

Quantum dot spin engineering
for quantum optics

Quantum dot spin engineering for quantum optics

Proefschrift

ter verkrijging van de graad van doctor
aan de Technische Universiteit Delft,
op gezag van de Rector Magnificus Prof. ir. K.C.A.M. Luyben,
voorzitter van het College voor Promoties,
in het openbaar te verdedigen op vrijdag 25 april 2014 om 12:30 uur

door

Barbara WITEK

Magister, Uniwersytet Warszawski, Polska
geboren te Szczecin, Polska

Dit proefschrift is goedgekeurd door de promotor:

Prof. dr. ir. L.P. Kouwenhoven

Copromotor:

Dr. V. Zwiller

Samenstelling promotiecommissie:

Rector Magnificus,	voorzitter
Prof. dr. ir. L.P. Kouwenhoven,	Technische Universiteit Delft, promotor
Dr. V. Zwiller,	Technische Universiteit Delft, copromotor
Prof. dr. A. Zrenner,	Universität Paderborn
Prof. dr. J. Rarity,	University of Bristol
Prof. dr. G. Bester,	Max Planck Institut für Festkörperforschung, Stuttgart
Prof. dr. L.D.A. Siebbeles,	Technische Universiteit Delft
Prof. dr. Y.M. Blanter,	Technische Universiteit Delft
Prof. dr. ir. L. Vandersypen,	Technische Universiteit Delft, reservelid



© 2014, Barbara Witek

All rights reserved. No part of this book may be reproduced, stored in a retrieval system, or transmitted, in any form or by any means, without prior permission from the copyright owner.

ISBN: 978-90-8593-184-3

Casimir PhD Series Delft-Leiden 2014-9

Printed by Proefschriftmaken.nl — www.Proefschriftmaken.nl

An electronic version of this thesis is available at www.library.tudelft.nl/dissertations

Contents

1	Introduction	1
1.1	Single electrons, holes and photons	1
1.2	Thesis overview	2
1.3	Bibliography	4
2	Quantum dots: single spins and single photons properties	5
2.1	Quantum dots as hosts for qubits	6
2.1.1	Electron and hole state description	6
2.1.2	Relaxation and decoherence	9
2.2	Spin to photon interface	11
2.2.1	Optical selection rules	11
2.2.2	Spin-photon quantum state transfer	15
2.2.3	Spin-photon entanglement	17
2.3	Spin mixing due to shape and strain anisotropy	18
2.3.1	Luttinger-Kohn and Bir Pikus Hamiltonians	18
2.3.2	Heavy and light hole spin mixing in quantum dots	22
2.4	Quantum dots as sources of nonclassical photons	24
2.4.1	Photon statistics	24
2.4.2	Single photon coherence	26
2.4.3	Single photon non-locality	28
2.5	Conclusion	31
2.6	Bibliography	33
3	Heavy and Light hole spin properties	39
3.1	Introduction	40
3.2	Exchange interaction and Zeeman effect Hamiltonians	44
3.3	Fine structure and spin-spin coupling constants	46
3.4	Diamagnetic shift and the wavefunction symmetry	48
3.5	Conclusions	48
3.6	Bibliography	49
4	Heavy-holes in the magnetic field	51

4.1	Introduction	52
4.2	Model	52
4.3	Experiment	54
4.3.1	Charged Exciton	55
4.3.2	Neutral Exciton	57
4.4	Discussion	60
4.5	Conclusion	64
4.6	Bibliography	65
5	Realizing a light-hole ground state in a quantum dot	67
5.1	Motivation and background	68
5.2	Sample structure	68
5.3	Light hole exciton states in photoluminescence	69
5.4	Exchange interaction from the atomistic pseudopotential method	73
5.5	Conclusion	74
5.6	Methods	75
5.6.1	Sample growth, processing and structural characterization	75
5.6.2	Optical characterization	76
5.7	Supplementary	77
5.7.1	Fine structure of as-grown QDs and of side view PL spectra	77
5.7.2	Magnetic-field-dependent PL data for as-grown QDs (HH exciton)	78
5.7.3	Magnetic-field dependent PL spectroscopy of tensile strained QDs	79
5.7.4	Evaluation of amplitude of HH-LH mixing	81
5.7.5	Numerical Results	81
5.8	Bibliography	84
6	Impact of strain and shape symmetry on spin states	87
6.1	Observation of a strong heavy-light hole spin mixing	88
6.1.1	Quantum dot sample description	88
6.1.2	Experimental results	89
6.1.3	Discussion and conclusion	91
6.2	Observation of the exchange interaction induced mixing	93
6.2.1	Quantum dot sample description	95
6.2.2	Experimental results	96
6.2.3	Discussion and conclusion	97
6.3	Conclusion	101
6.4	Bibliography	102
7	Non-locality of a single photon	105
7.1	Experimental details	106
7.1.1	Fiber network	106
7.1.2	Single photon source	108

7.1.3	Local oscillator and single photon indistinguishability	109
7.1.4	Local oscillator relative phase control	110
7.2	Data acquisition and analysis	111
7.2.1	Single channel histograms	112
7.2.2	Two channel coincidence histogram	115
7.3	Conclusion	120
7.4	Bibliography	120
8	Outlook	121
8.1	Spins: heavy or light?	121
8.2	Current status and future directions	123
8.3	Quantum optics: any entanglement is just mode entanglement!	124
8.4	Bibliography	127
A	Relevant matrices	131
A.1	Spin matrices	132
A.2	8 dimensional Exchange Hamiltonian	135
	Summary	137
	Samenvatting	139
	Acknowledgements	141
	List of Publications	143
	Curriculum Vitae	145

INTRODUCTION

1.1 Single electrons, holes and photons

Quantum dots are tiny boxes in which we can enclose single grains of matter - the electrons. However, as discovered a century ago by Louis de Broglie, electrons exhibit both the particle and a wave-like nature, a property that is referred to as wave-particle duality. In the past two decades thanks to the development of semiconductor growth techniques we are able to make the boxes out of the semiconductor material so tiny, that their size is comparable to the length of the electron wave. In such regime quantum mechanics plays a major role and quantum dots open a fascinating playground for physicists to first observe, understand and eventually learn to engineer quantum mechanical properties.

Semiconductor quantum dots, in contrast to electrically defined quantum dots, can trap both electrons and holes. A recombination of the electron and hole pair (an exciton) gives a photon, a quantum particle of light. This fact has at least two profound consequences. First of all, next to the electrical manipulation of the electron and hole spin, physicist can use light to address this quantum mechanical property. Single charges can be injected into the boxes with electric field^{1,2}, spin states manipulated with electric gates or, even faster, with a laser, and finally the result can be readout in the optical³⁻⁶ or electrical way^{7,8}. Therefore quantum dots deliver a freedom to explore both electrical and optical single spin manipulation schemes. Secondly, semiconductor quantum dots are natural platforms for interfacing single spins (stationary qubits) with photons (flying qubits). Spin-photon entanglement has been recently demonstrated^{9,10} and a single spin to single photon "coherent quantum translator" still awaits its realization¹¹. The way in which the spin state is translated onto a photon polarization depends on quantum numbers for the electron and hole

involved in the optical recombination. In III - V semiconductor quantum dots there are two species of holes (heavy and light) that differ by quantum numbers. In usual quantum dots, which physicists study for over twenty years, a hole ground state always has a dominantly heavy character. Because of this, experiments with a pure light hole ground state were out of reach. In this thesis, we show how a high purity light hole state can be engineered by careful design of quantum dot shape and strain.

The spin of an electron and a hole can point either up or down, or be in an up-down quantum superposition state. We can employ this quantum property and use the spin as a quantum bit. One of the basic requirements for a quantum bit is that the two levels (up and down) are separated and hence can be individually addressed¹². The magnetic field is commonly used to separate the up and down spin state. In this thesis we investigate the electron and hole response to the external magnetic field which is quantified by the g-factors and the diamagnetic shift coefficients.

Finally, exploring the quantum nature of single particles of matter is not the only possibility that quantum dots offer. Most importantly, quantum dots are also the sources of single quantum particles of light, photons. The statistics of photons emitted from the quantum dot makes them very unique and different from the sunlight or laser photons. In particular, having quantum dots we can produce the light states of a well defined number of photons. In this thesis we will take a single photon and demonstrate the most striking effect in quantum mechanics: quantum non-locality.

Quantum non-locality seems to be a valid property of the world we live in, even though it often counters our intuition and was not easy to accept even by Einstein¹³. Physicists use a test developed by John Bell to rule out between quantum non-locality and local realism. Ideally, two entangled particles are brought far enough to exclude any communication between them and then the sequence of Bell test measurements is performed. If the two distant particles behave like a single, inseparable entity, then their physical state is nonlocal. Our approach is to prove quantum non-locality with only one particle instead of a pair. In this thesis we show a Bell test performed on a single photon.

In summary, in this work we explore abstract quantum mechanical concepts such as non-locality and at the same time address very practical issues of spin states engineering. In both cases quantum dots are at the heart of our experiments and set the common denominator of our investigations.

1.2 Thesis overview

Chapter 2 presents an overview of theoretical concepts that this thesis is based on. We start with the introduction of basic electron and hole spin properties resulting from the wavefunction symmetry in semiconductor quantum dots. We deduce the optical selection rules for heavy and light hole excitations and explain how different hole

states manifest themselves in the polarization of the exciton emission. The physical intuition behind the Luttinger-Kohn model is developed in order to understand the influence of the quantum dot shape symmetry and strain distribution on the hole spin eigenstates. Finally, we focus on the properties of light emitted from the quantum dot, in particular its use in the test of the quantum mechanical concept of nonlocality.

Chapters 3 to 6 report on the experiments revealing the heavy and light hole excitons properties. In **chapter 3** we investigate the heavy and light hole spin characteristics that are manifested in the exchange interaction with the electron as well as the Zeeman and diamagnetic interaction in the external magnetic field. Experimental results are shown for highly symmetric GaAs/AlGaAs epitaxial quantum dots, where the hole character can be switched from a dominantly heavy to dominantly light. Further, a comprehensive study of the magnetic properties of the heavy hole exciton is presented in **chapter 4**. A complete g-factor tensor is revealed thanks to the use of magnetic fields in three different geometries. However, the InAsP quantum dots studied in chapter 4 differ substantially from the quantum dots studied in chapter 3. It is not only a difference in composition, but most importantly in the nanostructure geometry (InP nanowire) and crystal symmetry (wurtzite). In **chapter 5** we describe how to engineer a quantum dot system with a light hole ground state using tensile strain. Our first observations of the light hole exciton are shown and compared to the theoretical expectations from the atomistic pseudopotential calculations. Before the growth of quantum dots with high purity light hole ground state was optimized, we went through a series of attempts and characterized quantum dots with mixed hole states. The results of these measurements and the discussion of possible mixing mechanism can be found in **chapter 6**.

From considerations of electron and hole spins in semiconductor quantum dots we move on to an experiment with single photons in **chapter 7**. In this chapter we describe our attempt to test the quantum non-locality with only one particle: a single photon. Our goal is to show that a single photon can be in a superposition of two distant spatial modes. In order to prove quantum non-locality we implement a Bell measurement in which we probe wave-like properties of a single photon.

1.3 Bibliography

- [1] L. Kouwenhoven *et al.* Single electron charging effects in semiconductor quantum dots. *Zeitschrift für Physik B Condensed Matter* **85**, 367 (1991).
- [2] A. S. Bracker *et al.* Optical pumping of the electronic and nuclear spin of single charge-tunable quantum dots. *Phys. Rev. Lett.* **94**, 047402 (2005).
- [3] M. Kroutvar *et al.* Optically programmable electron spin memory using semiconductor quantum dots. *Nature* **432**, 81 (2004).
- [4] D. Press, T. D. Ladd, B. Zhang and Y. Yamamoto. Complete quantum control of a single quantum dot spin using ultrafast optical pulses. *Nature* **456**, 218 (2008).
- [5] B. D. Gerardot *et al.* Optical pumping of a single hole spin in a quantum dot. *Nature* **451**, 441 (2008).
- [6] A. Delteil, W.-b. Gao, P. Fallahi, J. Miguel-Sanchez and A. Imamoglu. Observation of quantum jumps of a single quantum dot spin using submicrosecond single-shot optical readout. *Phys. Rev. Lett.* **112**, 116802 (2014).
- [7] J. J. Finley *et al.* Electrical detection of optically induced charge storage in self-assembled inas quantum dots. *Applied Physics Letters* **73**, 2618 (1998).
- [8] A. Zrenner *et al.* Coherent properties of a two-level system based on a quantum-dot photodiode. *Nature* **418**, 612 (2002).
- [9] W. Gao, P. Fallahi, E. Togan, J. Miguel-Sanchez and A. Imamoglu. Observation of entanglement between a quantum dot spin and a single photon. *Nature* **491**, 426 (2012).
- [10] K. De Greve *et al.* Quantum-dot spin-photon entanglement via frequency down-conversion to telecom wavelength. *Nature* **491**, 421 (2012).
- [11] R. Vrijen and E. Yablonovitch. A spin-coherent semiconductor photo-detector for quantum communication. *Physica E: Low-dimensional Systems and Nanostructures* **10**, 569 (2001).
- [12] D. P. DiVincenzo. Quantum computation. *Science* **270**, 255 (1995).
- [13] A. Einstein, B. Podolsky and N. Rosen. Can quantum-mechanical description of physical reality be considered complete? *Physical review* **47**, 777 (1935).

QUANTUM DOTS: SINGLE SPINS AND SINGLE PHOTONS PROPERTIES

Semiconductor quantum dots can act both as convenient hosts of two-level quantum systems as well as controllable single, non-classical photon emitters. The unquestionable advantage of semiconductor quantum dots over other single photon emitters is the flexibility to tune their size, shape and composition. In this way a large degree of control of spin properties can be achieved, as well as optical properties. In this chapter we explain how the electron, heavy and light hole spins properties and optical selection rules are linked to the wavefunction symmetry. Optical selection rules for pure spin states in quantum dots are discussed. We explain the effect of shape and strain anisotropy on spin states mixing and discuss the signature of different mixing mechanisms revealed in the polarization of the exciton. Finally, after introducing optical selection rules, we focus on non-classical statistics of quantum dot photons and their coherence properties.

2.1 Quantum dots as hosts for qubits

A semiconductor quantum dot is a zero dimensional structure, where single electrons and holes can be trapped and manipulated. The spins of electrons and holes form a two level system constituting a natural candidate for a quantum bit - a qubit. An advantageous (and very peculiar!) feature of a quantum bit is that the binary values of a single bit can be brought into a coherent superposition:

$$|\Psi(t)\rangle = \cos\frac{\theta}{2} |\uparrow\rangle + e^{-\frac{i\Delta E t}{\hbar} + \phi} \sin\frac{\theta}{2} |\downarrow\rangle. \quad (2.1)$$

This equation describes the spin states $|\uparrow\rangle$ and $|\downarrow\rangle$ split by the Zeeman splitting ΔE and their time evolution in an external field. In a perfectly isolated system this spin state would obey the dynamics described above forever. In reality, there are a number of effects that damp the evolution in time of a spin in a semiconductor. The randomization of θ leads to the longitudinal spin relaxation, described by a time T_1 . The loss of the relative phase information ϕ is referred to as transverse spin decoherence, occurring in time T_2 . Preservation of the spin orientation and its coherence are the necessary conditions for an undisturbed quantum computation. Electron spins, for a long time, have been considered as natural candidates for qubits. In recent years however, increasing attention has been paid to hole spins. Both spin species have been found to have long coherence times relative to the expected time for gate operations. Here, we discuss and compare the spin states of electrons and holes in a quantum dot. Before we summarize the properties of these qubits, such as relaxation time T_1 and coherence time T_2 , we shall start with the description of the valence and conduction band in III-V semiconductor quantum dots.

2.1.1 Electron and hole state description

In order to develop understanding of the qubit states in a quantum dot, we shall recall briefly the description of the electron and hole states in a bulk semiconductor. In the crystal lattice of a semiconductor, the electron experiences a periodic potential. According to Bloch's theorem, this potential introduces a modulation to the free electron plane wave:

$$|\Psi(r)\rangle = e^{ikr} |u_k^b(r)\rangle \quad (2.2)$$

The Bloch state $u_k^b(r)$ is a periodic function in the Bravais lattice describing an electron in the band b with wave vector k . The energy of the electron in the momentum space k for the conduction c and valence v bands is shown in figure 2.1(a). Around the extrema of the bands the energy dispersion is parabolic and can be approximated with the energy of a free electron with effective mass m_b . The effective mass is obtained from the curvature of the energy dispersion. This is how the two upper valence band states take their names: the heavy (HH) and light hole (LH). The HH and LH sub-bands are degenerate at the Γ point ($k = 0$) and split into two branches for finite

wave vectors k . The third sub-band in the valence band is the spin orbit split-off (SO) band.

Let us focus now at the orbital L and spin S quantum numbers for the subbands at the Γ point ($k = 0$). A brief look at the symmetry properties of the atomic eigenfunctions can greatly enhance our understanding of the bandstructure. First, we start by looking at the energy eigenvalues of the individual atoms that constitute the semiconductor crystal. The individual atoms have the outermost (valence) electrons in s- and p-type orbitals. The symmetry and geometric properties of these orbitals are depicted in fig. 2.1(b). Once the atoms form a crystal, the valence electrons hybridize into sp^3 orbitals that lead to tetrahedral bonding. The crystal develops its own bandstructure with gaps and allowed bands. In semiconductors the conduction and valence bands are of major interest. It turns out that the states near the band-edges behave very much like the s and the three p -type orbitals they had when they were individual atoms. Electrons in the s -type conduction band have therefore $L = 0$ and $S = 1/2$, resulting in the total angular momentum $J_e = 1/2$. For p-type holes $L = 1$ and $S = 1/2$, giving two possibilities for total angular momentum: $J = L + S = 3/2$ and $J = |L - S| = 1/2$. States with $J = 1/2$ and $J = 3/2$ are split by the spin-orbit interaction and a state with $J = 1/2$ has a lower energy. This is the origin of the split-off band. States with $J = 3/2$ have two projections in the z direction: states with $J_z = \pm 3/2$ form a HH subspace and states with $J_z = \pm 1/2$ a LH subspace. The Bloch functions retain much of the symmetries that the atomic orbitals possess. Conduction band electron states can be expressed as:¹:

$$\begin{aligned} |u_{e,\uparrow}\rangle &= |S\rangle |\uparrow\rangle, \\ |u_{e,\downarrow}\rangle &= |S\rangle |\downarrow\rangle, \end{aligned} \quad (2.3)$$

valence band HH states:

$$\begin{aligned} |u_{HH,\uparrow}\rangle &= -\frac{1}{\sqrt{2}} |X + iY\rangle |\uparrow\rangle, \\ |u_{HH,\downarrow}\rangle &= \frac{1}{\sqrt{2}} |X - iY\rangle |\downarrow\rangle, \end{aligned} \quad (2.4)$$

LH states:

$$\begin{aligned} |u_{LH,\uparrow}\rangle &= -\frac{1}{\sqrt{6}} (|X + iY\rangle |\downarrow\rangle + 2|Z\rangle |\uparrow\rangle), \\ |u_{LH,\downarrow}\rangle &= \frac{1}{\sqrt{6}} (|X - iY\rangle |\uparrow\rangle + 2|Z\rangle |\downarrow\rangle), \end{aligned} \quad (2.5)$$

and SO states:

$$\begin{aligned} |u_{SO,\uparrow}\rangle &= -\frac{1}{\sqrt{3}} (|X + iY\rangle |\downarrow\rangle + |Z\rangle |\uparrow\rangle), \\ |u_{SO,\downarrow}\rangle &= \frac{1}{\sqrt{3}} (|X - iY\rangle |\uparrow\rangle - |Z\rangle |\downarrow\rangle). \end{aligned} \quad (2.6)$$

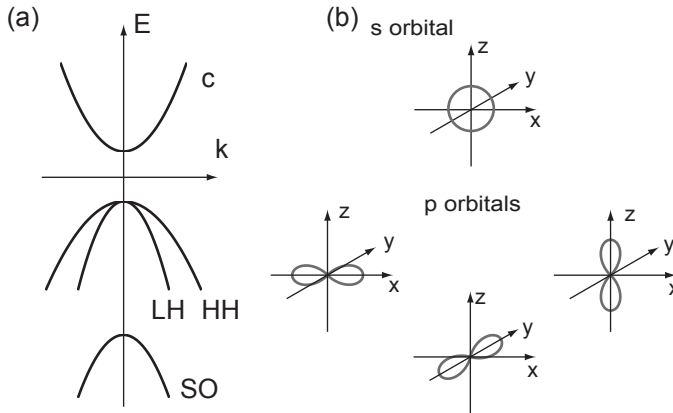


Figure 2.1 | (a) The bandstructure of a typical III-V bulk semiconductor. (b) s- and p-like atomic orbitals.

Since the spin-orbit splitting is large (340 *meV* for GaAs and 380 *meV* for InAs) we exclude the SO states from our further consideration.

An electron in a semiconductor quantum dot is trapped in all three dimensions and its quantum mechanical behavior becomes apparent. Thanks to the effective mass approximation, the equation of motion in the band *b* takes a quite simple form again:

$$|\Psi(r)\rangle = |\phi(r)\rangle |u_k^b(r)\rangle. \quad (2.7)$$

In contrast to the bulk case (eq. 2.1.1), the free electron plane wave function e^{ikr} is replaced with the envelope function $\phi(r)$, which is localized at the quantum dot according to the effective quantum dot potential. It is important to note, that the Bloch function $u_k^b(r)$ is still present in the description of the electron states. The orbital symmetry of carriers trapped in quantum dots will later help us understand their spin properties and interactions with the environment. In a quantum dot the HH and LH bands are no longer degenerate (see chapter 6). Typical HH-LH splittings found in quantum dot experiments are on the order of $\Delta_{HH-LH} \approx 10$ *meV*. There are two reasons why HHs usually form the ground state in a quantum dot. First of all, since the eigenenergy of the confined state is inversely proportional to the mass, heavier particles occupy lower levels. Secondly, biaxial in-plane compressive strain lifts the HH band. This is a major effect responsible for the HH-LH splitting in Stransky-Krastanov type dots, where strain is required in quantum dot formation. Due to such large splitting in usual quantum dots, the hole ground state is in first

approximation treated as a purely HH state. For dots with rotational symmetry, the hole ground state can be more than 90% heavy. Therefore LH states, being beyond experimental reach, were often neglected. It has been observed for GaAs, InAs, CdTe, CdSe that in-plane shape elongation can tremendously enhance the LH admixture typically up to 20 – 30%²⁻⁴, or even 70% as reported once for InAs quantum dots⁵. In this work we will present studies of an almost pure LH ground state achieved with a unique growth and fabrication technique that introduces tensile strain. Before we present the results in chapter 5, we shall discuss the optical selection rules for both the heavy and light hole in a quantum dot.

2.1.2 Relaxation and decoherence

An ideal qubit should be robust against environment influences that lead to decoherence and relaxation. Here we discuss and compare the performance of three qubit candidates: the electron spin, the heavy hole spin and the light hole spin.

In bulk III-V semiconductors, hole spin relaxes much faster than electron spin. This is due to much stronger spin-orbit interaction for holes. The spin relaxation of holes is extremely fast, in the femtosecond time domain⁶. However, quantum confinement can improve this situation. A substantial increase in the hole spin relaxation time is observed in quantum wells (up to 1 ns⁷) where the HH - LH mixing is partially inhibited by motion quantization. Still, the hole spin relaxation time in quantum wells is typically on the order of 10^3 times shorter than for electrons. It is only in quantum dots, that the major hole spin relaxation mechanism, the spin-orbit valence band mixing, is strongly suppressed. Therefore in quantum dots, the two main spin-flip and decoherence mechanisms are the same for both electrons and holes: (i) interactions with phonons and (ii) interactions with nuclear spins⁸. The nature of these interactions is different for the hole and electron spin, and we are going to discuss situations where either the hole or the electron spin is advantageous.

First, we will discuss spin-phonon coupling that is responsible for the spin-flip transitions between the two Zeeman-split spin levels defining a qubit. This process limits the T_1 time. In quantum dots at low temperatures it is the spin-orbit interactions that mediates the spin-phonon scattering^{9,10}. Naturally for HHs, due to residual HH-LH mixing, this process is more efficient. Relaxation time T_1 of the electron spin can be as long as 20 ms ($B_{ext} = 4T$ and $T = 1K$)¹¹. In an equivalent experiment the HH spin performs on average 5 – 10 times worse, with $T_1 = 270 \pm 180\mu s$ ($B_{nuclei} = 1.5T$, $T = 8K$)⁸. However, it is in principle possible to achieve the hole relaxation time comparable to electron, or even longer¹⁰. The geometry of the quantum dot affects the magnitude of the spin-orbit interaction. The ratio of the electron to hole spin-orbit interaction $H_{el}^{so}/H_{HH}^{so} = (l/h)^2$, depends on the lateral size l of the quantum dot and the height h . In the limit of strongly two-dimensional quantum dots ($l \gg h$), heavy holes should have a longer relaxation time than electrons. Despite this prediction longer heavy hole T_1 time has not been reported yet (to the best of our knowledge). In

both experiments measuring the electron¹¹ and hole⁸ spin storage time, the external magnetic field facilitates the spin-phonon coupling and therefore reduces drastically the relaxation time $T_1 \propto B^{-5}$ (effect of Dresselhaus spin-orbit). The best relaxation time T_1 is achieved at zero magnetic field, on the other hand, the magnetic field is essential in defining well separated and individually addressable two levels of a qubit. Interestingly, in an experiment demonstrating a single hole spin initialization by Brian D. Gerardot *et al.*¹² no external magnetic field was needed to individually pump one of the spin states, because holes are less sensitive to the nuclear spins. This work brings us to the discussion of the hyperfine interaction for the hole and electron spin.

In typical GaAs quantum dots a carrier spin interacts with a bath of $10^4 - 10^5$ nuclear spins. The nuclear spins create a fluctuating effective magnetic field, the Overhauser field. The carrier spin precesses in the Overhauser field such that the time-averaged coherence time, is much shorter than the intrinsic decoherence time, T_2 . Electrons, owing to the *s*-type symmetry, experience a direct contact hyperfine interaction with the nuclear spin. Holes, however, described by a *p* atomic orbital whose density vanishes at the nuclei site, have a strongly suppressed contact hyperfine interaction. A weaker, long range dipole - dipole interaction with the nuclei dominates^{13,14}. Recent measurements on InGaAs/GaAs QDs¹⁵ and InP/GaInP QDs¹⁶ show that the HH hyperfine interaction is 10 times smaller than for electrons (9% and 11%). Interestingly, in both cases the sign of the hole hyperfine interaction is opposite to that of the electron. Otherwise, these results would be in excellent agreement with theoretical predictions of the anisotropic dipole-dipole hole hyperfine interaction¹⁴. The explanation to this puzzle came with an element-sensitive measurement of hole hyperfine interaction¹⁷. The idea was to first polarize the whole nuclear spin bath with the pump pulse, and later depolarize selectively one of the isotopes with a radiofrequency oscillating magnetic field. It was found that anions, such as P and As, have a quite large positive hyperfine constant (+18% of the electron). Cations (Ga and In), in contrast, have a negative hyperfine (-4% and -15%). This variation in the sign of the hyperfine coupling could not be explained if the hole Bloch function had only a *p*-type symmetry. As apparent from the expressions of the hole hyperfine Hamiltonians, *p*-orbitals can have only a positive contribution:

$$\begin{aligned}
 H_{hf}^{HH} &= \sum_j \frac{A_j^j}{2} |\Psi_{\pm 3/2}(R_j)|^2 \left(\frac{12}{5} M_p - \frac{18}{7} M_d \right) I_z^j S_z^{HH} + \frac{9}{7} M_d (I_x^j S_x^{HH} - I_y^j S_y^{HH}), \\
 H_{hf}^{LH} &= \sum_j \frac{A_j^j}{2} |\Psi_{\pm 1/2}(R_j)|^2 \left(\frac{4}{5} M_p - \frac{18}{7} M_d \right) I_z^j S_z^{LH} + \left(\frac{8}{5} M_p - \frac{9}{7} M_d \right) (I_x^j S_x^{HH} - I_y^j S_y^{HH}).
 \end{aligned}
 \tag{2.8}$$

where positive integrals M_l ($l = p, d$) depend on the hydrogenic radial wavefunctions

$R_l(r)$ corresponding to the shell with orbital momentum L and normalized by the density $(4\pi)^{-1}|S(0)|^2$. Only an addition of the d -orbital can lead to a negative sign of the interaction. To account for a negative hyperfine constant for cations a contribution of 20% of the d -type Bloch symmetry is estimated. Anions, however, are closer to a pure p-type orbital.

So far, a comparison was carried out between the electron and the heavy hole spin. Can the light hole spin provide us with an equally robust qubit as the heavy hole spin? The answer is apparent from eq. 2.8. Terms $I_i S_i$ describe flip-flops between hole and nuclear spin. If we consider a pure p-type orbital, HHs are sensitive only to the z-component of the Overhauser field, whereas LHs can sense the Overhauser field in any direction, especially in-plane field.¹⁴. Therefore the admixture of LH into the HH state is believed to decrease the performance of the hole qubit in quantum dots^{13,14}. However, the T_2 time of a pure LH state has not been yet experimentally determined.

2.2 Spin to photon interface

Quantum dots made of semiconductors with direct bandgaps are optically active. It means that the energy quanta of the electromagnetic field can promote the electron from the valence band to the conduction band, leaving a hole behind. The electron-hole pair created in the process of light absorption is called an exciton. When the exciton recombines, it emits a photon. Quantum dots are therefore a natural platform for spin-photon interfaces. Understanding the optical selection rules that govern the transitions between the electron and hole spin opens up many interesting possibilities of addressing the spin with light. It has been shown that one can initialize, control and readout spin states using laser light^{12,18-21}. Furthermore, HH exciton selection rules enable spin-photon entanglement^{22,23}, whereas LH optical selection rules allow for coherent transfer of quantum information from spin to photon and vice versa²⁴.

2.2.1 Optical selection rules

The key to understanding optical selection rules lies in the symmetry of the hole and electron wavefunctions. To analyze the problem of a quantum dot interacting with the quantized electromagnetic field, in the strong confinement regime, we can apply the standard model of a two level system with states $|1\rangle$ and $|2\rangle$. In a very good approximation, the interaction of the electron confined in the quantum dot with the electromagnetic field reduces to the electric dipole interaction. The oscillator strength $f_{2,1}$ quantifies how much the two levels are coupled to the radiative field:

$$f_{2,1} = \frac{2|\mathbf{e}_{\mathbf{k}s} \cdot \langle 2|p|1\rangle|^2}{m_0|E_2 - E_1|} \quad (2.9)$$

The unit vector $\mathbf{e}_{\mathbf{k}s}$ denotes the direction of light polarization, and $\langle 2|p|1\rangle$ is the momentum matrix element. For optical transitions, the momentum matrix element

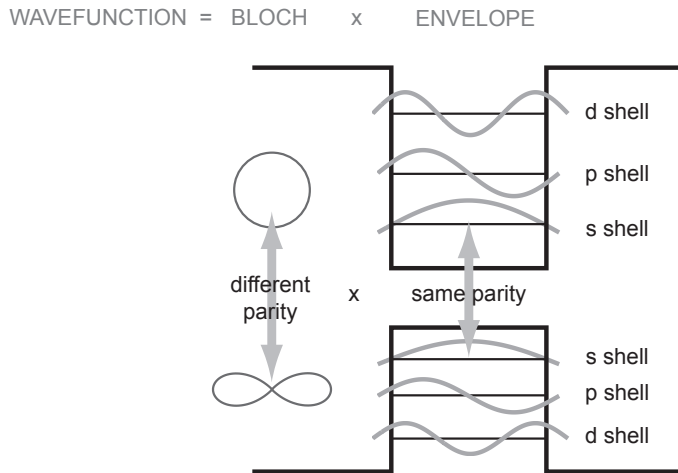


Figure 2.2 | Schematic of the electron and hole wavefunction symmetry. The optical transitions are allowed between states of overall different parity

should be non-vanishing. This imposes certain symmetry criteria on states $|1\rangle$ and $|2\rangle$. Since the momentum operator p changes the parity of the state, the electric dipole transition is possible only between states of different parity. Let us look again at the electron and hole wavefunctions in the quantum dot:

$$|1\rangle = |\phi_c\rangle |u_c\rangle, \quad |2\rangle = |\phi_v\rangle |u_v\rangle. \quad (2.10)$$

As we have already seen in section 2.1.1, the electron $|u_c\rangle$ and hole $|u_v\rangle$ Bloch functions have a different parity. In order to ensure that the total electron and hole wavefunctions $|1\rangle$ and $|2\rangle$ have a different parity, the envelope wavefunctions $|\phi\rangle$ should have the same parity. This is the reason why the optical transitions in the quantum dot are allowed only between the same shells, as illustrated in fig. 2.2.

It can be derived that the following selection rules hold for the quantum numbers:

$$J - J' = 0, \pm 1, \quad L - L' = \pm 1, \quad J_z - J'_z = 0, \pm 1. \quad (2.11)$$

The transitions with $J_z - J'_z = \pm 1$ are circularly polarized (σ polarized), as they involve net transfer of angular momentum and $J_z - J'_z = 0$ transitions are linearly polarized (π polarized). We shall recall now the quantum numbers for the electron and hole states introduced in section 2.1.1. First, we consider the excitons composed of the HH with $J_z = \pm 3/2$ (\uparrow or \downarrow) and the electron with $S_z = \pm 1/2$ (\uparrow or \downarrow). We get

four exciton states of different exciton total momentum $|J_{X,z}\rangle$:

$$|+2\rangle = \left| +\frac{3}{2}, +\frac{1}{2} \right\rangle = |\uparrow_{HH}\uparrow\rangle \quad (2.12)$$

$$|+1\rangle = \left| +\frac{3}{2}, -\frac{1}{2} \right\rangle = |\uparrow_{HH}\downarrow\rangle \quad (2.13)$$

$$|-1\rangle = \left| -\frac{3}{2}, +\frac{1}{2} \right\rangle = |\downarrow_{HH}\uparrow\rangle \quad (2.14)$$

$$|-2\rangle = \left| -\frac{3}{2}, -\frac{1}{2} \right\rangle = |\downarrow_{HH}\downarrow\rangle \quad (2.15)$$

with the electron states:

$$\begin{aligned} \left| +\frac{1}{2} \right\rangle &= |S\rangle |\uparrow\rangle, \\ \left| -\frac{1}{2} \right\rangle &= |S\rangle |\downarrow\rangle, \end{aligned} \quad (2.16)$$

and HH states:

$$\begin{aligned} \left| +\frac{3}{2} \right\rangle &= |\uparrow\rangle_{HH} = -\frac{1}{\sqrt{2}} |X + iY\rangle |\uparrow\rangle, \\ \left| -\frac{3}{2} \right\rangle &= |\downarrow\rangle_{LH} = \frac{1}{\sqrt{2}} |X - iY\rangle |\downarrow\rangle, \end{aligned} \quad (2.17)$$

Immediately, one can see that two of these states with $J_{X,z} = \pm 2$ have to be dark. The two remaining ones are circularly polarized. The polarization of the transition is directly governed by the symmetry of the Bloch function. It is not the s-type electron of the homogenous probability distribution, but the p-type hole that sets the direction of the electric dipole transition. This is clearly seen from the scalar product of the unitary polarization vector with the transition dipole matrix elements:

$$\left\langle +\frac{1}{2} \left| \mathbf{e} \cdot \mathbf{p} \right| +\frac{3}{2} \right\rangle = 0 \quad (2.18)$$

$$\left\langle -\frac{1}{2} \left| \mathbf{e} \cdot \mathbf{p} \right| +\frac{3}{2} \right\rangle = -\frac{\Pi}{\sqrt{2}} (\mathbf{e}_x + i\mathbf{e}_y) \quad (2.19)$$

$$\left\langle +\frac{1}{2} \left| \mathbf{e} \cdot \mathbf{p} \right| -\frac{3}{2} \right\rangle = \frac{\Pi}{\sqrt{2}} (\mathbf{e}_x - i\mathbf{e}_y) \quad (2.20)$$

$$\left\langle -\frac{1}{2} \left| \mathbf{e} \cdot \mathbf{p} \right| -\frac{3}{2} \right\rangle = 0, \quad (2.21)$$

where $\Pi = \langle S | p_x | X \rangle = \langle S | p_x | Y \rangle = \langle S | p_z | Z \rangle$. Light has a negligible action on spin, the electron promoted from the valence band to the conduction band leaves a hole

behind with an opposite spin. From this viewpoint, the optical transition for exciton states with $J_{X,z} = \pm 2$ would not conserve the spin orientation.

There is no such problem for the exciton states composed of the LH and electron spins. Both of the LH states with $J_z = \pm 1/2$ are built from the linear combination of spin up and down states, therefore they couple to every electron spin orientation:

$$|+1\rangle = \left| +\frac{1}{2}, +\frac{1}{2} \right\rangle = |\uparrow_{LH}\uparrow\rangle \quad (2.22)$$

$$|+0\rangle = \left| +\frac{1}{2}, -\frac{1}{2} \right\rangle = |\uparrow_{LH}\downarrow\rangle \quad (2.23)$$

$$|-0\rangle = \left| -\frac{1}{2}, +\frac{1}{2} \right\rangle = |\downarrow_{LH}\uparrow\rangle \quad (2.24)$$

$$|-1\rangle = \left| -\frac{1}{2}, -\frac{1}{2} \right\rangle = |\downarrow_{LH}\downarrow\rangle \quad (2.25)$$

where:

$$\begin{aligned} \left| +\frac{1}{2} \right\rangle &= |\uparrow_{LH}\rangle = -\frac{1}{\sqrt{6}}(|X + iY\rangle |\downarrow\rangle + 2|Z\rangle |\uparrow\rangle), \\ \left| -\frac{1}{2} \right\rangle &= |\downarrow_{LH}\rangle = \frac{1}{\sqrt{6}}(|X - iY\rangle |\uparrow\rangle + 2|Z\rangle |\downarrow\rangle), \end{aligned} \quad (2.26)$$

All four LH exciton states are bright, however, with different oscillator strengths:

$$\left\langle +\frac{1}{2} \left| \mathbf{e} \cdot \mathbf{p} \right| +\frac{1}{2} \right\rangle = -\frac{\Pi}{\sqrt{6}}(\mathbf{e}_x + i\mathbf{e}_y) \quad (2.27)$$

$$\left\langle -\frac{1}{2} \left| \mathbf{e} \cdot \mathbf{p} \right| +\frac{1}{2} \right\rangle = \frac{2\Pi}{\sqrt{6}}(\mathbf{e}_z) \quad (2.28)$$

$$\left\langle +\frac{1}{2} \left| \mathbf{e} \cdot \mathbf{p} \right| -\frac{1}{2} \right\rangle = \frac{2\Pi}{\sqrt{6}}(\mathbf{e}_z) \quad (2.29)$$

$$\left\langle -\frac{1}{2} \left| \mathbf{e} \cdot \mathbf{p} \right| -\frac{1}{2} \right\rangle = \frac{\Pi}{\sqrt{6}}(\mathbf{e}_x - i\mathbf{e}_y), \quad (2.30)$$

All possible optical transitions for the HH and LH excitons are summarized in fig 2.3. The offset between the HH and LH states was set for clarity of the diagram and does not impose any specific band ordering (in this thesis we will show experimental results for two situations: HH or LH on the top of the valence band). The thickness of the arrows is proportional to the transition oscillator strength. An electron spin up (+1/2) can recombine with the HH or LH. In the first case the emitted photon is left-handed circularly polarized (σ^-), in the latter case right-handed circularly polarized (σ^+). If the hole state is a mixture of the HH and the LH $|hole\rangle = \alpha|HH\rangle + \beta|LH\rangle$, then the resulting photon polarization is elliptical (as the sum of two uneven contributions from

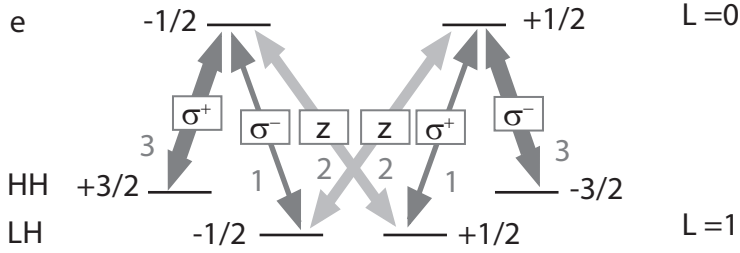


Figure 2.3 | Schematic of the optical transitions between the hole and electron states.

the orthogonal circular components $\alpha |\sigma^- \rangle + \beta/3 |\sigma^+ \rangle$). Quantifying the ellipticity of the neutral exciton emission has been an experimental measure of the HH-LH mixing in QD experiments. We shall notice that the oscillator strength of the transition to the LH state is 3 times weaker than to the HH state. Why is the probability of the recombination to the LH state lower than to the HH state? If we look at the overall picture, it is not. Collecting light emitted only along the z -direction (in other words: in-plane polarized), shows only part of the LH exciton emission. There is 66% probability, that the LH exciton will give a z -polarized photon. Such a photon can be observed only in a non standard micro-luminescence geometry, whit collection from the edges of the semiconductor sample. A pure HH exciton emission will not result in z -polarized light.

In conclusion, there is a crucial difference between the optical transitions derived from the selection rules for the HH and the LH exciton. The HH couples to only one electron spin, making the selection rules very clear. In contrary, LH states can recombine with both electron up and down spin. One can say that there is no "spin blockade" for the LH transition. In the following sections we will discuss the best use of those radically different optical transitions.

2.2.2 Spin-photon quantum state transfer

In the context of quantum communication between remote quantum nodes the possibility of transferring the quantum information from the stationary qubit (the electron or hole spin) on to the flying qubit (a photon) and vice versa, is highly appealing. Let's consider a photon in a quantum superposition of states $|\phi_{ph}\rangle = \alpha |\sigma^+\rangle + \beta |\sigma^-\rangle$ and a quantum dot with the HH band as a ground state. Absorption of such photon creates a superposition of HH excitons:

$$|\phi_{ph}\rangle = \alpha |\sigma^+\rangle + \beta |\sigma^-\rangle \iff |\Phi_X\rangle = \alpha |\uparrow_{HH}\downarrow\rangle + \beta |\downarrow_{HH}\uparrow\rangle. \quad (2.31)$$

We have transferred the quantum information from the photon to the exciton state, however, our goal is not yet achieved. Now we shall remove one of the carriers with an external electric field, so that a single stationary qubit is left. Its quantum state should be a faithful copy of the photon state. However, the electron and hole spins in equation 2.31 are inseparable: they are entangled. Any attempt at removing one of the carriers will instantly collapse the state of the remaining one. As we can see, HH excitons are not suitable in this scenario of photon to spin state mapping. Nonetheless, using the LH exciton might be a solution, since one LH state couples optically to both electron spins (see fig. 2.3). Therefore the hole state can be simply factored out from the superposition of LH exciton states:

$$|\phi_{ph}\rangle = \alpha |z\rangle + \beta |x\rangle \iff |\Phi_X\rangle = \alpha |\downarrow_{LH}\uparrow\rangle + \beta |\downarrow_{LH}\downarrow\rangle = |\downarrow_{LH}\rangle (\alpha |\uparrow\rangle + \beta |\downarrow\rangle). \quad (2.32)$$

The LH can be now removed from the quantum dot without any harm for the electron state. The electron state carries the information about the photon quantum state. This scheme was proposed by Vrijen and Yablonowitch²⁴ and became one of our motivations for engineering quantum dots with LHs. This proposal is not trivial to implement for a few reasons. First of all, because of the uneven oscillator strength of the LH exciton transitions, the coefficients in the superposition state α and β might not be evenly mapped. Secondly, there are certain requirements on the electron and hole g -factors ($g_e \ll g_{LH}$). All these issues are discussed in greater detail in the original proposal. Lastly, another difficulty is an enormous fine structure splitting (above 400 μeV !) of the LH exciton that we have measured (chapter 3 and 5 of this thesis), but not considered by the authors.

Why is the LH exciton exchange an obstacle? In eq. 2.32 we consider a photon in a superposition of x and z polarization. The excitons corresponding to these polarization states are split by as much as 430 μeV (e.g. QDA^{LH} in chapter 3) and therefore a photon of unusually large natural linewidth would be needed to simultaneously address both transitions. We can try to bring these excitons closer with external magnetic field in Faraday geometry. The value of the magnetic field required to cancel the splitting between the x and z polarized excitons depends uniquely on the quantum dot electron and hole g -factors. For the studied QDA^{LH} we would need $B = 15$ T, which is not impossible, however, not very practical. Besides practical reasons, high magnetic fields are also a problem for the qubit coherence (as discussed already in section 2.1.2. Could we have anticipated such enormous exchange interaction for the LH exciton? In the literature on excitons in quantum wells a splitting between x and z polarized LH excitons was reported to be at least 300 μeV up to 1.1 meV ²⁵. Moreover, these experimental values found confirmation in theoretical calculations. In chapter 5 we also provide a theoretical model reproducing the values of exchange energies.

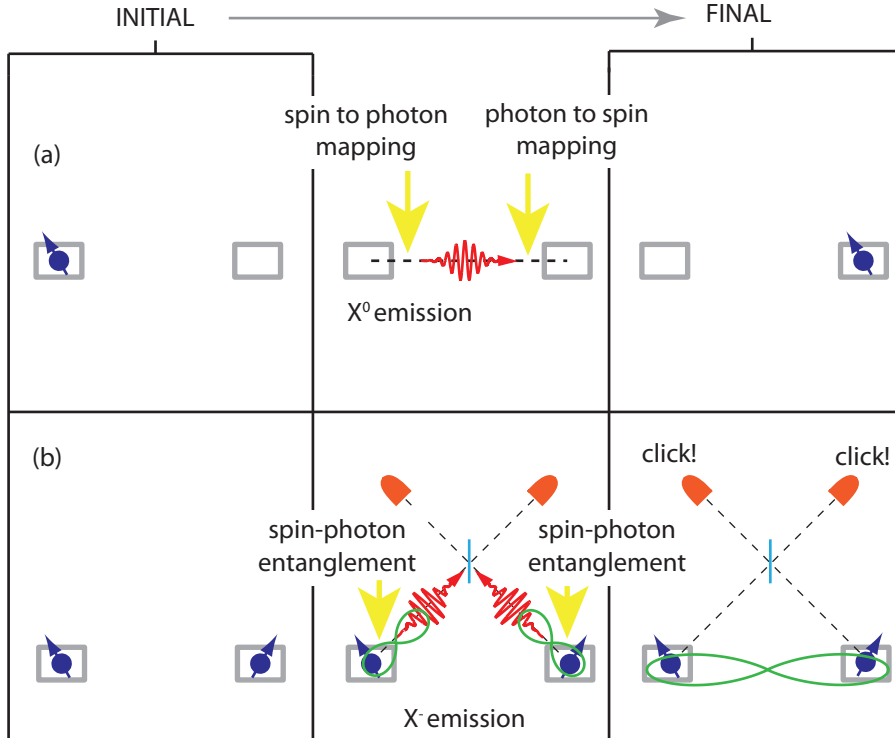


Figure 2.4 | A comparison between the application of the (a) spin to photon quantum state coherent transfer and (b) spin-photon entanglement.

2.2.3 Spin-photon entanglement

Spin-photon entanglement is another important step for quantum communication and quantum networks. It has been demonstrated for trapped ions²⁶, neutral atoms^{27,28} and nitrogen-vacancy centers²⁹. Recently, it has been reported also for semiconductor quantum dots in two independent experiments by De Greve *et al.*²³ and Gao *et al.*²². In both cases a negatively charged trion X^- transition in the magnetic field in Voigt configuration was used. As a result of a X^- recombination, a single photon is emitted and a single electron remains in the QD. The spin of the electron is entangled with the energy and the polarization of the emitted photon:

$$|\Phi\rangle = \frac{1}{\sqrt{2}}(|\downarrow\rangle |\omega_{red}; H\rangle + i |\uparrow\rangle |\omega_{blue}; V\rangle). \quad (2.33)$$

One degree of freedom in this entangled state has to be erased in order to avoid a problem of "which-path information". The information about the polarization of

the photon was erased with a polarizer in the Gao *et al.* experiment, whereas the information about the energy of the photons was erased in a very fast detection in the De Greve *et al.* experiment. The exact details of these experiments are not the main subject of this work, yet it is important to point out the importance of the selection rules. Spin-photon entanglement in those experiments could be achieved thanks to clear polarization selection rules for transitions involving heavy holes. To the best of my knowledge, it would be impossible to implement spin-photon entanglement using light holes.

Here I would also like to emphasize, that the demonstration of the spin-photon entanglement does not completely replace the need for spin to photon coherent transfer. Those two schemes are not equivalent and serve slightly different aspects of quantum communication, as depicted in figure 2.4. The goal of the first scheme is to transfer the quantum information from one quantum computer to the other using photons as mediators. In the second scheme, spin-photon entanglement is a first step towards entangling remote spins via entanglement swapping. Once the entanglement between two remote spins is established, the quantum information can be teleported from one computer to the other, as demonstrated for ions³⁰. Spin-photon entanglement can be also used to transfer the state of the photon to the electron in a quantum dot as demonstrated in the follow up experiment by Gao *et al.*³¹. In contrast to the Vrijen and Yablonowitch proposal, the photon is not simply absorbed in the quantum dot, but its state is teleported to the electron spin in a quantum dot.

2.3 Spin mixing due to shape and strain anisotropy

The shape symmetry of semiconductor quantum dots and strain distribution have a tremendous influence on the exciton spin states and on the emitted photons polarization. Strain to a large extent, can redesign a semiconductor bandstructure. It can modify the bandgap as well as reorder the subbands in the valence band. This is why strain has become a powerful tool in engineering semiconductor nanostructure properties. The shape of the quantum dot confining potential determines the character of the quantized states. In this section we study both the effects of the quantum dot shape and strain distribution on hole spins. We show how hole states spin mixing demonstrates in the polarization of the exciton states.

2.3.1 Luttinger-Kohn and Bir Pikus Hamiltonians

For simplicity, we first discuss a semiconductor grown along the [001] direction (z), which is the case for most semiconductor quantum dots, including the GaAs quantum dots discussed in section 6.1. The description of wurtzite nanowires grown along the [111] direction is more complex, because of the built in piezoelectric fields^{32,33}.

The lattice of a semiconductor is under biaxial stress if the interatomic distances a between the atoms in the $x - y$ plane do not equal the semiconductor lattice constant

a_0 . The net strain in the semiconductor plane ϵ_{\parallel} is given by

$$\epsilon_{\parallel} = \epsilon_{xx} = \epsilon_{yy} = \frac{a - a_0}{a_0}. \quad (2.34)$$

If ϵ_{\parallel} has a negative value, then we have biaxial compressive strain, whereas a positive value indicates tensile strain. In response to the biaxial stress, the layer relaxes along the growth direction z as illustrated in fig. 2.5(a). Strain along z ϵ_{zz} is of opposite sign to ϵ_{\parallel} and linked to it by the Poisson ratio σ :

$$\epsilon_{zz} = -\frac{2\sigma}{1 - \sigma}\epsilon_{\parallel}. \quad (2.35)$$

For tetrahedral semiconductors σ is approximately $\frac{1}{3}$ so that $\epsilon_{zz} \simeq -\epsilon_{\parallel}$.³⁴ The total strain can be resolved into a purely axial component ϵ_{ax} ,

$$\epsilon_{ax} = \epsilon_{zz} - \epsilon_{\parallel} \simeq -2\epsilon_{\parallel}, \quad (2.36)$$

and a hydrostatic component $\epsilon_{vol}(= \Delta V/V)$

$$\epsilon_{vol} = \epsilon_{xx} + \epsilon_{yy} + \epsilon_{zz} \simeq -\epsilon_{\parallel}. \quad (2.37)$$

In other words, as a result of the hydrostatic strain the volume is changed, whereas as a result of the axial strain the shape of the structure is affected. It is very useful for further analysis and predictions to resolve those two strain components.

The band structure of semiconductors can be calculated by many different methods. The pseudopotential method has been used to look at both the conduction and valence states in quantum nanostructures (e.g. Ref³⁵⁻³⁷), as has the tight-binding method³⁸⁻⁴⁰. However, here I choose to discuss the method that speaks best to my physical intuition, which is the Bloch and envelope function approximation and the Luttinger-Kohn Hamiltonian^{41,42} for the valence band description. The Luttinger-Kohn Hamiltonian of the unstrained structure and the HH and LH subbands ($|\frac{3}{2}, \frac{3}{2}\rangle, |\frac{3}{2}, \frac{1}{2}\rangle, |\frac{3}{2}, -\frac{1}{2}\rangle, |\frac{3}{2}, -\frac{3}{2}\rangle$) is given by:

$$H_{LK} = \begin{pmatrix} P + Q & S & R & 0 \\ S^\dagger & P - Q & 0 & R \\ R^\dagger & 0 & P - Q & -S \\ 0 & R^\dagger & -S^\dagger & P + Q \end{pmatrix} \quad (2.38)$$

Matrix elements in this Hamiltonian define the energy dispersion of the valence subbands in the momentum space k , using three material parameters γ_1 , γ_2 and γ_3

(which are related to inverse effective masses at the Brillouin zone center):

$$P = -\left(\frac{\hbar^2}{2m_0}\right)\gamma_1(k_x^2 + k_y^2 + k_z^2), \quad (2.39)$$

$$Q = -\left(\frac{\hbar^2}{2m_0}\right)\gamma_2(k_x^2 + k_y^2 - 2k_z^2), \quad (2.40)$$

$$R = -\left(\frac{\hbar^2}{2m_0}\right)\sqrt{3}[-\gamma_2(k_x^2 - k_y^2) + 2i\gamma_3k_xk_y], \quad (2.41)$$

$$S = \left(\frac{\hbar^2}{2m_0}\right)2\sqrt{3}\gamma_3(k_x - ik_y)k_z. \quad (2.42)$$

It is worth giving some attention to these terms, because they summarize our understanding of the influence of the confinement shape and strain on the valence band in a very compact way. We recall then the strain Hamiltonian with analogue terms to the previous Hamiltonian in eq. 2.38

$$H_{strain} = \begin{pmatrix} P_\epsilon + Q_\epsilon & S_\epsilon & R_\epsilon & 0 \\ S_{\epsilon^\dagger} & P_\epsilon - Q_\epsilon & 0 & R_\epsilon \\ R_{\epsilon^\dagger} & 0 & P_\epsilon - Q_\epsilon & -S_\epsilon \\ 0 & R_{\epsilon^\dagger} & -S_{\epsilon^\dagger} & P_\epsilon + Q_\epsilon \end{pmatrix} \quad (2.43)$$

Here, the matrix elements are expressed with the Bir-Pikus deformation potentials⁴³ a_v , b , d and the momentum k is replaced with the strain tensor elements ϵ_{ij} :

$$P_\epsilon = a_v(\epsilon_{xx} + \epsilon_{yy} + \epsilon_{zz}) = a_v\epsilon_{vol}, \quad (2.44)$$

$$Q_\epsilon = \frac{b}{2}(\epsilon_{xx} + \epsilon_{yy} - 2\epsilon_{zz}) = -b\epsilon_{ax}, \quad (2.45)$$

$$R_\epsilon = -\frac{\sqrt{3}}{2}b(\epsilon_{xx} - \epsilon_{yy}) - id\epsilon_{xy} \quad (2.46)$$

$$S_\epsilon = -d(\epsilon_{zx} - i\epsilon_{yz}). \quad (2.47)$$

Both the axial b and hydrostatic a_v deformation potentials have negative values (for e.g. GaAs $a_v = -8.0$ and $b = -1.7^{44}$).

Let us first consider diagonal terms in the Luttinger-Kohn Hamiltonian which set the splitting between the HH and LH bands. In a bulk, unstrained semiconductor, at Γ point where $k = 0$, the expression in eq. 2.40 for Q becomes zero. The HH and LH bands are therefore degenerate. The hydrostatic strain ϵ_{vol} influences the bandgap of the semiconductor by shifting the valence band edge with respect to the conduction band edge, as apparent from the expression for P_ϵ (eq. 2.44). Biaxial compressive strain ($\epsilon_{xx}, \epsilon_{yy} < 0$ and $\epsilon_{zz} > 0$) gives a positive value of Q_ϵ (eq. 2.45), lifting the HH band above the LH band. The situation is reversed for biaxial tensile strain. These effects are summarized in fig. 2.5(b). The hydrostatic component of the compressive

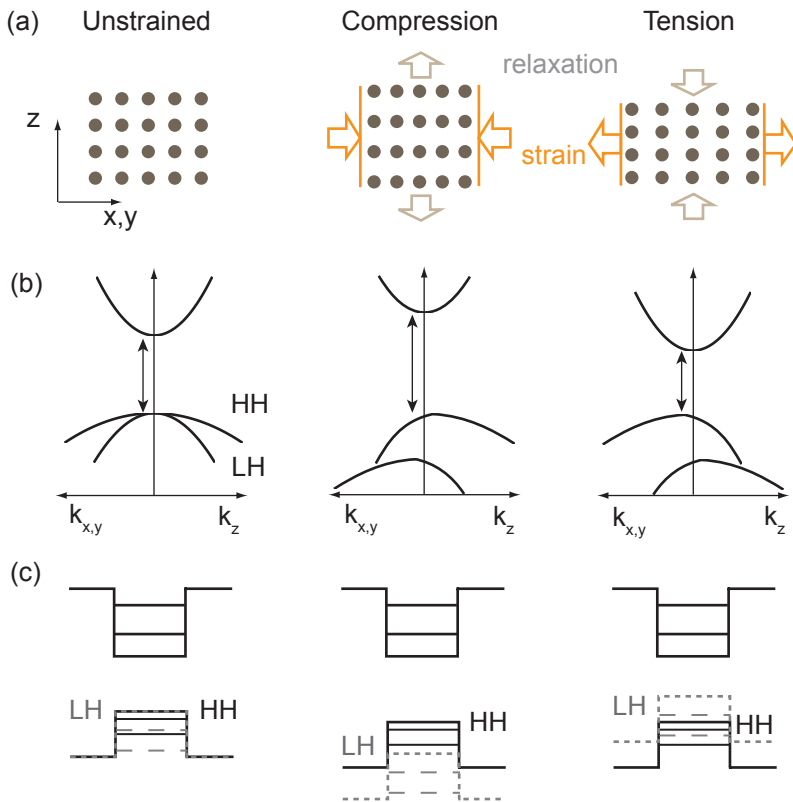


Figure 2.5 | (a) A schematic representation of the unstrained lattice and the compressive/tensile strain. (b) The influence of strain on the bulk semiconductor bandgap, the conduction band and both HH and LH hole subbands. (c) The influence of strained on the energy levels in quantum confinement.

(tensile) strain increases (decreases) the bandgap. In the case of compression, the highest band is heavy along k_z and lighter along $k_{x,y}$. On the other hand, tensile strain gives the highest band being light along k_z .

2.3.2 Heavy and light hole spin mixing in quantum dots

Our considerations bring us now to the case of a confined nanostructure, a quantum dot. Usually, confinement in quantum dots is the strongest in z direction. If h is the height of a quantum dot, l_x and l_y denote its lateral size, then $k_z \sim \frac{1}{h}$ is dominant over $k_x \sim \frac{1}{l_x}$ and $k_y \sim \frac{1}{l_y}$. It is then easy to see why in flat quantum dots the HH states are above the LH states: the term Q (eq. 2.40) is positive. Increasing the height of the QD can push the LH subband closer to the HH⁴⁵. This is the reason why the LH admixture to the hole state is high for dots resembling nanorods^{46–48}. Confined states in a usual, flat quantum dot ($h < l_x, l_y$) are shown in fig. 2.5. In an unstrained quantum dot the ground state has a heavy character. Compressive strain separates further the confining potential for the HH and the LH, so the splitting becomes even larger (the case for Stransky-Krastanov quantum dots). Biaxial tensile strain is predicted to reverse the order of hole subbands also in a quantum dot. We have verified this prediction and obtained quantum dots with over 95% purity LH state using tensile strain of 0.36% (see chapter 5).

It is important to note, that biaxial strain will only change the splitting between the HH and LH states, but will not mix the spin states. Only if strain is not uniform, so that $\epsilon_{xx} \neq \epsilon_{yy}$ then the mixing term R_ϵ is non zero. R_ϵ couples the HH state $|\frac{3}{2}, \frac{3}{2}\rangle$ with the LH state $|\frac{3}{2}, -\frac{1}{2}\rangle$ (as well as $|\frac{3}{2}, -\frac{3}{2}\rangle$ with $|\frac{3}{2}, \frac{1}{2}\rangle$). The mixed hole states can be written as:

$$|h_1^R\rangle = \alpha \left| \frac{3}{2}, +\frac{3}{2} \right\rangle + \beta \left| \frac{3}{2}, -\frac{1}{2} \right\rangle, \quad (2.48)$$

$$|h_2^R\rangle = \alpha \left| \frac{3}{2}, -\frac{3}{2} \right\rangle + \beta \left| \frac{3}{2}, +\frac{1}{2} \right\rangle. \quad (2.49)$$

Both hole spin components in state $|h_1^R\rangle$ recombine with the same electron spin ($|\frac{1}{2}, -\frac{1}{2}\rangle \equiv |\downarrow\rangle$), but the HH recombination gives a σ^+ polarized photon, whereas the LH recombination results in a σ^- photon. In a general situation of this HH-LH mixing, an elliptical polarization from the exciton emission should be observed:

$$|h_1^R\rangle |\downarrow\rangle \rightarrow \alpha \sigma^+ + \frac{\beta}{\sqrt{3}} \sigma^-, \quad (2.50)$$

$$|h_2^R\rangle |\uparrow\rangle \rightarrow \alpha \sigma^- + \frac{\beta}{\sqrt{3}} \sigma^+. \quad (2.51)$$

We can also consider two more excitons composed of the $|h_1^R\rangle$ and $|h_2^R\rangle$:

$$|h_1^R\rangle |\uparrow\rangle \rightarrow \alpha |dark\rangle + \frac{2\beta}{\sqrt{3}}z, \quad (2.52)$$

$$|h_2^R\rangle |\downarrow\rangle \rightarrow \alpha |dark\rangle + \frac{2\beta}{\sqrt{3}}z. \quad (2.53)$$

where the optical recombination with the HH spin component is dipole forbidden and the LH component gives a z -polarized photon. In conclusion, HH-LH mixing can be manifested by (i) the ellipticity of the exciton polarization and (ii) by the weak z polarized emission of exciton dark states. The same effect of the hole spin mixing can be caused also by in plane shape elongation, as apparent from the term R (eq. 2.41) in the Luttinger-Kohn Hamiltonian. The impact of the HH-LH mixing caused by the shape asymmetry of strain free GaAs QDs has been reported by T. Belhadj *et al.*⁴⁹. The effects of strain and QD shape on the polarization anisotropy of InAs QDs were described also by C. Tonin *et al.*⁵⁰

There is yet another term S (eq. 2.42) that couples different pairs of the HH and LH spins and gives the following hole mixture:

$$|h_1^S\rangle = \alpha \left| \frac{3}{2}, +\frac{3}{2} \right\rangle + \beta \left| \frac{3}{2}, +\frac{1}{2} \right\rangle, \quad (2.54)$$

$$|h_2^S\rangle = \alpha \left| \frac{3}{2}, -\frac{3}{2} \right\rangle + \beta \left| \frac{3}{2}, -\frac{1}{2} \right\rangle. \quad (2.55)$$

The polarization fingerprint of the two exciton states composed of the hole $|h_1^S\rangle$ and $|h_2^S\rangle$ states is the admixture of z polarization to circularly polarized states and vice versa. At the same time two dark states acquire some circular polarization:

$$|h_1^S\rangle |\uparrow\rangle \rightarrow \alpha |dark\rangle + \frac{\beta}{\sqrt{3}}\sigma^+, \quad (2.56)$$

$$|h_1^S\rangle |\downarrow\rangle \rightarrow \alpha\sigma^+ + \frac{2\beta}{\sqrt{3}}z, \quad (2.57)$$

$$|h_2^S\rangle |\uparrow\rangle \rightarrow \alpha\sigma^- + \frac{2\beta}{\sqrt{3}}z, \quad (2.58)$$

$$|h_2^S\rangle |\downarrow\rangle \rightarrow \alpha |dark\rangle + \frac{\beta}{\sqrt{3}}\sigma^-. \quad (2.59)$$

It has been observed in several experiments (e.g. ref.^{5,51}) that the HH exciton dark state transition is not strictly forbidden and reveals in-plane polarization. It is very likely that this effect originates from the coupling term S (eq. 2.42) in the Luttinger-Kohn Hamiltonian, that is sensitive to the quantum dot confinement anisotropy.

Usually, it was assumed, that the coupling term S is negligible compared to R .⁵² Also, strain is unlikely to result in HH-LH mixing described in eq. 2.55, because only shear strain can cause such effect (see eq. 2.47). However, it is difficult to draw any general conclusions for quantum dots, since different growth methods can result in various shape and strain characteristics. In chapter 6, very pronounced HH-LH mixing due to the S and/or S_c term is shown for epitaxial GaAs quantum dots, where tensile strain can be induced in order to switch LHs to the ground state.

2.4 Quantum dots as sources of nonclassical photons

A single photon is an energy quantum of the electromagnetic field. Hundred years ago Max Planck realized that the electromagnetic field has to be quantized in order to properly describe the black body radiation and save us from the so called "ultraviolet catastrophe". Nowadays, we learn how to employ single photons in proposals where the transfer of quantum information is required. Single photons are an ideal platform for quantum communication transfer over long distance due to their weak coupling to the environment. Therefore, on demand, controllable single photon generation is required in numerous experiments. In 1984, Bennett and Brassard proposed a protocol for secret key distribution⁵³ that uses the single-particle character of a photon to avoid any possibility of eavesdropping on an encoded message. The preparation of a single- or few-photon states on demand is also required for quantum repeaters⁵⁴, and quantum teleportation⁵⁵. Photons as flying qubits can serve as information carriers in scalable quantum networks between processing nodes consisting of stationary qubits (like quantum dots, NV centers, atoms). In this work, however, we employ single photons to test one of the most striking properties of quantum mechanics - non-locality.

Quantum dots are natural single photon sources, since recombination of a single electron-hole pair results in one photon⁵⁶. There are ongoing efforts to increase the collection efficiency from quantum dots single photon collection. On the one hand, the emission of photons can be directed by cavities⁵⁷ or waveguiding effects in nanowires^{58,59} or micropillars⁶⁰. On the other hand, the emission profile can be shaped to match a Gaussian profile, hence achieve optimal coupling to the fiber. In this work we have used GaAs/AlGaAs quantum dots embedded in a weak cavity. In the following paragraphs we will focus on the properties of single photons, rather than the source.

2.4.1 Photon statistics

Photons are bosons, implying that there is no restriction on the number of photons that can occupy the same quantum state. The bosonic nature of photons is demonstrated in the coherent state (e.g. laser light). The coherent state is described by poissonian

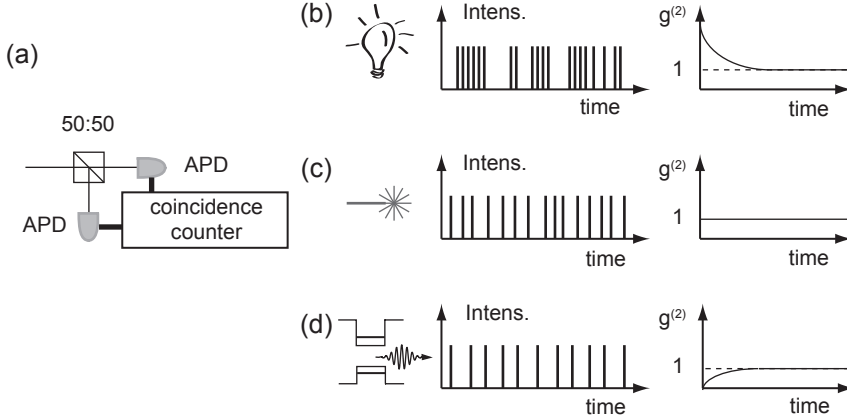


Figure 2.6 | (a) Set up of a Hanbury-Brown and Twiss experiment, including a 50:50 beam splitter and start- and stop- single photon detectors modules. Photon counting events and corresponding second order correlation functions for (b) a classical thermal source (light bulb), (c) coherent light (laser) and (d) a single photon source.

statistics:

$$|\alpha\rangle = e^{-\frac{|\alpha|^2}{2}} \sum_{n=0}^{\infty} \frac{\alpha^n}{\sqrt{n!}} |n\rangle, \quad (2.60)$$

where $|n\rangle$ is a photon number state (a Fock state). A coherent state is defined as an eigenstate of the the annihilation operator \hat{a} :

$$\hat{a} |\alpha\rangle = \alpha |\alpha\rangle. \quad (2.61)$$

We require photons from a single photon source to follow completely different statistics. There should be not more than just one photon produced by the source at a time. In other words, the stream of photons from a single photon source should be antibunched. Single photon states are described by a Fock state, which is an eigenstate of the photon number operator $\hat{N} = \hat{a}^\dagger \hat{a}$:

$$\hat{N} |n\rangle = n |n\rangle. \quad (2.62)$$

The second order correlation function, $g_2(t)$, describes the photon statistics:

$$g^{(2)}(t, t') = \frac{\langle \hat{a}^\dagger(t) \hat{a}^\dagger(t') \hat{a}(t) \hat{a}(t') \rangle}{\langle \hat{a}^\dagger(t) \hat{a}(t) \rangle \langle \hat{a}^\dagger(t') \hat{a}(t') \rangle} = \frac{\langle \hat{I}(t) \hat{I}(t') \rangle}{\langle \hat{I}(t) \rangle \langle \hat{I}(t') \rangle}, \quad (2.63)$$

where $\hat{I}(t)$ is the time dependent intensity operator of mode \hat{a} . The Hanbury-Brown and Twiss setup for the second order correlation function measurement is shown in

fig. 2.6(a). The beam of photons is split in two with a 50:50 beam splitter and counts in each path are recorded with single photon detectors (e.g. avalanche photon detectors (APDs) or superconducting single photon detectors (SSPDs)). Coincidences are binned into a histogram using a coincidence module. A second order correlation measurement allows us to differentiate between different sources of photons. A thermal source emitting bunched photons shows an enhancement in $g^{(2)}$ near zero delay (fig. 2.6(b)). Sources with a Poisson distribution (lasers) have a flat correlation function as shown in fig. 2.6(c). A single mode quantum field with photon number variance $V(n)$ and mean \bar{n} obeys:

$$g^{(2)}(0) = 1 + \frac{V(n) - \bar{n}}{\bar{n}^2} \quad (2.64)$$

For an eigenstate of the photon number operator (or Fock state), this yields $g^{(2)}(0) = 1 - 1/n$. Therefore for a single photon emitter $g^{(2)}(0) = 0$.

2.4.2 Single photon coherence

One of the key challenges in the development of the quantum network with quantum dots is generation of high quality single photons with high efficiency, coherence, and purity (i.e., suppressed multi-photon emission). In a previous section we have shown how a second order correlation function quantifies the purity of a single photon emission. In this section we focus on coherence of single photons which is assessed by a first order correlation function:

$$g^{(1)}(t, t') = \frac{\langle \hat{a}^\dagger(t) \hat{a}(t') \rangle}{\langle \hat{a}^\dagger(t) \hat{a}(t) \rangle} \quad (2.65)$$

The first order correlation function measures the capability of the single photon field coming from two different time-space points to form interference fringes when superposed. In practice, we use a Michelson interferometer to perform a first order correlation measurement. A schematic view of the experimental setup is depicted in fig. 2.7 (a). The quantum dot emission is directed to a nonpolarizing beam splitter. After the beamsplitter, the single-photon field takes both pathways towards the fixed mirror M1 and movable mirror M2. When the path difference between mirrors is within the coherence length of the emitted photons we observe single-photon interference effects through variations in the observed intensity at the output of the Michelson interferometer where the charge-coupled device (CCD) camera is positioned. We measure the visibility of the interference fringes defined as:

$$V = |g^{(1)}(t)| = \frac{I_{max} - I_{min}}{I_{max} + I_{min}}. \quad (2.66)$$

The visibility decreases with increasing delay between the two arms of the interferometer, as apparent from a comparison of the fringes in fig. 2.7 (b) and (c). For light

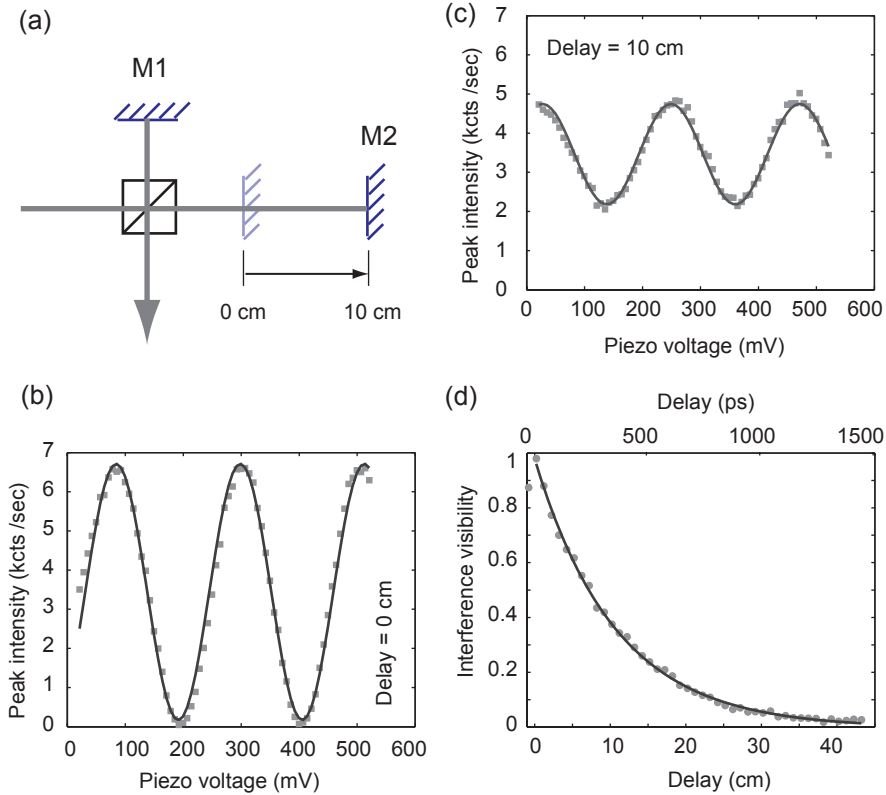


Figure 2.7 | (a) Schematic of a Michelson interferometer. The electromagnetic field is split at a non polarizing 50:50 beamsplitter and then reflected back from mirrors M1 (fixed) and M2 (movable, a motor stage for translations in a cm range, a piezo stage for fine translations). The fields coalesce at the beamsplitter and the interference fringes are formed when the relative path difference between the arms is changed with M2. (b) High visibility of interference is observed when there is no path difference between the two arms of the interferometer and (c) decreased visibility for 10 cm delay due to finite coherence of the photons. In (b) and (c) the subwavelength M2 translation scales with the piezo voltage. (d) Exponential decay of the visibility for photons of 10.7 cm coherence length translates to $T_2 = 357$ ps.

with Lorentzian lineshape the visibility decays exponentially with a time constant T_2 (coherence time)

$$V = e^{-\frac{t}{T_2}}. \quad (2.67)$$

Theoretical upper limit on the coherence time T_2 is set by twice the relaxation time T_1 (for a Fourier limited dot $T_2 = 2T_1$ holds). However, in practice the coherence of single photons from a quantum dot is below the Fourier limit due to dephasing processes characterized by T_2^* time:

$$\frac{1}{T_2} = \frac{1}{2T_1} + \frac{1}{T_2^*}. \quad (2.68)$$

Dephasing is caused by interactions with the environment, therefore the above bandgap excitation bringing excess energy to the system influences the coherence properties. It has been shown that quantum dot photons can approach the Fourier limit ($T_2/(2T_1) > 0.9$) in resonant⁶¹ and pulsed excitation⁶². Also, a general strategy to approach the Fourier limit is to embed the quantum dots in microcavities in order to accelerate the spontaneous emission rate and have less time to interact with the environment⁶³.

2.4.3 Single photon non-locality

non-locality is one of the most striking features of quantum mechanics. We are used to thinking about non-locality in the context of at least two entangled particles that share a nonlocal property (like polarization of entangled photons). Here we explore the concept of non-locality of a single particle. In other words, we pose the question: can we violate a Bell-type inequality with only one particle? In this work we aim at realizing a proposal introduced by S. M. Tan, D. F. Walls and M. J. Collet⁶⁴. A single photon generated in a quantum dot and then sent at the beam splitter will be our single particle testing quantum mechanical predictions. After the beam splitter, a single photon field is present in two paths (denoted as b_1 and b_2):

$$|\Psi\rangle = \frac{1}{\sqrt{2}}(i|1\rangle_{b_1} |0\rangle_{b_2} + |0\rangle_{b_1} |1\rangle_{b_2}). \quad (2.69)$$

This state is mathematically isomorphic to any other form of an entangled state. If we placed, e.g. an atom in each path, whose spin state depends on the absorption of the photon, then we would be able to map the state in eq. 2.69 into a spin entangled state. However, here, we want to prove entanglement of the two modes of the electromagnetic field when only one photon is present, not entanglement in any other physical system. Therefore we must think of a way to perform a Bell test for a state in eq. 2.69. How can we measure correlations in the Fock space spanned by zero and one photon? Let us first gain more insight into a situation, where a single photon takes two paths. This

is actually a well studied concept. In Young's experiment, a single photon has to pass simultaneously through two slits in order to explain the observed interference pattern. Similarly, in optical interferometers a single photon interferes with itself. These examples show, that measuring wave-like properties of a single photon (interference) is the way to proceed if we want to verify a simultaneous presence of a single photon in two different paths. However, we do not want to interfere two paths with each other. Ideally the two paths b_1 and b_2 should be separated far enough to lie outside each other's light cones in order to exclude any communication between them. In our experiment we will not yet fulfill this condition. However, in principle there is nothing fundamental preventing us from bringing the paths at arbitrary large distance. In each path we place a homodyne detector. A homodyne detector consists of a 50:50 beam splitter, a coherent local oscillator with amplitude $\alpha_k = \alpha e^{i\theta_k}$ ($k = 1, 2$) and two photodetectors in the output ports. A schematic of the experiment is shown in fig. 3.1(a). The local oscillator is a coherent state with $|\alpha| < 1$, hence the average photon number also smaller than one $|\alpha|^2 < 1$. The role of the local oscillator is to provide a common reference frame for the two paths with a single photon field. The phase of a local oscillator is equivalent to the angle of the polarizers in the standard Bell test for polarization entangled photon pairs. In order to perform a Bell test, one has to look at coincidences between two detectors, let us choose D2 and D3 in fig. 3.1(a). Obviously, since $g^{(2)}(0) = 0$ for a single photon, we will not observe any coincidence counts originating only from a single photon source. However, when the local oscillator is present, then the two fields (single photon and local oscillator) mix at the beam splitter. The probability of interference is proportional to the fields' amplitude in each path:

$$P_{interference} = \frac{1}{2}|\alpha|^2, \quad (2.70)$$

where a fraction $\frac{1}{2}$ comes from the single photon field amplitude in eq. 2.69 and $|\alpha|^2$ comes from the local oscillator field. Constructive/ destructive interference in paths to detectors D2 and D3, depends on the relative phase of the local oscillator $\theta = \theta_2 - \theta_1$:

$$\langle I_{D2}I_{D3} \rangle_{interference} = \frac{1}{2}|\alpha|^2 \sin^2\left(\frac{\pi}{4} + \frac{\theta}{2}\right), \quad (2.71)$$

where $\langle I_{D2}I_{D3} \rangle_{interference}$ denotes a probability that both detectors D_2 and D_3 simultaneously record a detection event resulting from interference. A derivation of this formula can be found in the original proposal⁶⁴. As apparent from eq. 2.70, the probability of interference increases with increasing local oscillator amplitude. However, there is a trade off. The overall visibility of interference decreases, because the local oscillator gives constant coincidence background counts $\frac{1}{2}|\alpha|^2 \times \frac{1}{2}|\alpha|^2$ as shown in fig. 3.1(b). Therefore the total coincidence count rate seen by the D2 and D3 detectors is:

$$\langle D_2D_3 \rangle_{total} = \frac{1}{4}|\alpha|^4 + \frac{1}{2}|\alpha|^2 \sin^2\left(\frac{\pi}{4} + \frac{\theta}{2}\right). \quad (2.72)$$

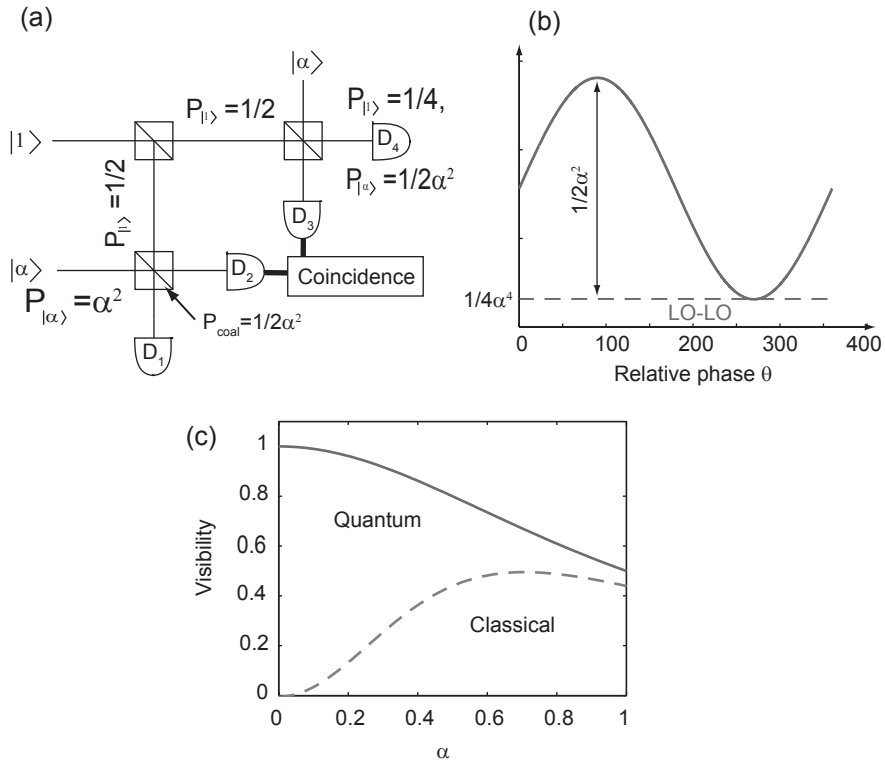


Figure 2.8 | (a) Schematic of the experimental set-up capable of performing measurements complementary to photon number measurements. A single photon field is split in two paths, such that the probability of finding a photon in each of them is $1/2$. A single photon is detected by only one detector at a time (with probability $1/4$) and does not give coincidence counts. The local oscillator (LO) gives a constant count rate in each of the detectors (probability $1/2|\alpha|^2$) resulting in a constant coincidence count rate ($1/4|\alpha|^4$). The interference of the single photon field with the local oscillator is manifested by the LO phase dependant coincidences. (b) Expected EPR-like correlations among two detectors for $|\alpha| = 0.5$. (c) Visibility as a function of the local oscillator amplitude $|\alpha|$ in the case of a quantum, non-local particle and a classical wave.

As apparent from this formula, the coincidences originating from the local oscillator increase with its amplitude faster, than the interference probability. We can derive a formula for the visibility interference as a function of $|\alpha|$:

$$V = \frac{1}{|\alpha|^2 + 1}. \quad (2.73)$$

S. M. Tan *et al.*⁶⁴ have contrasted the concept of quantum non-locality of a single photon with a naive classical field theory. Let us replace the single photon input in fig. 3.1(a) with a classical wave of amplitude β and unspecified phase $\beta e^{(\pm i\Phi)}$. We should still expect to see the interference fringes, however, the visibility would decrease:

$$V = \frac{\rho}{\rho^2 + \rho + \frac{1}{4}}, \quad (2.74)$$

where $\rho = (|\alpha|/|\beta|)^2$. In fig. 3.1(c) we plot the interference visibility versus local oscillator amplitude $|\alpha|$. In the case of quantum non-locality the visibility increases with decreasing $|\alpha|$. For a classical case (we assumed $|\beta| = 1$) the trend is non monotonic and the maximal visibility does not exceed 50%. So far we have not yet discussed, how we can violate the Bell inequality with a single photon. The coincidence curve in fig. 3.1(b) shows the Einstein-Podolsky-Rosen type of correlations. For such correlations the Bell inequality is violated if the visibility exceeds 71% ($> 1/\sqrt{2}$).

In conclusion, in order to verify single photon entanglement in two modes, we can not look at the particle-like properties at two distant locations, but at the wave-like properties of a single photon. Hence, a measurement of wave-like properties of a single photon requires a reference oscillator (additional photons!). This is the reason why this concept has raised many controversies⁶⁵. Is it really a single particle non-locality? The nonlocal properties in this measurement depend on the presence of a single particle. Therefore all the nonlocal correlations are carried by the single particle state, although the observation of these correlations requires auxiliary reference particles.

2.5 Conclusion

We have discussed the properties of electron and hole spins in semiconductor quantum dots. The HH spin emerges as the optimal candidate for a robust qubit used for information processing (longest T_2), whereas the electron spin performs better as a quantum memory (longest T_1). However, there is a possibility to enhance the HH relaxation time T_1 by engineering the shape of quantum dot confining potential.

Naturally, a question arises: what is the LH spin good for? The implementation of the photon to spin coherent transfer proposal²⁴ seems troublesome, considering our demonstration of an enormous LH exciton exchange interaction. However, there is another advantage of LH spins over the HH spins that remains, regardless the magnitude of the electron-hole exchange. The LH spin, in contrast to the HH spin,

couples directly to the radio frequency (RF) magnetic field, hence enabling on-chip spin manipulation⁶⁶. This fact becomes apparent from a perturbation term in the presence of the RF field:

$$H'(t) = \frac{1}{2}g\mu_B B_x e^{i\omega t} J_x, \quad (2.75)$$

where g is the spin g -factor for holes and B_x is a small RF field that oscillates at frequency ω . The frequency ω equals the energy spacing between two qubit states and the RF field applied for a time τ rotates the qubit state into a coherent superposition state. For a HH subspace, $J_{hh,x}$ is simply zero (see the appendix A), whereas for a LH subspace $J_{lh,x}$ has a form of a Pauli matrix σ_x . Therefore the HH spin can couple to the RF field only indirectly, via spin mixing with the LH (the possible origins of this mixing are discussed in chapter 6). In summary, the HH and LH spins are complementary if we consider different spin manipulation schemes. The HH spin, thanks to its clear optical selection rules is ideal for all-optical manipulation, whereas the LH spin opens up a possibility of fast electrical spin manipulation. In these examples high purity of hole spin states is necessary, therefore the quantum dot shape and strain distribution must be uniform.

Finally, we have characterized basic properties of single photons generated in a quantum dot. We are witnessing a very promising time for quantum dots as single photon emitters, since in recent years we have learnt how to approach the Fourier limit^{61,62}. We are in possession of all the tools to enter a level of quantum experiments with coherent single photons from quantum dots. In this thesis we will test the single photon non-locality using quantum dots as controllable single photon sources. Previously, non-locality has been demonstrated for photons generated in a parametric downconversion source⁶⁷.

2.6 Bibliography

- [1] D. A. Broido and L. J. Sham. Effective masses of holes at GaAs – AlGaAs heterojunctions. *Phys. Rev. B* **31**, 888 (1985).
- [2] A. V. Koudinov, I. A. Akimov, Y. G. Kusrayev and F. Henneberger. Optical and magnetic anisotropies of the hole states in stranski-krastanov quantum dots. *Phys. Rev. B* **70**, 241305 (2004).
- [3] Y. Léger, L. Besombes, L. Maingault and H. Mariette. Valence-band mixing in neutral, charged, and Mn-doped self-assembled quantum dots. *Phys. Rev. B* **76**, 045331 (2007).
- [4] T. Belhadj *et al.* Impact of heavy hole-light hole coupling on optical selection rules in gaas quantum dots. *Applied Physics Letters* **97**, 051111 (2010).
- [5] D. Krizhanovskii *et al.* Individual neutral and charged $\text{In}_x\text{Ga}_{1-x}\text{As}$ – GaAs quantum dots with strong in-plane optical anisotropy. *Physical Review B* **72**, 161312 (2005).
- [6] D. J. Hilton and C. L. Tang. Optical orientation and femtosecond relaxation of spin-polarized holes in gaas. *Phys. Rev. Lett.* **89**, 146601 (2002).
- [7] P. Roussignol *et al.* Hole polarization and slow hole-spin relaxation in an n -doped quantum-well structure. *Phys. Rev. B* **46**, 7292 (1992).
- [8] D. Heiss *et al.* Observation of extremely slow hole spin relaxation in self-assembled quantum dots. *Phys. Rev. B* **76**, 241306 (2007).
- [9] L. M. Woods, T. L. Reinecke and R. Kotlyar. Hole spin relaxation in quantum dots. *Phys. Rev. B* **69**, 125330 (2004).
- [10] D. V. Bulaev and D. Loss. Spin relaxation and decoherence of holes in quantum dots. *Phys. Rev. Lett.* **95**, 076805 (2005).
- [11] M. Kroutvar *et al.* Optically programmable electron spin memory using semiconductor quantum dots. *Nature* **432**, 81 (2004).
- [12] D. Brunner *et al.* A coherent single-hole spin in a semiconductor. *Science* **325**, 70 (2009).
- [13] J. Fischer, W. Coish, D. Bulaev and D. Loss. Spin decoherence of a heavy hole coupled to nuclear spins in a quantum dot. *Physical Review B* **78**, 155329 (2008).
- [14] C. Testelin, F. Bernardot, B. Eble and M. Chamarro. Hole spin dephasing time associated with hyperfine interaction in quantum dots. *Phys. Rev. B* **79**, 195440 (2009).

- [15] P. Fallahi, S. T. Yılmaz and A. Imamoglu. Measurement of a heavy-hole hyperfine interaction in InGaAs quantum dots using resonance fluorescence. *Phys. Rev. Lett.* **105**, 257402 (2010).
- [16] E. A. Chekhovich, A. B. Krysa, M. S. Skolnick and A. I. Tartakovskii. Direct measurement of the hole-nuclear spin interaction in single InP/GaInP quantum dots using photoluminescence spectroscopy. *Phys. Rev. Lett.* **106**, 027402 (2011).
- [17] E. Chekhovich *et al.* Element-sensitive measurement of the hole-nuclear spin interaction in quantum dots. *Nature Physics* **9**, 74 (2012).
- [18] A. J. Ramsay *et al.* Fast optical preparation, control, and readout of a single quantum dot spin. *Phys. Rev. Lett.* **100**, 197401 (2008).
- [19] B. D. Gerardot *et al.* Optical pumping of a single hole spin in a quantum dot. *Nature* **451**, 441 (2008).
- [20] K. De Greve *et al.* Ultrafast coherent control and suppressed nuclear feedback of a single quantum dot hole qubit. *Nature Physics* **7**, 872 (2011).
- [21] T. M. Godden *et al.* Coherent optical control of the spin of a single hole in an InGaAs quantum dot. *Phys. Rev. Lett.* **108**, 017402 (2012).
- [22] W. Gao, P. Fallahi, E. Togan, J. Miguel-Sanchez and A. Imamoglu. Observation of entanglement between a quantum dot spin and a single photon. *Nature* **491**, 426 (2012).
- [23] K. De Greve *et al.* Quantum-dot spin-photon entanglement via frequency down-conversion to telecom wavelength. *Nature* **491**, 421 (2012).
- [24] R. Vrijen and E. Yablonovitch. A spin-coherent semiconductor photo-detector for quantum communication. *Physica E: Low-dimensional Systems and Nanostructures* **10**, 569 (2001).
- [25] M. W. Berz, L. C. Andreani, E. F. Steigmeier and F.-K. Reinhart. Exchange splitting of light hole excitons in AlGaAs-GaAs quantum wells. *Solid state communications* **80**, 553 (1991).
- [26] B. Blinov, D. Moehring, L.-M. Duan and C. Monroe. Observation of entanglement between a single trapped atom and a single photon. *Nature* **428**, 153 (2004).
- [27] J. Volz *et al.* Observation of entanglement of a single photon with a trapped atom. *Physical review letters* **96**, 030404 (2006).
- [28] T. Wilk, S. C. Webster, A. Kuhn and G. Rempe. Single-atom single-photon quantum interface. *Science* **317**, 488 (2007).

-
- [29] E. Togan *et al.* Quantum entanglement between an optical photon and a solid-state spin qubit. *Frontiers in Optics*. Optical Society of America (2011).
- [30] S. Olmschenk *et al.* Quantum teleportation between distant matter qubits. *Science* **323**, 486 (2009).
- [31] W. Gao *et al.* Quantum teleportation from a propagating photon to a solid-state spin qubit. *Nature communications* **4** (2013).
- [32] M. Tchernycheva *et al.* Growth and characterization of inp nanowires with inasp insertions. *Nano Letters* **7**, 1500 (2007).
- [33] F. Boxberg, N. Søndergaard and H. Q. Xu. Photovoltaics with piezoelectric core-shell nanowires. *Nano Letters* **10**, 1108 (2010).
- [34] E. P. O'Reilly. Valence band engineering in strained-layer structures. *Semiconductor Science and Technology* **4**, 121 (1989).
- [35] G. Bester. Electronic excitations in nanostructures: an empirical pseudopotential based approach. *Journal of Physics: Condensed Matter* **21**, 023202 (2009).
- [36] G. Bester, S. Nair and A. Zunger. Pseudopotential calculation of the excitonic fine structure of million-atom self-assembled $\text{In}_{1-x}\text{Ga}_x\text{As}/\text{GaAs}$ quantum dots. *Physical Review B* **67**, 161306 (2003).
- [37] R. Singh and G. Bester. Nanowire quantum dots as an ideal source of entangled photon pairs. *Phys. Rev. Lett.* **103**, 063601 (2009).
- [38] S. Lee, L. Jönsson, J. W. Wilkins, G. W. Bryant and G. Klimeck. Electron-hole correlations in semiconductor quantum dots with tight-binding wave functions. *Phys. Rev. B* **63**, 195318 (2001).
- [39] W. Jaskólski, M. Zieliński, G. W. Bryant and J. Aizpurua. Strain effects on the electronic structure of strongly coupled self-assembled InAs/GaAs quantum dots: Tight-binding approach. *Phys. Rev. B* **74**, 195339 (2006).
- [40] M. Zieliński, M. Korkusiński and P. Hawrylak. Atomistic tight-binding theory of multiexciton complexes in a self-assembled inas quantum dot. *Physical review. B, Condensed matter and materials physics* **81**, 085301 (2010).
- [41] J. M. Luttinger and W. Kohn. Motion of electrons and holes in perturbed periodic fields. *Phys. Rev.* **97**, 869 (1955).
- [42] J. M. Luttinger. Quantum theory of cyclotron resonance in semiconductors: General theory. *Phys. Rev.* **102**, 1030 (1956).
- [43] G. L. Bir, G. E. Pikus, P. Shelnitz and D. Louvish. *Symmetry and strain-induced effects in semiconductors*, volume 624. Wiley New York (1974).

- [44] N. Data. Functional relationships in science and technology, edited by o. madelung, landolt-börnstein, new series, group iii, vol. 17, pt. a (1982).
- [45] T. Tanaka, J. Singh, Y. Arakawa and P. Bhattacharya. Near band edge polarization dependence as a probe of structural symmetry in gaas/algaas quantum dot structures. *Applied physics letters* **62**, 756 (1993).
- [46] L. Li *et al.* Control of polarization and dipole moment in low-dimensional semiconductor nanostructures. *Applied Physics Letters* **95**, 221116 (2009).
- [47] P. Ridha *et al.* Polarization properties of columnar quantum dots: effects of aspect ratio and compositional contrast. *Quantum Electronics, IEEE Journal of* **46**, 197 (2010).
- [48] V. Troncale, K. Karlsson, E. Pelucchi, A. Rudra and E. Kapon. Control of valence band states in pyramidal quantum dot-in-dot semiconductor heterostructures. *Applied Physics Letters* **91**, 241909 (2007).
- [49] T. Belhadj *et al.* Impact of heavy hole-light hole coupling on optical selection rules in gaas quantum dots. *Applied Physics Letters* **97**, 051111 (2010).
- [50] C. Tonin *et al.* Polarization properties of excitonic qubits in single self-assembled quantum dots. *Physical Review B* **85**, 155303 (2012).
- [51] E. A. Chekhovich, A. B. Krysa, M. S. Skolnick and A. I. Tartakovskii. Direct measurement of the hole-nuclear spin interaction in single InP/GaInP quantum dots using photoluminescence spectroscopy. *Phys. Rev. Lett.* **106**, 027402 (2011).
- [52] C. Lü, J. Cheng and M. Wu. Hole spin relaxation in semiconductor quantum dots. *Physical Review B* **71**, 075308 (2005).
- [53] C. H. Bennett, G. Brassard *et al.* Quantum cryptography: Public key distribution and coin tossing. *Proceedings of IEEE International Conference on Computers, Systems and Signal Processing*. New York (1984), volume 175.
- [54] H.-J. Briegel, W. Dür, J. I. Cirac and P. Zoller. Quantum repeaters: The role of imperfect local operations in quantum communication. *Phys. Rev. Lett.* **81**, 5932 (1998).
- [55] D. Bouwmeester *et al.* Experimental quantum teleportation. *Nature* **390**, 575 (1997).
- [56] P. Michler *et al.* A quantum dot single-photon turnstile device. *Science* **290**, 2282 (2000).
- [57] M. Pelton *et al.* Efficient source of single photons: A single quantum dot in a micropost microcavity. *Phys. Rev. Lett.* **89**, 233602 (2002).

- [58] J. Claudon *et al.* A highly efficient single-photon source based on a quantum dot in a photonic nanowire. *Nature Photonics* **4**, 174 (2010).
- [59] M. E. Reimer *et al.* Bright single-photon sources in bottom-up tailored nanowires. *Nature Communications* **3**, 737 (2012).
- [60] E. Moreau *et al.* Single-mode solid-state single photon source based on isolated quantum dots in pillar microcavities. *Applied Physics Letters* **79**, 2865 (2001).
- [61] S. Ates *et al.* Post-selected indistinguishable photons from the resonance fluorescence of a single quantum dot in a microcavity. *Phys. Rev. Lett.* **103**, 167402 (2009).
- [62] Y.-M. He *et al.* On-demand semiconductor single-photon source with near-unity indistinguishability. *Nature nanotechnology* (2013).
- [63] O. Gazzano *et al.* Bright solid-state sources of indistinguishable single photons. *Nature communications* **4**, 1425 (2013).
- [64] S. Tan, D. Walls and M. Collett. Nonlocality of a single photon. *Physical review letters* **66**, 252 (1991).
- [65] D. M. Greenberger, M. A. Horne and A. Zeilinger. Nonlocality of a single photon? *Phys. Rev. Lett.* **75**, 2064 (1995).
- [66] D. Sleiter and W. Brinkman. Using holes in gaas as qubits: An estimate of the rabi frequency in the presence of an external rf field. *Physical Review B* **74**, 153312 (2006).
- [67] B. Hessmo, P. Usachev, H. Heydari and G. Björk. Experimental demonstration of single photon nonlocality. *Physical review letters* **92**, 180401 (2004).

HEAVY AND LIGHT HOLE SPIN PROPERTIES

We present an experimental characterization of the light hole exciton spin properties revealed in the electron-hole exchange interaction, polarization selection rules, diamagnetic response and the g factors. A light hole exciton composed of an electron and a high purity light hole state ($> 95\%$ LH) is novel for quantum dots, where either a heavy hole or a mixed hole ground state is usually present. In our experiment, high quality symmetric GaAs epitaxial quantum dots were studied, in which the hole character can be switched from predominantly heavy to predominantly light. Employing micro-photoluminescence measurements in the external magnetic field (Faraday and Voigt geometry) completely reveals the fine structure of the heavy and light exciton, and experimentally determine the values of the spin-spin coupling constants in the Exchange Hamiltonian.

3.1 Introduction

In most direct bandgap semiconductors, the physics of holes is much richer than that of electrons, because they do not only have a spin $S = 1/2$, but also an angular momentum $L = 1$, giving much more freedom in engineering total spin properties. The projection of the total angular momentum $J = 3/2$ (for simplicity: hole pseudo-spin) defines a subspace of heavy holes (HH $J_z = \pm 3/2$) and light holes (LH $J_z = \pm 1/2$). Due to p -like Bloch function symmetry around each atom in the crystal, holes do not experience contact interaction with the spin of nuclei.^{1,2} Holes hyperfine interaction is thus 10 times weaker than the hyperfine contact interaction of electrons^{3,4}, leading to longer coherence. Further, since an electron has a symmetric s -like Bloch function, it is the p -like hole that directly governs the polarization of excitonic absorption and emission by setting the direction of the optical dipole. Understanding optical selection rules for different hole species is not only crucial for conventional electronic devices but also for the implementation of quantum processing and quantum communication schemes with quantum dots. Optical selection rules for HHs have proven to be ideal for all-optical spin manipulation schemes⁵⁻⁹ and for the implementation of spin-photon entanglement.^{10,11} LHs, on the other hand, have complementary advantages. In contrast to HHs they couple directly to the radiofrequency magnetic field¹², enabling on-chip manipulation. In addition, a given LH spin can recombine with both electron spin states, making coherent spin to photon quantum information transfer possible.¹³

However, only recently a novel type of QDs with almost pure LH ground state ($> 95\%$ LH character) has been developed.¹⁴ Therefore compared to the HH exciton, the LH exciton of high purity is not yet well characterized experimentally (in quantum dots LH-HH mixing has been studied^{15,16}). Here, we aim at filling this gap by presenting measurements of the HH and LH fine structure and magnetic response in Faraday and Voigt geometry. This work gives more insight into the LH and the symmetry of its Bloch function.

In our experiment we investigate the photoluminescence of quantum dots, whose hole character can be switched from dominantly heavy to dominantly light by inducing tensile strain in thin nanomembranes with embedded quantum dots. The details of this technique are described in ref.¹⁴. Fig. 3.1(a) schematically shows our structure with GaAs/AlGaAs strain-free, epitaxial quantum dots. In the as-grown sample, holes in the quantum dot have a dominant HH character. However, when the sacrificial layer of AlAs is etched away, we are left with 200 nm thick membranes, where the quantum dot is sandwiched between two thin layers with In atoms. In a thin membrane, the compressively stressed In-containing layers can partially relax and induce a biaxial tensile strain of 0.36% in the quantum dot and surrounding AlGaAs matrix. A LH exciton in contrast to the HH one, emits also photons polarized in z direction. This is a reason why we collect the photoluminescence from the edge of the sample, as schematically illustrated in fig. 3.1 (b). This geometry allows us to measure z and y polarization components of the exciton spectrum. We apply the magnetic field in two

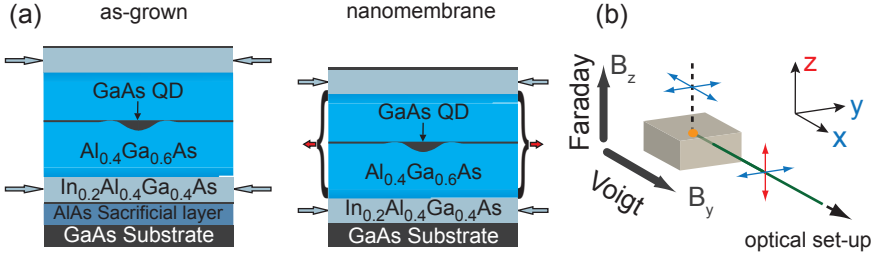


Figure 3.1 | (a) As-grown sample with strain-free quantum dots and tensile strained membranes. (b) Measurement geometry: side photoluminescence collected from the edge of the sample, where y and z polarization components can be measured. Magnetic field in Faraday (Voigt) geometry is aligned with the sample growth axis z (the plane of the sample).

directions: along the sample growth direction z (Faraday geometry) and in the plane of the sample (Voigt geometry).

The polarization of the exciton emission results directly from the orbital symmetry of the hole Bloch function. We express the hole J_z states in the linear combination of the orbital L_z and spin S_z eigenfunctions:^{17,18}

$$\begin{aligned}
 |\uparrow_{HH}\rangle &= \left| +\frac{3}{2} \right\rangle = \left| +1, +\frac{1}{2} \right\rangle, \\
 |\downarrow_{HH}\rangle &= \left| -\frac{3}{2} \right\rangle = \left| -1, -\frac{1}{2} \right\rangle, \\
 |\uparrow_{LH}\rangle &= \left| +\frac{1}{2} \right\rangle = \sqrt{\frac{1}{3}} \left| +1, -\frac{1}{2} \right\rangle + \sqrt{\frac{2}{3}} \left| 0, =\frac{1}{2} \right\rangle, \\
 |\downarrow_{LH}\rangle &= \left| -\frac{1}{2} \right\rangle = \sqrt{\frac{1}{3}} \left| -1, +\frac{1}{2} \right\rangle + \sqrt{\frac{2}{3}} \left| 0, -\frac{1}{2} \right\rangle.
 \end{aligned} \tag{3.1}$$

The states with projection of angular momentum $L_z = +1$ ($L_z = -1$) are given by linear combination of in-plane p_x and p_y orbitals ($|+1\rangle = -1/\sqrt{2}|p_x + ip_y\rangle$ and $|-1\rangle = 1/\sqrt{2}|p_x - ip_y\rangle$), whereas $L_z = 0$ corresponds to the p_z orbital. While the first two states in eq. 3.1, corresponding to the HH states, couple only to in-plane polarized light, the LH states can be polarized in any direction: x , y , and z . Calculating the optical transition dipole moments between the electron and the HH, gives two in-plane circularly polarized bright states ($|+1\rangle_{HH} = |\uparrow_{HH}, \downarrow\rangle$, $|-1\rangle_{HH} = |\downarrow_{HH}, \uparrow\rangle$) and two optically forbidden transitions (dark states $|+2\rangle_{HH} = |\uparrow_{HH}, \uparrow\rangle$ and $|-2\rangle_{HH} =$

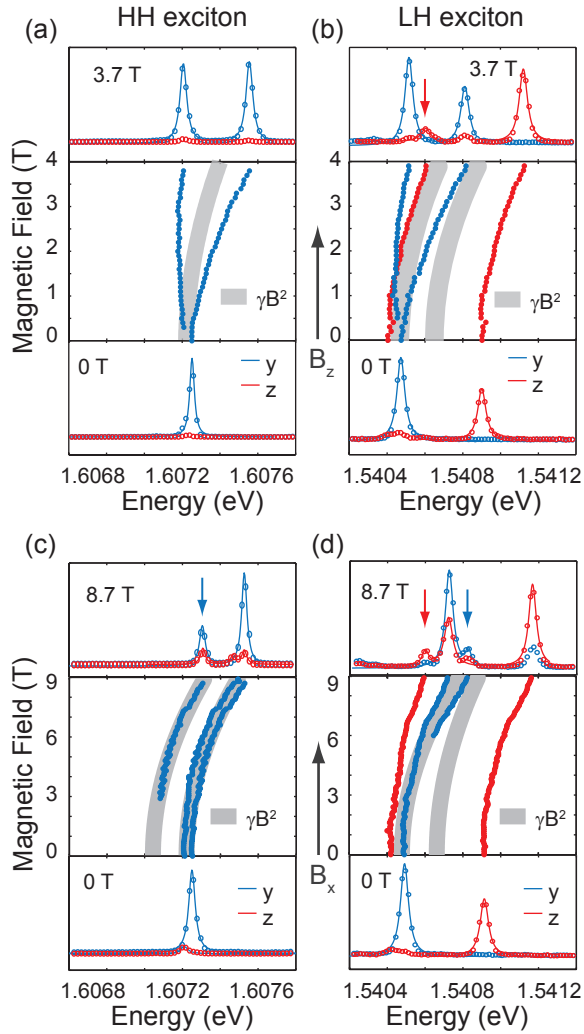


Figure 3.2 | Polarization and energy of photons emitted from (a,c) HH and (b,d) LH exciton in magnetic fields: in (a,b) Faraday and (c,d) Voigt geometry. The z - y polarization resolved spectra are shown for zero and the maximal magnetic field in all geometries. Red and blue datapoints trace the position of each spectral line for increasing magnetic field. The quadratic contribution of the energy shift is shown by the grey shaded area. The red arrows in (b) and (d) point at the LH exciton dark states. A blue arrow in (c) shows one of the HH exciton dark states.

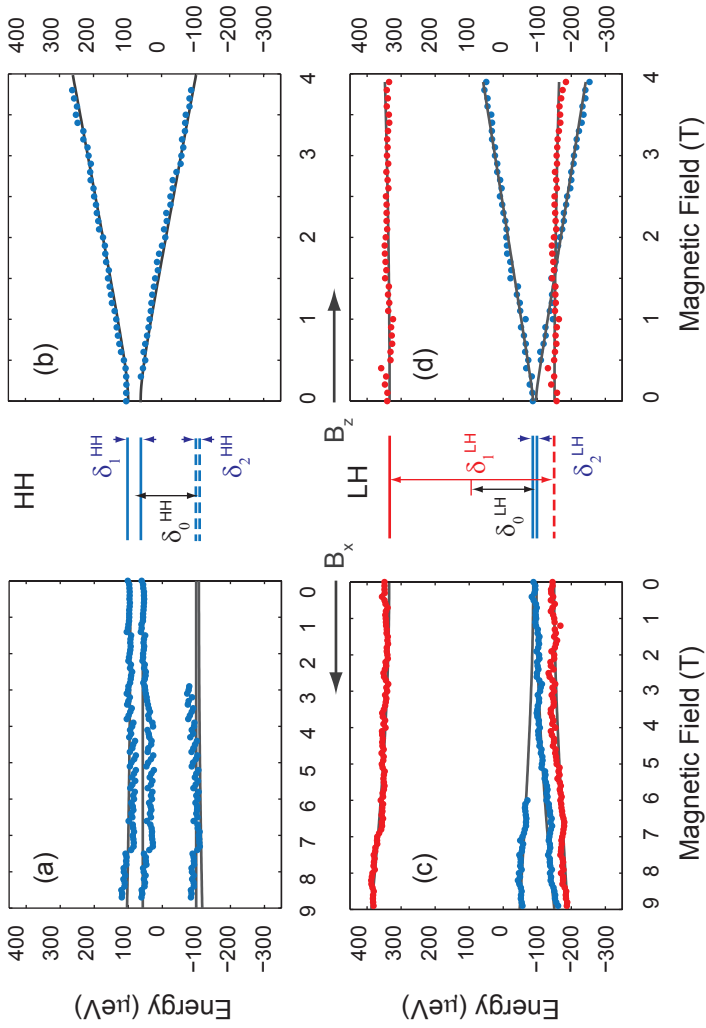


Figure 3.3 | Zeeman shift of HH ((a) and (b)) and LH ((c) and (d)) exciton. The complete set of measurements in Faraday ((a) and (c)) and Voigt ((b) and (d)) geometry reveals the fine structure of the HH and LH exciton. Solid lines represent the fit of the Zeeman Hamiltonians.

$|\downarrow_{HH}, \downarrow\rangle$). In case of a LH exciton, all transitions are optically allowed:

$$|+1\rangle_{LH} = |\uparrow_{LH}, \uparrow\rangle \rightarrow -\frac{\Pi}{\sqrt{6}}(\mathbf{e}_x + i\mathbf{e}_y) \quad (3.2)$$

$$|+0\rangle_{LH} = |\uparrow_{LH}, \downarrow\rangle \rightarrow \frac{2\Pi}{\sqrt{6}}(\mathbf{e}_z) \quad (3.3)$$

$$|-0\rangle_{LH} = |\downarrow_{LH}, \uparrow\rangle \rightarrow \frac{2\Pi}{\sqrt{6}}(\mathbf{e}_z) \quad (3.4)$$

$$|-1\rangle_{LH} = |\downarrow_{LH}, \downarrow\rangle \rightarrow \frac{\Pi}{\sqrt{6}}(\mathbf{e}_x - i\mathbf{e}_y) \quad (3.5)$$

where $\Pi = \langle s|\mathbf{d}|p_x\rangle = \langle s|\mathbf{d}|p_y\rangle = \langle s|d|p_z\rangle$, d is the dipole moment and \mathbf{e}_i are the unit polarization vectors along the $i=x, y, z$ direction.

3.2 Exchange interaction and Zeeman effect Hamiltonians

The electron and hole spins are coupled by the exchange interaction, which establishes the quantum dot exciton eigenstates. The general formula for the exchange interaction^{20?}:

$$H_{exch} = - \sum_{i=x,y,z} (a_i\sigma_i \otimes J_i + b_i\sigma_i \otimes J_i^3) \quad (3.6)$$

The matrix representation of this Hamiltonian is valid for the $h=HH$ subspace spanned by the basis vectors $|+2\rangle_{HH}, |+1\rangle_{HH}, |-1\rangle_{HH}, |-2\rangle_{HH}$ and for the $h=LH$ subspace with basis vectors $|+1\rangle_{LH}, |+0\rangle_{LH}, |-0\rangle_{LH}, |-1\rangle_{LH}$ (see eq. 3.2 - 3.5):

$$H_{exch}^h \frac{1}{2} \begin{bmatrix} -\delta_0^h & 0 & 0 & +\delta_2^h \\ 0 & +\delta_0^h & +\delta_1^h & 0 \\ 0 & +\delta_1^h & +\delta_0^h & 0 \\ +\delta_2^h & 0 & 0 & -\delta_0^h \end{bmatrix} \quad (3.7)$$

Only the formulas for the exchange energies δ_i^h ($i = 0, 1, 2$), expressed in terms of the spin-spin coupling constants a_j and b_j ($j = x, y, z$), are different for the HH and LH exciton (table 3.1). Spectra of HH and LH exciton at zero magnetic field in fig. 3.2(a) and (b)) show the exciton polarization eigenstates. As known for the HH exciton, there are two in-plane linearly polarized bright states resulting from a linear combination of circularly polarized states $|+1\rangle_{HH}$ and $|-1\rangle_{HH}$ ²¹. However, in fig. 3.2 (a), we observe only one of the linearly polarized states in y . In case of the LH exciton, the off-diagonal terms in the Exchange Hamiltonian are responsible for coupling states $|+1\rangle_{LH}$ with $|-1\rangle_{LH}$ and states $|+0\rangle_{LH}$ with $|-0\rangle_{LH}$. The resulting eigenstates of

the exchange Hamiltonian are:

$$|B_x\rangle = 1/2(|+1\rangle_{LH} + |-1\rangle_{LH}) \rightarrow \frac{\Pi}{\sqrt{3}}e_x \quad (3.8)$$

$$|B_y\rangle = 1/2(|+1\rangle_{LH} - |-1\rangle_{LH}) \rightarrow -\frac{i\Pi}{\sqrt{3}}e_y \quad (3.9)$$

$$|B_z\rangle = 1/2(|+0\rangle_{LH} + |-0\rangle_{LH}) \rightarrow \frac{2\Pi}{\sqrt{3}}e_z \quad (3.10)$$

$$|D_z\rangle = 1/2(|+0\rangle_{LH} - |-0\rangle_{LH}) \rightarrow 0 \quad (3.11)$$

In the LH exciton spectrum at zero magnetic field in fig. 3.2 (b) we can recognize the states $|B_y\rangle$ and $|B_z\rangle$ polarized along the y and z directions respectively. The $|B_x\rangle$ would be visible from the orthogonal edge of the sample. Interestingly, the fourth state in eq. 3.11 is dark, even though it is composed of a superposition of two bright states polarized in z . Eventually, the LH exciton has a dark state, however, unlike the HH exciton one, it is not forbidden by the optical selection rules. The $|D_z\rangle$ state is dark, because the amplitude of two composite states $|+0\rangle$ and $|-0\rangle$ perfectly cancels out resulting in zero oscillator strength. Nonetheless, this condition is relaxed in the presence of magnetic field which changes the balance of the states $|+0\rangle$ and $|-0\rangle$. The Zeeman Hamiltonian describes how strongly the electron and hole spin couple to the external magnetic field B :

$$H_e = -\mu_B \sum_{i=x,y,z} (g_{e,i}S_{e,i} - 2\kappa_i J_{h,i} - 2q_i J_{h,i}^3) B_i \quad (3.12)$$

In Faraday geometry (B_z component) we obtain a matrix form for the $h = HH$ and $h = LH$ subspace:

$$H_{Faraday}^h = \frac{\mu_B B_z}{2} \begin{bmatrix} -(g_{e,z} - g_{h,z}) & 0 & 0 & 0 \\ 0 & g_{e,z} + g_{h,z} & 0 & 0 \\ 0 & 0 & -(g_{e,z} + g_{h,z}) & 0 \\ 0 & 0 & 0 & g_{e,z} - g_{h,z} \end{bmatrix} \quad (3.13)$$

It is assumed that the parameter q_z in the Zeeman Hamiltonian (eq. 3.12) is smaller than κ_z ²⁰. Therefore, the LH g factor $g_{LH,z}$ is expected to be approximately 3 times smaller than that of the HH $g_{HH,z}$ (table 3.1).

In fig. 3.2(b) we observe that the initially dark LH exciton state gains oscillator strength. In the spectrum at 3.7 T all four LH exciton states can be recognized (red arrow points at the dark state). The magnetic field Hamiltonian of the Zeeman effect in Faraday geometry has a diagonal form. For large enough magnetic field B in z direction the off-diagonal elements of the exchange Hamiltonian become negligible and we expect the recovery of the HH and LH basis states. Therefore for the HH and LH exciton in fig. 3.2 (a) and (b), at $B_z = 3.7$ T we observe y polarization component of

Table 3.1 | The HH and LH exciton parameters in the exchange and Zeeman Hamiltonians.

Hamiltonian	HH parametes	LH parameters
Exchange	$\delta_0^{HH} = \frac{1}{2}(3a_z + \frac{27}{4}b_z)$	$\delta_0^{LH} = \frac{1}{8}(4a_z + b_z)$
	$\delta_1^{HH} = -\frac{3}{4}(b_x - b_y)$	$\delta_1^{LH} = -(a_x + a_y) - \frac{5}{2}(b_x + b_y)$
	$\delta_2^{HH} = -\frac{3}{4}(b_x + b_y)$	$\delta_2^{LH} = -(a_x - a_y) - \frac{5}{2}(b_x - b_y)$
Zeeman (Faraday)	$g_{HH,z} = 6\kappa_z + \frac{27}{2}q_z$	$g_{LH,z} = 2\kappa_z + \frac{1}{2}q_z$
Zeeman (Voigt)	$g_{HH,x} = 3q_x$	$g_{LH,x} = 4\kappa_x + 10q_x$

two bright circularly polarized states. In addition, the LH exciton shows also the two states polarized in the z -direction. In contrast to Faraday geometry, the Hamiltonian in Voigt geometry does not have diagonal terms, therefore it will only mix further the basis states:

$$H_{Voigt}^h = \frac{\mu_B B_x}{2} \begin{bmatrix} 0 & -g_{e,x} & g_{h,x} & 0 \\ -g_{e,x} & 0 & 0 & g_{h,x} \\ g_{h,x} & 0 & 0 & -g_{e,x} \\ 0 & g_{h,x} & -g_{e,x} & 0 \end{bmatrix} \quad (3.14)$$

However, it couples different pairs of states than the exchange Hamiltonian and as a result each state has a contribution of all basis states (fig 3.2). For the HH exciton this implies that finally the dark excitons can be observed in fig. 3.2(c). For the LH exciton it means that all four exciton states exhibit at the same time x, y and z -polarization and that the optical dipoles have a non isotropic emission in every direction.

In table 3.1 we summarize the expressions for the HH and LH g factors and electron-hole exchange interaction.

3.3 Fine structure and spin-spin coupling constants

The magnetic field changes also the energy of all exciton states, as shown in the plots that bridge the spectra from zero to the maximal value of the magnetic field. Grey lines trace the quadratic shift originating from the diamagnetic effect. By subtracting this quadratic contribution, the effect of the Zeeman interaction or the HH and LH exciton can be extracted in fig. 3.12. From the fits we determine the values of the exchange energies and the g -factors for the HH-like and the LH-like quantum dot (referred as QDA^{HH} and $quQDA^{LH}$). In table 3.2 we summarize the obtained values for three quantum dots with the LH exciton and three dots with the HH exciton. The LH exciton exhibits an exceptionally large δ_1^{LH} splitting between the z -polarized lines (around $470 \mu eV$). We point out, that the fine structures of the LH exciton

Table 3.2 | Experimental values of the exchange energies (in μeV) for three dots with the LH exciton and three dots with the HH exciton. The resulting average spin-spin coupling constants are calculated. Components of the g -factor tensor obtained in Faraday (g_z) and Voigt (g_x) geometry. Note that for the HH exciton in Faraday geometry only the total exciton $g_z^e + g_z^{HH}$ factor is accessible.

	Exchange ($\delta_0, \delta_1, \delta_2$)			g-factors	
				g_z	g_x
QDA^{LH}	183.4,	484.6,	9.5	$g_z^e = 1.03$ $g_z^{LH} = -0.33$	$ g_x^e = 0.17$ $ g_x^{LH} = 0.43$
QDB^{LH}	213.7,	448.3,	3.7	$g_z^e = 1.42$ $g_z^{LH} = 0.09$	
QDC^{LH}	209.2,	466.3,	6.3	$g_z^e = 1.23$ $g_z^{LH} = 0.02$	
QDA^{HH}	168.8,	36.5,	10.3	$g_z^e + g_z^{HH} = 1.56$	$ g_x^e = 0.09,$ $ g_x^{HH} = 0.09$
QDB^{HH}	$\delta_1^{HH} = 12.1$			$g_z^e + g_z^{HH} = 1.49$	
QDC^{HH}	$\delta_1^{HH} = 19.6$			$g_z^e + g_z^{HH} = 0.99$	

$$a_x = -182, a_y = -251, a_z = 441,$$

$$b_x = -22, b_y = 9, b_z = -146.$$

do not differ much from dot to dot (by around 10% for δ_0^{LH} and δ_1^{LH}), even though they are located in different regions of the sample. More measurements in the usual micro-photoluminescence top geometry confirm the uniformity of these quantum dots spectral fingerprints (not shown).

Not all of the quantum dots were measured in Voigt geometry, due to practical inconvenience in our setup. Despite the complete set of exchange energies for the HH exciton could not be obtained without revealing the dark states in Voigt geometry for each dot, we assume that measurement for the QDA^{HH} is representative. We depend on the argument of the uniformity of these quantum dots reported also in Ref. [?] (if the quantum dots are similar after the membrane undercut, they must be similar in the as-grown sample as well). By taking the average values of measured fine structure of the HH and LH exciton, we are able to get approximate values of the complete set of the spin-spin coupling constants in the Exchange Hamiltonian (see the bottom of table 3.2). The values of g factors experience more variations from dot to dot. In

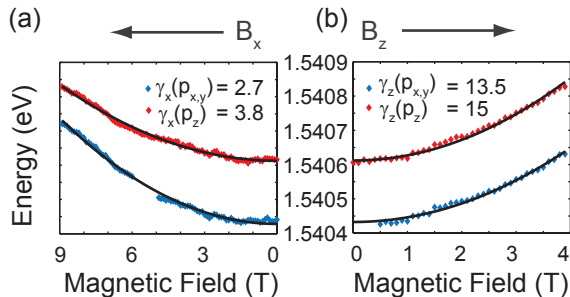


Figure 3.4 | The diamagnetic shift of LH exciton states composed of p_z (red data points) and $p_{x,y}$ (blue data points) orbitals in the (a) Voigt and (b) Faraday geometry.

all cases, the z -component of the LH g -factor g_z^{LH} is smaller than the corresponding electron g -factor and close to zero. The sign of the g_z^{LH} must depend on the details of the confinement experienced by the p_x , p_y and p_z orbitals.

3.4 Diamagnetic shift and the wavefunction symmetry

It is worth to pay a closer attention to the diamagnetic shift. The magnitude of the shift reflects both the spatial extension of the wavefunction, as well as its symmetry. In fig. 3.4 we clearly see that states with a dominant z polarization have a higher diamagnetic coefficient than the states polarized mainly in-plane. This situation is reversed for the other two dots, however, the difference is less pronounced (QDB^{LH} : $\gamma_z(p_z) = 12.4$ and $\gamma_z(p_{x,y}) = 13.6$; QDC^{LH} : $\gamma_z(p_z) = 14.3$ and $\gamma_z(p_{x,y}) = 14.4$). For dot QDA^{LH} , there could be some correlation between the negative LH g -factor g_z^{LH} and the higher diamagnetic shift of the p_z orbital. It would be interesting to simulate the wavefunctions associated with p_z orbitals to understand this behavior better.

3.5 Conclusions

Thanks to the development of a unique growth method of quantum dots with dominantly LH state, we can finally describe the properties of LH spins confined to zero dimensional structures. We have probed the properties of high purity LH and HH spins by measuring the electron-hole Coulomb exchange and interactions with an external magnetic field. The LH spin in contrast to the HH spin can be composed of the p_z orbital which exhibits quite different behavior from p_x and p_y orbitals in quantum dots. We observe a much larger Coulomb exchange interaction and slight difference in the diamagnetic shift. Finally, we can experimentally extract all the spin-spin coupling constants in the exchange Hamiltonian.

3.6 Bibliography

- [1] J. Fischer, W. Coish, D. Bulaev and D. Loss. Spin decoherence of a heavy hole coupled to nuclear spins in a quantum dot. *Physical Review B* **78**, 155329 (2008).
- [2] C. Testelin, F. Bernardot, B. Eble and M. Chamarro. Hole–spin dephasing time associated with hyperfine interaction in quantum dots. *Phys. Rev. B* **79**, 195440 (2009).
- [3] P. Fallahi, S. T. Yılmaz and A. Imamoğlu. Measurement of a heavy-hole hyperfine interaction in ingaas quantum dots using resonance fluorescence. *Phys. Rev. Lett.* **105**, 257402 (2010).
- [4] E. A. Chekhovich, A. B. Krysa, M. S. Skolnick and A. I. Tartakovskii. Direct measurement of the hole-nuclear spin interaction in single InP/GaInP quantum dots using photoluminescence spectroscopy. *Phys. Rev. Lett.* **106**, 027402 (2011).
- [5] A. J. Ramsay *et al.* Fast optical preparation, control, and readout of a single quantum dot spin. *Phys. Rev. Lett.* **100**, 197401 (2008).
- [6] B. D. Gerardot *et al.* Optical pumping of a single hole spin in a quantum dot. *Nature* **451**, 441 (2008).
- [7] D. Brunner *et al.* A coherent single-hole spin in a semiconductor. *Science* **325**, 70 (2009).
- [8] K. De Greve *et al.* Ultrafast coherent control and suppressed nuclear feedback of a single quantum dot hole qubit. *Nature Physics* **7**, 872 (2011).
- [9] T. M. Godden *et al.* Coherent optical control of the spin of a single hole in an InAs/GaAs quantum dot. *Phys. Rev. Lett.* **108**, 017402 (2012).
- [10] W. Gao, P. Fallahi, E. Togan, J. Miguel-Sanchez and A. Imamoglu. Observation of entanglement between a quantum dot spin and a single photon. *Nature* **491**, 426 (2012).
- [11] K. De Greve *et al.* Quantum-dot spin-photon entanglement via frequency down-conversion to telecom wavelength. *Nature* **491**, 421 (2012).
- [12] D. Sleiter and W. Brinkman. Using holes in gaas as qubits: An estimate of the rabi frequency in the presence of an external rf field. *Physical Review B* **74**, 153312 (2006).

- [13] R. Vrijen and E. Yablonovitch. A spin-coherent semiconductor photo-detector for quantum communication. *Physica E: Low-dimensional Systems and Nanostructures* **10**, 569 (2001).
- [14] Y. Huo *et al.* A light-hole exciton in a quantum dot. *Nature Physics* (2013).
- [15] L. Besombes, K. Kheng and D. Martrou. Exciton and biexciton fine structure in single elongated islands grown on a vicinal surface. *Physical review letters* **85**, 425 (2000).
- [16] T. Belhadj *et al.* Impact of heavy hole-light hole coupling on optical selection rules in gaas quantum dots. *Applied Physics Letters* **97**, 051111 (2010).
- [17] J. M. Luttinger. Quantum theory of cyclotron resonance in semiconductors: General theory. *Phys. Rev.* **102**, 1030 (1956).
- [18] S. Hong and J. Singh. Theoretical studies of polarization dependent electro-optical modulation in lattice matched and strained multi-quantum well structures. *Superlattices and Microstructures* **3**, 645 (1987).
- [19] H. W. van Kesteren, E. C. Cosman, W. A. J. A. van der Poel and C. T. Foxon. Fine structure of excitons in type-ii gaas/alas quantum wells. *Phys. Rev. B* **41**, 5283 (1990).
- [20] M. Bayer *et al.* Fine structure of neutral and charged excitons in self-assembled in(ga)as/(al)gaas quantum dots. *Phys. Rev. B* **65**, 195315 (2002).
- [21] B. J. Witek *et al.* Measurement of the g -factor tensor in a quantum dot and disentanglement of exciton spins. *Phys. Rev. B* **84**, 195305 (2011).

CHAPTER 4

MEASUREMENT OF g -FACTOR TENSOR IN A QUANTUM DOT AND DISENTANGLEMENT OF EXCITON SPINS

B.J. Witek, R.W. Heeres, U. Perinetti, E.P.A.M Bakkers, L.P. Kouwenhoven and
V. Zwiller

We perform polarization-resolved magneto-optical measurements on single InAsP quantum dots embedded in an InP nanowire. In order to determine all elements of the electron and hole g -factor tensors, we measure in magnetic field with different orientations. The results of these measurements are in good agreement with a model based on exchange terms and Zeeman interaction. In our experiment, polarization analysis delivers a powerful tool that not only significantly increases the precision of the measurements, but also enables us to probe the exciton spin state evolution in magnetic fields. We propose a disentangling scheme of heavy-hole exciton spins enabling a coherent transfer of a photon in a time-bin superposition onto the electron spin.

Part of this chapter has been published in *Physical Review B* **84**, 195305 (2011).

4.1 Introduction

Carrier spins in semiconductor quantum dots (QDs) have attracted considerable interest due to their potential in quantum information processing based on optical, ultrafast spin manipulation. In recent years, impressive steps toward this goal have been demonstrated: high fidelity spin initialization by optical pumping,¹ coherent population trapping^{2,3} and coherent spin rotation with picosecond optical pulses.⁴ In all these cases electron and hole g -factors play a crucial role in defining the qubit energy levels. In order to optically address only a single spin state and reduce off-resonant coupling to other states, large g -factors are desired. On the other hand, an electron g -factor of zero is preferable for coherent photon to spin conversion⁵⁻⁷.

In bulk semiconductors strong spin-orbit interaction is responsible for relatively large negative electron g -factors⁸ (e.g. in InAs $g_e = -14.7$ versus free electron $g_e \approx 2$). Three dimensional confinement in a quantum dot can result in quenching of the orbital angular momentum and hence lead to the modification of g -factors.^{9,10} The influence of confinement on g -factors has been studied in various experiments.¹⁰⁻¹⁵ However, only some of the electron and hole g -tensor components were probed [e.g. exciton g -factor $g_X = (g_{e,z} + g_{h,z})$] providing an incomplete tensor measurement.

Here, we report the results of photoluminescence (PL) measurements in magnetic fields in three different orientations on two differently charged QDs, that reveal all of the components of the electron and hole g -factor tensors. Our measurements are polarization - resolved and therefore provide information about magnetic field-induced mixing of quantum states, which was not accessible in previous experiments.¹⁶ The nanowire QDs we use are a promising system for g -factor engineering because of the possibility to controllably grow QDs of different sizes and aspect ratios.

4.2 Model

In order to describe neutral and charged excitons in a magnetic field, we will utilize the Hamiltonians discussed in detail in Bayer *et al.*¹⁷ and van Kesteren *et al.*¹⁸ For simplicity only holes that form the top of the valance band, i.e., heavy holes ($J_{h,z} = \pm 3/2$), are considered here. The electron with a spin $S_{e,z} = \pm 1/2$ (\uparrow or \downarrow) and heavy hole with $J_{h,z} = \pm 3/2$ (\uparrow or \downarrow) can form four exciton states of different total exciton spin projections J_z :

$$|+1\rangle = |\downarrow\uparrow\rangle, |-1\rangle = |\uparrow\downarrow\rangle, |+2\rangle = |\uparrow\uparrow\rangle, |-2\rangle = |\downarrow\downarrow\rangle. \quad (4.1)$$

The electron and hole spin couple to the external magnetic field via the Zeeman Hamiltonian. By using these four exciton states as the basis, the Zeeman Hamiltonian for a magnetic field B_z oriented along the QD quantization axes (Faraday configuration)

can be represented by the matrix¹⁷:

$$H_B^z = \frac{\mu_B B_z}{2} \begin{pmatrix} g_{X,+1} & 0 & 0 & 0 \\ 0 & g_{X,-1} & 0 & 0 \\ 0 & 0 & g_{X,+2} & 0 \\ 0 & 0 & 0 & g_{X,-2} \end{pmatrix} \quad (4.2)$$

where $g_{X,\pm 1} = \pm(g_{e,z} + g_{h,z})$ and $g_{X,\pm 2} = \pm(g_{e,z} - g_{h,z})$ are the expressions for bright ($|\pm 1\rangle$) and dark ($|\pm 2\rangle$) exciton g -factors in the z -direction.

The orientation of the magnetic field in the Faraday configuration matches the QD quantization axis (z , growth direction). Therefore the eigenstates of the H_B^z Hamiltonian coincide with the chosen basis (4.1).

In the Voigt configuration the magnetic field is applied in the plane of the QD (for simplicity we consider only the x direction) resulting in breaking of the rotational symmetry about the z -axis. This leads to the H_B^x Hamiltonian¹⁷:

$$H_B^x = \frac{\mu_B B_x}{2} \begin{pmatrix} 0 & 0 & -g_{e,x} & g_{h,x} \\ 0 & 0 & g_{h,x} & -g_{e,x} \\ -g_{e,x} & g_{h,x} & 0 & 0 \\ g_{h,x} & -g_{e,x} & 0 & 0 \end{pmatrix} \quad (4.3)$$

The off-diagonal terms account for mixing between bright and dark states. In the Voigt configuration (B_x) the resulting eigenvectors are linear superpositions of basis vectors:

$$\begin{aligned} |X_{90^\circ}^*(I)\rangle &= 1/2(|+1\rangle + |-1\rangle + |+2\rangle + |-2\rangle) \\ |X_{90^\circ}^*(II)\rangle &= 1/2(|+1\rangle - |-1\rangle + |+2\rangle - |-2\rangle) \\ |X_{90^\circ}^*(III)\rangle &= 1/2(|+1\rangle - |-1\rangle - |+2\rangle + |-2\rangle) \\ |X_{90^\circ}^*(IV)\rangle &= 1/2(|+1\rangle + |-1\rangle - |+2\rangle - |-2\rangle) \end{aligned} \quad (4.4)$$

The labels I to IV indicate the eigenstates ordered by increasing energy.

Electron and hole spins do not only interact with an external magnetic field, but also with each other. Exchange interaction couples electron and hole spins in QDs and splits the energy of electron-hole pairs with different spin configurations. The Hamiltonian for the exchange interaction can be written as^{17,18}:

$$H_{exchange} = \frac{1}{2} \begin{pmatrix} +\delta_0 & +\delta_1 & 0 & 0 \\ +\delta_1 & +\delta_0 & 0 & 0 \\ 0 & 0 & -\delta_0 & +\delta_2 \\ 0 & 0 & +\delta_2 & -\delta_0 \end{pmatrix} \quad (4.5)$$

where δ_0 is the splitting between bright and dark states, δ_1 is often referred in literature as the fine structure splitting (FSS) of a bright exciton and δ_2 is the equivalent splitting

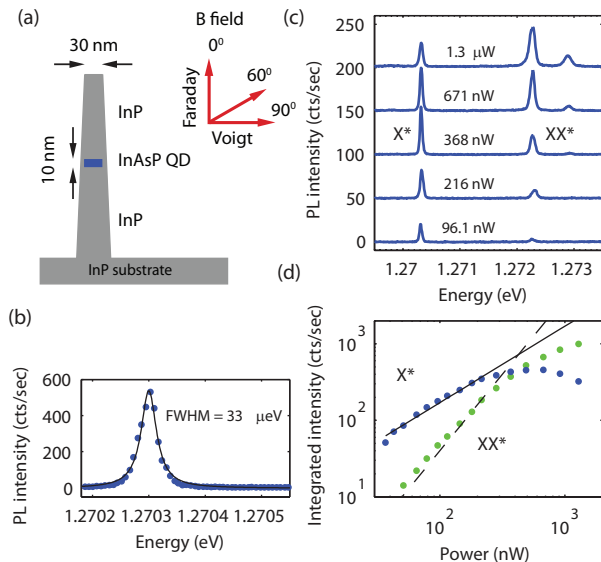


Figure 4.1 |Structural and optical properties of nanowire quantum dots. (a) Schematic nanowire and magnetic field orientations. (b) PL spectrum of a single exciton recombination. (c) Power dependent spectra taken at 10 K under nonresonant (532 nm) excitation at $B = 0$. The two emission peaks are identified as a charged exciton (X^*) and charged biexciton (XX^*). (d) Integrated intensity of X^* and XX^* transitions versus excitation power. The solid (dashed) line is a guide to the eye for linear (quadratic) power dependence.

for a dark exciton. Note that the exchange interaction is present for a single electron and hole pair (neutral exciton), and vanishes for more complex exciton molecules that consist of two electrons (total $S_{e,z} = 0$) and/or two holes (total $J_{h,z} = 0$). This is the case for a biexciton and singly charged excitons.

4.3 Experiment

We studied single $\text{InAs}_{0.25}\text{P}_{0.75}$ wurtzite quantum dots (QDs) embedded in InP wurtzite nanowires grown in the [111] direction. We performed photoluminescence (PL) measurements with a continuous wave 532 nm excitation laser. The polarization of the QD emission was fully characterized by the tomography measurements using two liquid crystal variable retarders. Our cryostat ($T \approx 10$ K) with a vector magnet allowed us to vary the direction of the magnetic field in the $x - z$ plane, with z being both the optical axis and the nanowire growth direction. Three magnetic field configurations: Faraday, Voigt and 60° , that are of a particular interest in our

experiment, are given in Fig. 5.1(a) together with a schematic of a nanowire. A typical QD, with a diameter of 30 nm and height of 10 nm, is surrounded by a thin shell of InP. Emission linewidths as narrow as $33 \mu\text{eV}$ [Fig. 5.1(b)] are clear signatures of the excellent quality of our QDs, which have also demonstrated spin memory in previous studies¹⁹. Power dependent PL spectra presented here [Fig. 5.1(c)] belong to a singly charged dot for which the g-factors will be determined in Sec. (4.3.1). The PL intensities of the two observed transitions show a linear and a quadratic dependence on excitation power [Fig. 5.1(d)] which is consistent with an exciton and biexciton type of recombination.

4.3.1 Charged Exciton

We start our discussion with a charged exciton X^* in a magnetic field, since its description is simpler than the neutral exciton case. As mentioned earlier, there is no exchange interaction for X^* and therefore the Zeeman Hamiltonian alone will provide a sufficient model. Although in our experiment we have no means of distinguishing between the positively and negatively charged exciton, the description for both cases is the same. Figure 4.2 presents the X^* behavior in three different magnetic field configurations (Faraday, Voigt and 60°).

The charged exciton PL spectra in the Faraday configuration are given in Fig. 4.2(a). Two exciton states of circular polarization σ^+ and σ^- corresponding to the $|+1\rangle$ and $|-1\rangle$ bright states are observed. The peak positions shift with magnetic field due to both Zeeman and diamagnetic effects. After subtracting the quadratic contribution from the diamagnetic shift the exciton state energy versus magnetic field is plotted in Fig. 4.2(b). The experimental data is fitted with the eigenvalues of the relevant Hamiltonian, in this case H_B^z (4.2), using $g_{X,+1} = g_{e,z} + g_{h,z}$ as the free fitting parameter. Since the two remaining exciton states - dark excitons $X_{0^\circ}^*(II)$ and $X_{0^\circ}^*(III)$ - are not visible in the Faraday configuration, $g_{X,+2} = g_{e,z} - g_{h,z}$ cannot be extracted from this measurement.

The situation changes in the Voigt configuration due to mixing between states. All four exciton states are present in the PL spectra as evident in Fig. 4.2(c). The transitions are linearly polarized: horizontally $|H\rangle = 1/\sqrt{2}(|-1\rangle + |+1\rangle)$ and vertically $|V\rangle = i/\sqrt{2}(|-1\rangle - |+1\rangle)$. Interestingly, all four exciton states [$X_{90^\circ}^*(I)$, $X_{90^\circ}^*(II)$, $X_{90^\circ}^*(III)$, and $X_{90^\circ}^*(IV)$] have equal measured intensities implying that they must all be equally composed of bright and dark components. These empirical observations are indeed confirmed by analysis of the H_B^z eigenvectors from (4.4). We find an agreement not only with the fitted energies (Fig. 4.2(d)), but also between observed and predicted brightness and polarization.

From the Faraday and Voigt configurations only in-plane electron $g_{e,x}$ and hole $g_{h,x}$ g-factors can be extracted, but the separate values of $g_{e,z}$ and $g_{h,z}$ remain unknown. This missing information is provided by measurements at an intermediate angle

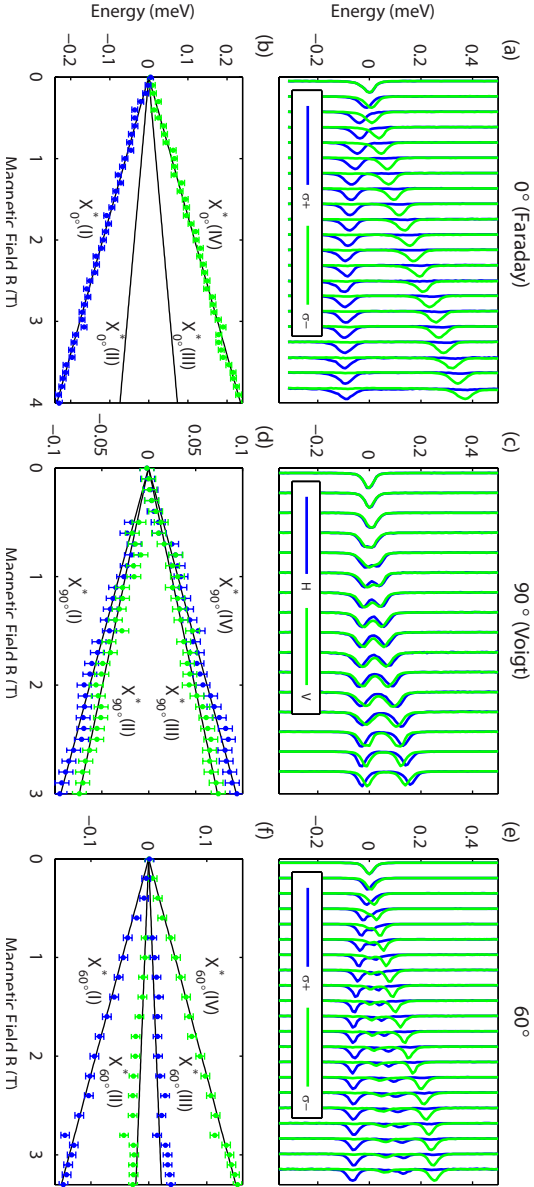


Figure 4.2 | Photoluminescence of a charged exciton (X^*) in a magnetic field in three different configurations (Faraday, Voigt, 60°). (a, c, e) Polarization resolved spectra. (b, d, f) Energies of the exciton transitions after diamagnetic shift subtraction (data points) fitted with the Zeeman Hamiltonian (lines) for the corresponding magnetic field configuration. The X^* recombination energy at zero magnetic field (1.2703 eV) is subtracted. The energy error bar value is $7.4 \mu\text{eV}$.

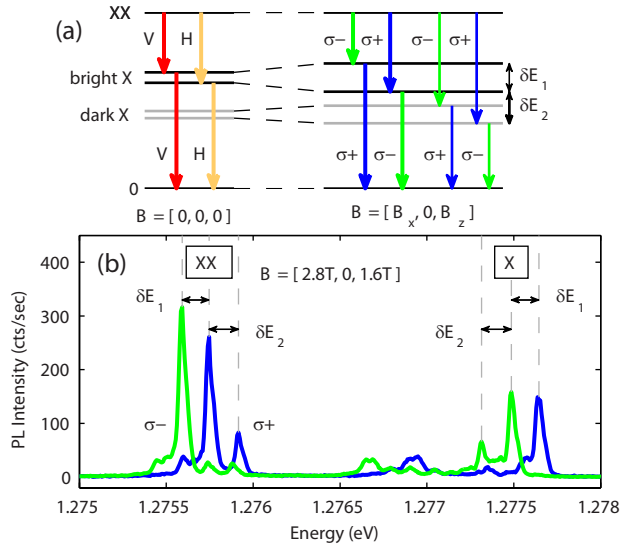


Figure 4.3 (a) Schematic of the neutral exciton and biexciton energy levels in a magnetic field at 60° and (b) corresponding spectrum for $B_{60^\circ} = 3.2$ T ($\mathbf{B} = [2.8$ T, 0, 1.6 T]).

(60°), where some of the features from the Faraday configuration and from the Voigt configuration are combined. Similarly to the Voigt configuration, all four exciton states are observed in the PL spectra, as shown in Fig. 4.2(e). Nevertheless, the PL intensity of exciton states $X_{60^\circ}^*(II)$ and $X_{60^\circ}^*(III)$ is on average three times weaker than the PL intensity of states $X_{60^\circ}^*(I)$ and $X_{60^\circ}^*(IV)$. The transitions are circularly polarized, just like in the case of the Faraday configuration. The fit from Fig. 4.2(f) completes the set of g-factors that is summarized in Table 4.1. Moreover, from the same fit we obtain the expected degree of mixing between dark and bright states. States $X_{60^\circ}^*(II)$ and $X_{60^\circ}^*(III)$, which were completely dark in the Faraday configuration, now consist of 26% bright components ($|-1\rangle$ and $|+1\rangle$ respectively). This gain in brightness comes at the expense of states $X_{60^\circ}^*(I)$ and $X_{60^\circ}^*(IV)$ whose brightness drops to 74% (compared to 100% in the Faraday configuration). These predictions match very well with our experimental observations.

4.3.2 Neutral Exciton

In the analysis of the neutral exciton X^0 in a magnetic field one has to take into account not only the Zeeman Hamiltonian [(4.2) and (4.3)], but also the exchange interaction Hamiltonian (4.5). Although the exchange energies are much smaller

than 1 meV and might seem to give only a small correction, the actual effect on the polarization of the eigenstates will prove to be tremendous.

Figure 4.3(a) presents the schematic of the neutral exciton and biexciton levels in a magnetic field at an intermediate angle (both x and z field components). The biexciton, with a total spin $S_{e,z} = 0$ and $J_{h,z} = 0$, experiences no Zeeman effect and no exchange interaction and therefore its recombination energies perfectly mirror those of the exciton transitions. Thus, one can identify the same splittings, for instance δE_1 and δE_2 in Fig. 4.3(a), in both the biexciton and the exciton emission. We will take advantage of this simple fact and use the biexciton emission to increase the precision of our measurement [especially Fig. 4.4(e)]. Figure 4.3 (b) presents the spectrum of a neutral dot in a magnetic field at 60° , where indeed, δE_1 and δE_2 have the same magnitude for the exciton and the biexciton.

Figure 4.4 shows the results of measurements on a neutral QD in the same magnetic field configurations as previously discussed for the charged QD. We begin with the Faraday configuration. Two states $X_{0^\circ}^0(III)$ and $X_{0^\circ}^0(IV)$ are visible and their energies (data points) are given in Fig. 4.4(a). The sum of the exchange and Zeeman Hamiltonians $H_{exchange} + H_B^z$ is diagonalized in order to extract the four energy eigenvalues that fit our data (lines). Simultaneously, we also obtain the eigenvectors corresponding to the four exciton states. Each eigenvector, representing one state, can be projected onto the total exciton spin J_z basis from (4.1). All the considered J_z components are listed in the legend. Fig. 4.4(b) consists of four plots, each describing the J_z components of a given exciton state. Only states $X_{0^\circ}^0(III)$ and $X_{0^\circ}^0(IV)$ are bright and hence measurable. At zero magnetic field they both consist equally of $|+1\rangle$ and $|-1\rangle$ resulting in linearly polarized neutral exciton transitions. With increasing magnetic field the transitions evolve toward pure σ^+ ($J_z = |+1\rangle$) and pure σ^- ($J_z = |-1\rangle$) polarization. The degree of circular polarization was measured for exciton states $X_{0^\circ}^0(III)$ and $X_{0^\circ}^0(IV)$ and plotted as gray diamonds. The agreement with the predicted curve is very good.

In the Voigt configuration, mixing between dark and bright states becomes sufficiently strong around $B_x = 2$ T to reveal all four exciton states, whose energies are plotted in Fig. 4.4(c). In contrast to the charged exciton case (Fig. 4.2(d)), all the exciton states are already split at $B = 0$ by the exchange energies (δ_0 , δ_1 and δ_2). The solid lines give the fitted eigenvalues of the $H_{exchange} + H_B^x$ Hamiltonian. As apparent in Fig. 4.4(d), states $X_{90^\circ}^0(I)$ and $X_{90^\circ}^0(II)$ start as completely dark at zero magnetic field. With increasing magnetic field they acquire bright components: $|H\rangle$ and $|V\rangle$ respectively, and hence become detectable in PL. This gain in brightness (up to 20 % at $B_x = 4$ T) comes at the expense of $X_{90^\circ}^0(III)$ and $X_{90^\circ}^0(IV)$ states. These initially purely bright states mix with dark components $|+2\rangle$ and $|-2\rangle$, decreasing the contribution of $|H\rangle$ and $|V\rangle$ to only 80% at $B_x = 4$ T. Based on the results given by our model, we draw the conclusion, that state $X_{90^\circ}^0(I)$ couples to $X_{90^\circ}^0(III)$ and state $X_{90^\circ}^0(II)$ couples to $X_{90^\circ}^0(IV)$. The coupled states share the

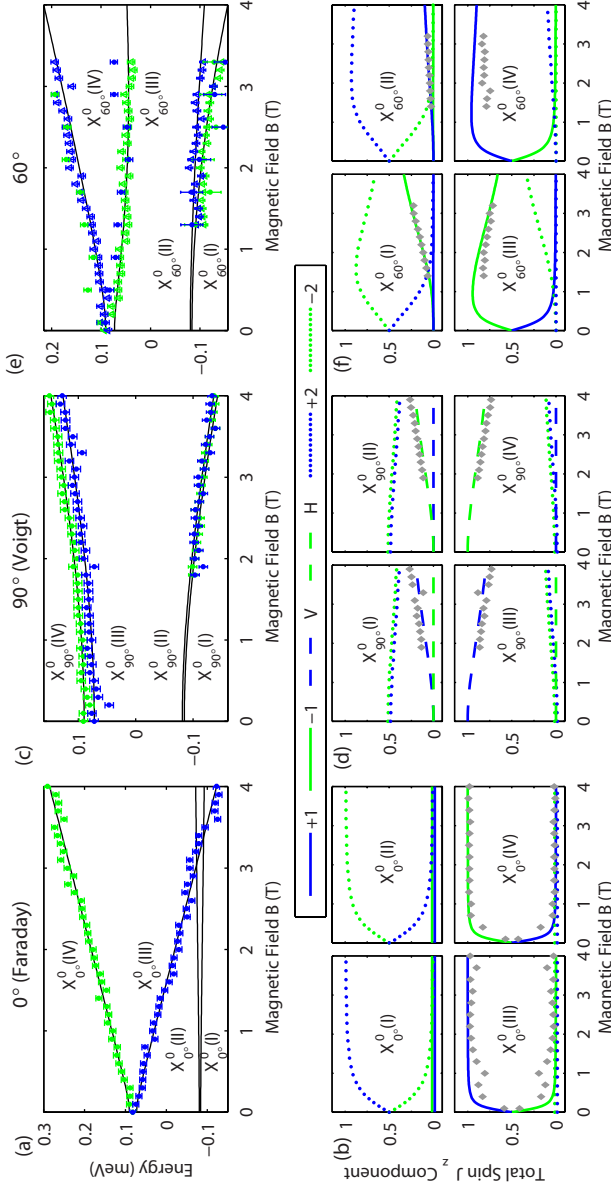


Figure 4.4 | Photoluminescence of a neutral exciton (X^0) in a magnetic field in three different configurations (Faraday, Voigt, 60°). (a), (c), (e) Energies of the exciton transitions after diamagnetic shift subtraction (data points) fitted with the Zeeman Hamiltonian (lines) for the corresponding magnetic field configuration. The average of the bright and dark exciton recombination energy at zero magnetic field 1.2775 eV is subtracted. The energy error bar value is 7.4 μeV . (b, d, f) Projection of the four exciton states eigenvectors onto the $|+1\rangle$, $|-1\rangle$, $|+2\rangle$, $|-2\rangle$ basis, as well as their linear combination $|H\rangle$ and $|V\rangle$.

same symmetry, the first pair form an antisymmetric superposition of spins (at $B = 0$ $|X_{90^\circ}^0(I)\rangle = 1/\sqrt{2}(|\uparrow\uparrow\rangle - |\downarrow\downarrow\rangle)$ and $|X_{90^\circ}^0(III)\rangle = 1/\sqrt{2}(|\downarrow\uparrow\rangle - |\uparrow\downarrow\rangle)$), whereas the second pair of coupled states is a symmetric superposition of spins. The magnetic field B_x is responsible for the precession of the carrier spins around the x -axis and therefore couples the states of the same symmetry.

The total brightness of a pair of coupled states can be defined as the sum of their bright components. This brightness per pair is conserved, for instance: $|\langle V|X_{90^\circ}^0(I)\rangle|^2 + |\langle V|X_{90^\circ}^0(III)\rangle|^2 = 1$ and $|\langle H|X_{90^\circ}^0(II)\rangle|^2 + |\langle H|X_{90^\circ}^0(IV)\rangle|^2 = 1$. Using the above expressions as normalization factors, the contribution of the $|V\rangle$ component to the states $X_{90^\circ}^0(I)$ and $X_{90^\circ}^0(III)$ (and the $|H\rangle$ component to the states $X_{90^\circ}^0(II)$ and $X_{90^\circ}^0(IV)$) can be determined from the experiment. The data points (gray diamonds) obtained in this way again follow our predictions with good accuracy.

In the case of the intermediate angle (60°) in Fig. 4.4(e), the biexciton recombination energies (mirrored about 0) are represented by triangles, whereas the exciton data are shown by circles. The evolution of the initially bright states, $X_{60^\circ}^0(III)$ and $X_{60^\circ}^0(IV)$, is equally well reflected by both sets of data points, which confirms the equivalence of X^0 and XX^0 in our experiment.

We focus now on the analysis of J_z components of the exciton states measured in the 60° configuration. First of all, a striking asymmetry in the exciton states total spin J_z composition is immediately recognized in Fig.4.4(f). Unlike in the Voigt configuration (Fig. 4.4(d)), states $X_{60^\circ}^0(I)$ and $X_{60^\circ}^0(II)$ reach a very different contribution of bright components. At $B_{60^\circ} = 4$ T it is 34% of $|+1\rangle$ for state $X_{60^\circ}^0(I)$ and only 10% of $|-1\rangle$ for state $X_{60^\circ}^0(II)$. Consequently, bright components of states $X_{60^\circ}^0(III)$ and $X_{60^\circ}^0(IV)$ evolve unevenly; they drop from 100% at $B_{60^\circ} = 0$ to 66% and 90% respectively at $B_{60^\circ} = 4$ T. Following the same procedure as described for the Voigt configuration, we add experimental data points (grey diamonds). There is a good correspondence between the predicted asymmetry and our measurement.

There is a simple explanation for this phenomenon. The energy separation between the exciton states sets the strength of the coupling. The gap between states $X_{60^\circ}^0(II)$ and $X_{60^\circ}^0(IV)$ [Fig. 4.4(e)] is significantly bigger than for the other pair of states ($X_{60^\circ}^0(I)$ and $X_{60^\circ}^0(III)$). This results in a much weaker coupling, which is the main reason for the practical difficulties in detecting the extremely weak PL emission from the $X_{60^\circ}^0(II)$ state. The same arguments should also be applied to the Voigt configuration [Fig. 4.4(c)]. In this case, however, the splittings between the coupled pairs of states are similar and the asymmetry becomes a negligible effect.

4.4 Discussion

The complete set of g -factors, exchange energies and diamagnetic coefficients obtained from the fits for charged and neutral excitons is summarized in Table 4.1. The g -factor

Table 4.1 | Values of g -factors and exchange energies for both neutral and charged excitons.

g -factor	Neutral Exciton X^0	Charged Exciton X^*
$g_{e,z}$	-0.84 ± 0.02	-0.70 ± 0.02
$g_{h,z}$	-0.92 ± 0.03	-1.33 ± 0.04
$ g_{e,x} $	0.96 ± 0.02	1.00 ± 0.02
$ g_{h,x} $	0.04 ± 0.02	0.12 ± 0.01
exchange		
δ_0	$163.7 \pm 2.2 \mu eV$	-
δ_1	$17.7 \pm 2.0 \mu eV$	-
δ_2	$3.5 \pm 2.9 \mu eV$	-
diamagnetic coefficient		
γ_{0°	$11.4 \pm 1.9 \mu eV/T^2$	$9.7 \pm 0.7 \mu eV/T^2$
γ_{60°	$9.5 \pm 1.7 \mu eV/T^2$	$8.2 \pm 1.0 \mu eV/T^2$
γ_{90°	$7.3 \pm 1.9 \mu eV/T^2$	$7.4 \pm 1.0 \mu eV/T^2$

components and exchange terms δ_0 , δ_1 are determined with high precision. The magnitude of the FSS (δ_1) is confirmed by an additional measurement performed at zero magnetic field as a function of the PL polarization angle ($\delta_1 = 16.1 \pm 2.6 \mu eV$). The diamagnetic coefficients γ_{0° and γ_{90° confirm a stronger confinement along the z -direction.

In principle our nanowire QD should exhibit C_{3v} symmetry.²⁰ However, several factors might lower this. First of all the bottom interface of the QD is sharper than the top one. Second, the randomness of alloying could further reduce the symmetry. In our case, the Hamiltonians [Eq. (4.2), (4.3), (4.5)] that are attributed to a symmetry lower than D_{2d} or even no symmetry at all¹⁷ reproduce the experimental results very well.

Performing this type of g -factor mapping experiment,¹⁶ we obtain the polarization resolved spectra and therefore access to the sign of electron and hole g -factors along the z direction. Strong confinement responsible for orbital angular momentum quenching¹⁰ pushes the exciton g -factor to positive values, as reported for a similar InAs/InP self-assembled QDs system^{13,14} (g_X as high as 1.25). In our case, however, the exciton g -factor is found to be negative ($g_X = g_{e,z} + g_{h,z}$ is -1.76 and -2.03), implying a weaker confinement. Indeed, the average height of the NW QD is larger than for self-assembled QDs. In case of the in-plane g -factors it is not possible to tell if they are positive or negative, since the polarization of exciton states in the Voigt configuration is insensitive to their sign.

The in-plane hole g -factor $g_{h,x}$ is almost zero, which resembles the situation in quantum wells^{21,22}. In theory the heavy hole in-plane g -factor is almost negligible and

mostly determined by a Luttinger q parameter²¹, $g_{hh,x} \approx 3q$, whereas the light hole g -factor takes larger nonzero values²³. For bulk InAs and InP, Luttinger parameters are 0.04 and 0.02 respectively²⁴ leading to an estimated $g_{hh,x} \approx 0.09$. The experimental result for nanowire QDs deviates slightly from this approximation, which is not surprising taking into account the 3D confinement. The charged exciton in-plane hole g -factor ($g_{h,x} = 0.12 \pm 0.01$) is larger than the neutral one ($g_{h,x} = 0.04 \pm 0.02$), and the same trend was reported for interfacial QDs in GaAs QWs¹⁶. Still this value is not large enough to imply heavy hole - light hole coupling. Although in our analysis we completely neglect light holes, we still obtain a very precise description of the experiment, which confirms the validity of our assumption.

The exciton spin behavior is substantially different for the charged and neutral exciton. As apparent from the charged exciton spectra in Fig. 4.2 the polarization and relative intensity of the transitions is independent of the magnetic field magnitude, implying that the mixing between bright and dark states is constant. Dark states become visible immediately in the nonzero transverse magnetic field, which is crucial in experiments involving a three-level lambda system formed by charged exciton states in the Voigt configuration^{2,3}. On the other hand, for the neutral exciton the strength of bright-dark state mixing increases with magnetic field (Fig. 4.4). The separation δ_0 between the bright and dark states prevents the immediate coupling.

Our studies have demonstrated that the coupling strength between exciton states can be tuned by a careful choice of the magnetic field angle and magnitude. This opens the possibility of engineering any superposition of exciton spin states at will. One particular example is illustrated in Fig. 4.5, where the behavior of a neutral exciton in a magnetic field at 20° is simulated. We took the experimental values of exchange energies and g -factors listed in Table 4.1. Fig. 4.5(a) plots the energies of exciton states in a magnetic field up to 6 T. We observe the anticrossing of states $X_{20^\circ}^0(I)$ and $X_{20^\circ}^0(III)$. At the anticrossing, at approximately $B_{20^\circ} = 3.6$ T, the exciton spin states take a special form. As evident from Fig. 4.5(b) states $X_{20^\circ}^0(I)$ and $X_{20^\circ}^0(III)$ are equally composed of dark $|-2\rangle$ and bright $|-1\rangle$ components. At the same time states $X^0(II)$ and $X^0(IV)$ do not mix and stay completely dark $|+2\rangle$ or completely bright $|+1\rangle$. We can write the corresponding spin states at $B_{20^\circ} = 3.6$ T as follows:

$$\begin{aligned}
 |X_{20^\circ}^0(I)\rangle_{3.6T} &= \frac{1}{\sqrt{2}}(|\downarrow\downarrow\rangle - |\uparrow\downarrow\rangle) = \frac{1}{\sqrt{2}}(|\downarrow\rangle - |\uparrow\rangle) \otimes |\downarrow\rangle \\
 |X_{20^\circ}^0(II)\rangle_{3.6T} &= |\uparrow\uparrow\rangle \\
 |X_{20^\circ}^0(III)\rangle_{3.6T} &= \frac{1}{\sqrt{2}}(|\downarrow\downarrow\rangle + |\uparrow\downarrow\rangle) = \frac{1}{\sqrt{2}}(|\downarrow\rangle + |\uparrow\rangle) \otimes |\downarrow\rangle \\
 |X_{20^\circ}^0(IV)\rangle_{3.6T} &= |\downarrow\uparrow\rangle
 \end{aligned} \tag{4.6}$$

The hole spin $|\downarrow\rangle$ can be factored out from states $X_{20^\circ}^0(I)$ and $X_{20^\circ}^0(III)$ leaving the superposition of electron spin states. Note that this is possible only because of a

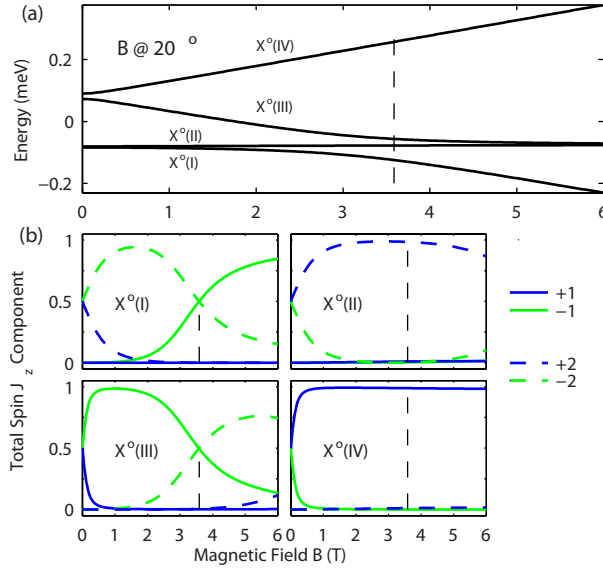


Figure 4.5 |Simulation of neutral exciton states in a magnetic field at 20° . The exchange energies and g -factors are the experimental values. (a) Energy shift due to the Zeeman effect and (b) the projection of the four exciton states eigenvectors onto the $|+1\rangle$, $|-1\rangle$, $|+2\rangle$, $|-2\rangle$ basis.

very small in-plane hole g -factor, which ensures that the hole spin stays insensitive to x -components of the magnetic field. Based on these properties we propose a scheme that enables measuring the electron coherence time T_2 in a similar fashion to the experiment by Kroutvar et al.²⁵ on electron spin relaxation time T_1 . A left handed circularly polarized pump pulse (σ^-) can create a superposition $|\uparrow\downarrow\rangle = 1/\sqrt{2}(|X_{20^\circ}^0(I)\rangle_{3.6T} - |X_{20^\circ}^0(III)\rangle_{3.6T})$ that precesses in time at a frequency given by the difference between the eigenenergies ΔE . This situation is illustrated in Fig. 4.6, where the photocreated state precesses in the equator plane of the Bloch sphere. The most crucial feature in this experiment is that we can factor out and therefore disentangle the hole state and only consider the electron superposition $1/\sqrt{2}(|\uparrow\rangle - e^{i\Delta Et/\hbar}|\downarrow\rangle) \otimes |\downarrow\rangle$. Under the application of external electric field one can remove the disentangled hole from the QD without any harm to the coherence of the electron spin superposition. After a certain delay time a hole can be brought back to the QD. This will result in a photon emission, whose polarization should exhibit quantum beats. The envelope of the beats is set by the electron T_2 . This suggested method will enable the T_2 measurement in time resolved PL. Other techniques of probing T_2^* , such as time resolved Faraday²⁶ and Kerr^{27–29} rotation are based on

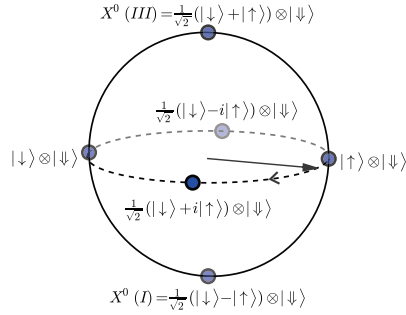


Figure 4.6 | Coherent time evolution of the electron spin disentangled from the heavy-hole spin.

transmission and reflection measurements respectively. In addition, disentangling of electron and hole can be used for mapping the superposition of a photon in two time bins onto the up-down superposition of the electron spin (provided that the precession period is matching the time delay of the two time bins).

4.5 Conclusion

In conclusion, we have presented a set of magneto - optical measurements that leads to the precise determination of g -factor tensor components for the electron and hole. In addition, the possibility of polarization analysis has given us a tool to probe the exciton spin response to the external magnetic field in any configuration. Our model has proven to provide a complete and self-consistent description of all the observed experimental effects in magnetic fields, from the evolution of the energy of exciton states to the prediction of their spin eigenstates. We have proposed a scheme of disentangling heavy-hole exciton spins that opens a way of measuring electron spin coherence T_2 decoupled from a hole.

4.6 Bibliography

- [1] M. Atatüre *et al.* Quantum-Dot Spin-State Preparation with Near-Unity Fidelity. *Science* **312**, 551 (2006).
- [2] X. Xu *et al.* Coherent population trapping of an electron spin in a single negatively charged quantum dot. *Nature Physics* **4**, 692 (2008).
- [3] D. Brunner *et al.* A coherent single-hole spin in a semiconductor. *Science* **325**, 70 (2009).
- [4] D. Press, T. Ladd, B. Zhang and Y. Yamamoto. Complete quantum control of a single quantum dot spin using ultrafast optical pulses. *Nature* **456**, 218 (2008).
- [5] R. Vrijen and E. Yablonovitch. A spin-coherent semiconductor photo-detector for quantum communication* 1. *Physica E: Low-dimensional Systems and Nanostructures* **10**, 569 (2001).
- [6] H. Kosaka *et al.* Spin state tomography of optically injected electrons in a semiconductor. *Nature* **457**, 702 (2009).
- [7] M. Kuwahara, T. Kutsuwa, K. Ono and H. Kosaka. Single charge detection of an electron created by a photon in a g-factor engineered quantum dot. *Applied Physics Letters* **96**, 163107 (2010).
- [8] C. Weisbuch and C. Hermann. Optical detection of conduction-electron spin resonance in *gaas*, *ga1-xinxas*, and *ga1-xalxas*. *Phys. Rev. B* **15**, 816 (1977).
- [9] A. A. Kiselev, E. L. Ivchenko and U. Rössler. Electron g factor in one- and zero-dimensional semiconductor nanostructures. *Phys. Rev. B* **58**, 16353 (1998).
- [10] C. E. Pryor and M. E. Flatté. Landé *g* factors and orbital momentum quenching in semiconductor quantum dots. *Phys. Rev. Lett.* **96**, 026804 (2006).
- [11] N. J. Traynor, R. T. Harley and R. J. Warburton. Zeeman splitting and g factor of heavy-hole excitons in $\text{In}_x\text{Ga}_{1-x}\text{As}/\text{GaAs}$ quantum wells. *Physical Review B* **51**, 7361 (1995).
- [12] M. T. Björk *et al.* Tunable effective *g* factor in *inas* nanowire quantum dots. *Phys. Rev. B* **72**, 201307 (2005).
- [13] D. Kim *et al.* Tuning the exciton *g* factor in single InAs/InP quantum dots. *Physical Review B* **79**, 045310 (2009).
- [14] N. A. J. M. Kleemans *et al.* Size-dependent exciton *g* factor in self-assembled *inas/inp* quantum dots. *Phys. Rev. B* **79**, 045311 (2009).

- [15] F. Klotz *et al.* Observation of an electrically tunable exciton g factor in In-GaAs/GaAs quantum dots. *Applied Physics Letters* **96**, 053113 (2010).
- [16] I. Toft and R. T. Phillips. Hole g factors in GaAs quantum dots from the angular dependence of the spin fine structure. *Phys. Rev. B* **76**, 033301 (2007).
- [17] M. Bayer *et al.* Fine structure of neutral and charged excitons in self-assembled In(Ga)As/(Al)GaAs quantum dots. *Phys. Rev. B* **65**, 195315 (2002).
- [18] H. W. van Kesteren, E. C. Cosman, W. A. J. A. van der Poel and C. T. Foxon. Fine structure of excitons in type-II GaAs/AlAs quantum wells. *Physical Review B* **41**, 5283 (1990).
- [19] M. H. M. van Weert *et al.* Selective Excitation and Detection of Spin States in a Single Nanowire Quantum Dot. *Nano Letters* **9**, 1989 (2009).
- [20] R. Singh and G. Bester. Nanowire quantum dots as an ideal source of entangled photon pairs. *Phys. Rev. Lett.* **103**, 063601 (2009).
- [21] X. Marie *et al.* Hole spin quantum beats in quantum-well structures. *Physical Review B* **60**, 5811 (1999).
- [22] S. Glasberg, H. Shtrikman, I. Bar-Joseph and P. C. Klipstein. Exciton exchange splitting in wide GaAs quantum wells. *Phys. Rev. B* **60**, R16295 (1999).
- [23] A. A. Kiselev, K. W. Kim and E. Yablonovitch. In-plane light-hole g factor in strained cubic heterostructures. *Phys. Rev. B* **64**, 125303 (2001).
- [24] V. Dymnikov and O. Konstantinov. Effective masses and $\hbar^{-1} \partial E / \partial k$ factors of electrons in excited states at the Γ point in III-V semiconductors. *Physics of the Solid State* **51**, 884 (2009). 10.1134/S1063783409050023.
- [25] M. Kroutvar *et al.* Optically programmable electron spin memory using semiconductor quantum dots. *Nature* **432**, 81 (2004).
- [26] J. A. Gupta, R. Knobel, N. Samarth and D. D. Awschalom. Ultrafast Manipulation of Electron Spin Coherence. *Science* **292**, 2458 (2001).
- [27] M. H. Mikkelsen, J. Berezovsky, N. G. Stoltz, L. A. Coldren and D. D. Awschalom. Optically detected coherent spin dynamics of a single electron in a quantum dot. *Nature Physics* **3**, 770 (2007).
- [28] J. Berezovsky, M. H. Mikkelsen, N. G. Stoltz, L. A. Coldren and D. D. Awschalom. Picosecond Coherent Optical Manipulation of a Single Electron Spin in a Quantum Dot. *Science* **320**, 349 (2008).
- [29] H. Kosaka *et al.* Coherent transfer of light polarization to electron spins in a semiconductor. *Phys. Rev. Lett.* **100**, 096602 (2008).

A LIGHT-HOLE EXCITON IN A QUANTUM DOT

Y. H. Huo, B. J. Witek, S. Kumar, J. R. Cardenas, J. X. Zhang, N. Akopian, R. Singh, E. Zallo, R. Grifone, D. Kriegner, R. Trotta, F. Ding, J. Stangl, V. Zwiller, G. Bester, A. Rastelli, and O. G. Schmidt

A light-hole exciton is a quasi-particle formed from a single electron bound to a single light-hole (LH). This type of fundamental excitation, if confined inside a semiconductor quantum dot (QD), could be advantageous in quantum information science and technology. However, it has been neglected so far, because confinement and strain in conventional QDs favor a ground-state single-particle hole with dominant heavy-hole (HH) character. Here we demonstrate the creation of a LH exciton ground state by applying elastic stress to an initially unstrained QD. Its signature is clearly distinct from that of the well-known HH exciton and consists of three orthogonally-polarized bright optical transitions and a fine-structure splitting of hundreds of μeV between in-plane and out-of-plane components. This work paves the way for the exploration of the fundamental properties and of the potential relevance of three-dimensionally confined LH states in quantum technologies.

5.1 Motivation and background

Epitaxial semiconductor quantum dots (QDs) are considered as candidate building blocks for quantum technologies, as they can act both as hosts of static quantum bits (excitons^{1,2}, or spins³⁻⁸) or as triggered sources of single and entangled photons⁹⁻¹¹. In particular, QDs can confine carriers with a spin coherence time longer than in the corresponding bulk materials. Hole spins, especially, are receiving increasing attention, as decoherence due to hyperfine interaction with the nuclear spin bath should be reduced compared to electron spins.⁶⁻⁸ All experimental studies presented so far have been dealing with heavy-holes (HH). This is because quantum confinement lifts the valence band degeneracy and leaves HH states energetically well above the light-hole (LH) states. Further energetic separation is provided by the compressive strain, which is required for the growth of self-assembled QDs such as InGaAs QDs in a GaAs matrix. Some proposals suggest, however, that using LHs instead of HHs would be beneficial for quantum information technologies. These include the coherent conversion of photons into electron-spins¹², the possibility to directly control the LH spin state via microwaves¹³, the direct tomographic measurement of the electron spin state or spin coherence¹⁴, and the faster and more stable control of a magnetic impurity spin coupled to a QD¹⁵. For the realization of these and future proposals, the LH should be the ground state (GS), as any decay channel would reduce the coherence time¹⁶. While QD LH excitons involving an excited hole-state have been studied¹⁷, and LH-HH mixing induced by shape and/or strain anisotropy has been often observed in the GS of conventional II-VI and III-V QDs^{18,19}, reports on systems with LH GS are limited to nanostructures with large height/base ratio²⁰⁻²², resembling vertical nanorods. Due to the broad linewidth of the exciton emission from the "dot-in-dot" studied in Ref²² and the absence of single-nanostructure data for the "columnar QDs" studied in Ref^{20,21}, it remains however unclear whether a "geometrical route" is appropriate to obtain QDs with LH GS and with optical properties comparable to state-of-the-art self-assembled QDs. Here we thus address two open questions: Can we make high-quality QDs with a GS of dominant LH-type? How does the excitonic emission of such a QD look like?

5.2 Sample structure

Our successful answer to the first question is to use strain-engineering rather than a complete redesign of the QD geometry: starting from almost unstrained GaAs QDs in AlGaAs matrix with a conventional HH GS, we reverse the energetic order of the HH and LH bands by biaxial tensile stress. Our QDs are obtained by local droplet etching of nanoholes into an AlGaAs surface followed by GaAs-filling and AlGaAs overgrowth. A sketch of the heterostructure is shown in Fig. 5.1(a). Compared to strained self-assembled QDs, GaAs/AlGaAs QDs grown on GaAs (001) substrates are almost unstrained and their height, which influences the LH-HH splitting, can be

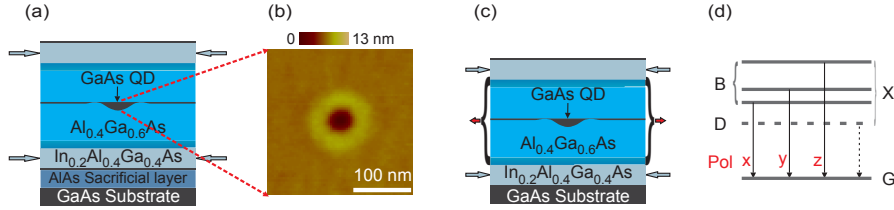


Figure 5.1 | A QD with light-hole exciton ground state. (a) Schematics of the GaAs QD heterostructure grown on GaAs (001) substrate. The GaAs QD layer is in the middle of a pre-stressed (In)AlGaAs membrane. The length of the horizontal arrows is proportional to the magnitude of in-plane strain in the layers. (b) AFM image of a representative droplet-etched nanohole on the AlGaAs surface prior to GaAs filling. (c) Schematics of the GaAs QD heterostructure after selective etching of the AlAs sacrificial layer followed by strain relaxation and bond back. The initially unstrained QD is now tensile strained. (d) Energy level diagram and allowed dipole transitions with corresponding polarization directions. X indicates the neutral light-hole exciton, which consists of a dark (D) state and three bright (B) states decaying to the crystal ground state (G). x and y denote in-plane crystal directions [110] and [1-10] and z denotes the growth direction [001].

controlled by adjusting the amount of GaAs used to fill the nanoholes. Since in-plane anisotropy of the confinement potential is expected to contribute to LH-HH mixing, the growth protocol is further optimized to obtain highly symmetric QDs (see Fig. 5.1(b))²³. Finally, to allow the LH to become the GS, a biaxial tensile strain of about 0.36% is induced on the 8 nm high QDs by embedding them into symmetrically pre-stressed membranes, which are then released from the substrate²⁴ (see arrows in Fig. 5.1(a) and Fig. 5.1(c)). Additional fine-tuning of the biaxial strain is achieved by placing the membranes onto a piezoelectric actuator.^{25,26}

5.3 Light hole exciton states in photoluminescence

In order to experimentally discriminate a LH exciton from a HH exciton, we consider how a LH, with spin projection $J_z = \pm 1/2$ along the [001] crystal direction (z), manifests itself in the polarization state of emitted photons. We constructed basis states for a four-dimensional pure LH exciton space composed of the electron spin (\uparrow and \downarrow) and LH spin (\uparrow and \downarrow):

$$|1\rangle = |\uparrow\uparrow\rangle, |2\rangle = |\downarrow\downarrow\rangle, |3\rangle = |\uparrow\downarrow\rangle, |4\rangle = |\downarrow\uparrow\rangle \quad (5.1)$$

The first two basis states ($|1\rangle$ and $|2\rangle$) with parallel spins have an angular momentum projection of $J_{1,z} = +1$ and $J_{2,z} = -1$, and emit circularly polarized photons (σ^+

and σ^- respectively). The two remaining states ($|3\rangle$ and $|4\rangle$) with antiparallel spins both have $J_{3,z} = J_{4,z} = 0$ giving rise to linearly polarized photons in the z growth direction. However, these are not yet the eigenstates in a QD, where electron-hole exchange interactions should be considered. We thus derived the exchange interaction Hamiltonian from the theory of invariants²⁷ and solved it for a pure LH exciton. By assuming that the momentum matrix elements are isotropic, we find the polarization of the four excitonic eigenstates as shown in Fig. 5.1(d) (see also Ref.²⁸). The exciton (X) consists of three optically bright (B) states and one dark (D) state. Two bright states, B_x and B_y , are linear superpositions of the basis states $|1\rangle$ and $|2\rangle$. The resulting polarization of B_x ($|1\rangle + |2\rangle$) and B_y ($|1\rangle - |2\rangle$) is linear along the $[110]$ (x) and $[1-10]$ (y) crystal directions. The symmetric linear superposition of states $|3\rangle$ and $|4\rangle$ forms another bright state B_z ($|3\rangle + |4\rangle$) polarized along the z direction. Finally, the oscillator strength of the antisymmetric superposition $|3\rangle - |4\rangle$ cancels out and a dark state D_z is formed. This means that, in contrast to the conventional HH exciton configurations, which include two dark states, an additional bright emission line should be observable by collecting the luminescence perpendicular to the growth direction.

To verify whether the induced tensile strain is sufficient to switch the LH to the GS of the valence band of our QDs, we excite μ -photoluminescence (μ -PL) with a laser beam focused on the sample (001) surface and collect linear-polarization-resolved PL spectra of as-grown and tensile strained QDs along both z - and x - (cleaved edge) directions. The spectra for a representative as-grown QD are shown in Fig. 5.2(a),(b) and are fully consistent with a HH exciton: two in-plane polarized bright-exciton states, B_1 and B_2 separated by a fine-structure-splitting (FSS) of $10\mu eV$. (Generally the directions 1 and 2 do not coincide with the crystal directions x and y in highly symmetric QDs²³). After membrane undercut, the average QD-emission-energy redshifts by about 50 meV due to the tensile biaxial strain, as illustrated by the spectra from another representative QD, shown in Fig. 5.1(c),(d). Most importantly all QD spectra measured so far display a new line located at $430\mu eV$ above the in-plane polarized doublet $B_{1,2}$. This line, indicated as B_z in Fig. 5.1(d) is barely visible when observed along the growth direction, but is very pronounced when detected from the cleaved edge of the sample and is linearly polarized along z (Fig. 5.1(d)). In addition, its intensity displays the same excitation-power dependence as $B_{1,2}$ and photon cross-correlation measurements between B_z and $B_{1,2}$ show a lack of coincidence events at zero delay. All these observations are in line with our expectations for a LH exciton having three bright recombination channels: $B_{1,2}$ and B_z . (A relatively weak z -polarized emission observed in Fig.5.2(b), 5.2(d), 5.3(b) in correspondence to $B_{1,2}$ origins from the x -polarized emission of B_1 that due to total internal reflection at the semiconductor-air interface, partially emerges via the edge of the sample). To better resolve the $B_{1,2}$ lines and to access also the dark state D_z of a LH exciton, we carried out magnetic field-dependent μ -PL measurements in Faraday configuration, i.e. with magnetic field parallel to the z direction.^{29,30} In fact, different from the

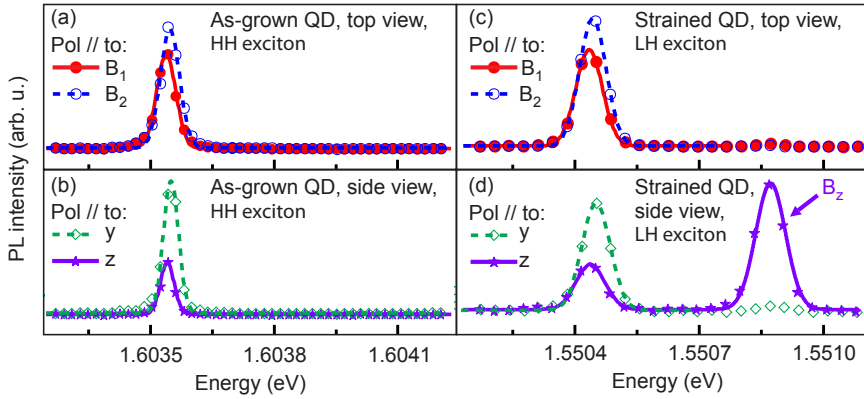


Figure 5.2 | Representative μ -PL spectra of heavy-hole and light-hole excitons in single GaAs/AlGaAs QDs. (a) to (d): Linearly-polarized spectra of neutral excitons along two perpendicular directions for one representative as-grown QD (a,b) and one tensile-strained QD (c,d). Spectra are collected along the conventional z [001] direction in (a,c) and along the x [110] direction from a cleaved edge in (b,d). In (a,c) solid and open circles correspond to the in-plane polarized lines B_1 and B_2 . For the two QDs, the B_1 line has polarization direction close to x . In (b,d) stars correspond to light polarized along the cleaved edge (y [1-10] direction), with spectra dominated by the emission of B_2 , and open diamonds correspond to light polarized along the z [001] growth direction. Besides the projection of the in-plane components (mostly B_1) on the z direction, the spectrum of a light-hole exciton in (d) is dominated by the z -polarized line B_z . In all plots, lines are Lorentzian fits of the experimental data.

HH case in Faraday configuration, the D_z line is expected to become visible due to magnetic-field-induced mixing with the B_z line. This is analogous to the more common situation encountered for the dark states of a HH exciton, which become partially bright when a magnetic field is applied in the x - y plane (Voigt configuration) due to mixing with the x - y polarized bright excitons. (A quantitative description of the behavior of a LH exciton in magnetic field is presented in chapter 3). Fig. 5.3(a) shows polarization-resolved spectra of a single QD collected along the z -direction. The B_1 and B_2 lines, which are initially linearly polarized and split by 9.5 (see bottom of Fig. 5.3(a)), display a diamagnetic shift and split further due to the Zeeman effect. When the Zeeman splitting becomes larger than the exchange splitting, the exchange interaction for states B_1 and B_2 can be neglected and we observe the recovery of the circular polarization of the basis states $|1\rangle$ and $|2\rangle$. The picture changes in Fig. 5.3(b), where light is collected along the x -direction. Besides B_z , the initially dark state D_z appears as a z -polarized line as the field is increased. Analogous to the in-plane polarized lines B_1 and B_2 , the lines B_z and D_z , initially split by the exchange

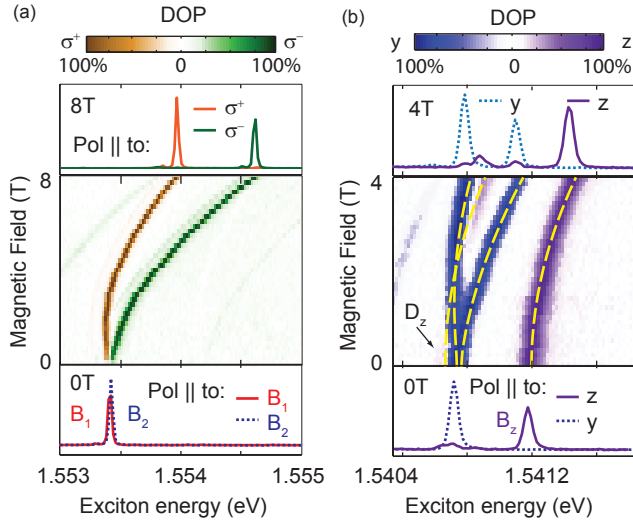


Figure 5.3 | Representative polarization-resolved μ -photoluminescence spectra of light-hole excitons in a magnetic field applied along the growth direction (Faraday configuration). Spectra for light collected along the z direction (a) and along the x direction (b). The colour plots in a,b are obtained by superimposing the intensities of circularly polarized spectra (with σ^+ and σ^- polarization) and linearly polarized spectra (with polarization parallel to the y and z directions), respectively. The polarization-resolved spectra shown on the top and bottom of (a) and (b) correspond to zero and maximum magnetic field. The dashed lines in the colour plot in (b) represent fits of the peak positions for the in-plane polarized B_1 and B_2 lines (white) and z -polarized B_z and D_z lines (green). D_z appears as the magnetic field is increased, as shown in the top spectrum of (b).

interaction, shift and split due to the diamagnetic and Zeeman effect. By fitting the peak energy positions of B_z and D_z , we find that D_z lies $482 \mu\text{eV}$ below the energy of B_z at 0 field. Note that the exchange splitting between B_z and D_z is so large, that it remains dominant over the Zeeman splitting up to the largest magnetic fields available. As a consequence, the basis states $|3\rangle$ and $|4\rangle$ cannot be restored. However, a brightening of D_z is clear and all the four LH exciton states are now observed. Similar behavior and values of the D_z - B_z splitting have been observed for all measured QDs.

5.4 Exchange interaction from the atomistic pseudopotential method

While the experimental results discussed so far are in line with the qualitative expectations of the mesoscopic model, a quantitative prediction of the fine-structure is necessary to assert that the unexpectedly large FSS is indeed a feature of a single LH exciton state. We have thus performed numerical calculations using the atomistic empirical pseudopotential method and configuration interaction, including the electron-hole exchange interaction.^{31,32} The structure for the simulation was constructed from the measured QD morphology by directly using atomic force microscopy (AFM) topographs of representative AlGaAs nanoholes before and after GaAs filling.^{23,33} Due to the lack of compressive strain and the relatively large height (8nm), the splitting between the dominant HH and dominant LH states is significantly reduced, compared to the common InGaAs/GaAs case. To simulate the experimental conditions, we introduce an in-plane tensile strain to the simulation cell and relax the atomic positions as well as the simulation cell in z -direction.³¹ In Fig. 5.4(a) we plot the HH and LH character of the valence band GS, h_0 , which is obtained from the projection of the atomistic quantum dot wavefunctions onto Bloch states of the underlying bulk, as a function of the induced strain. We see that, already for a moderate tensile strain value of 0.2% , the character shifts from dominantly HH to dominantly LH. For the experimentally determined strain value of 0.36% we expect that h_0 has 95% LH character. We further confirm this value by measuring the in-plane polarization anisotropy of the emission and using the model of Tonin et al.³⁴ By assuming the GS to be of dominant LH character, we find that the strained QD, presented in Fig. 5.2(c, d), has a 99% LH character. In Fig. 5.4(b) we plot the excitonic fine structure as a function of the tensile strain. The energies are given relative to the lowest (dark) exciton state D_z . At zero strain we have the well-known situation where the two bright states are polarized in-plane and are split by a FSS of $8\ \mu\text{eV}$, in good agreement with the experimental values, while the dark states are nearly degenerate. When tensile strain is introduced, the situation changes dramatically with one z -polarized bright state between 200 and $600\ \mu\text{eV}$ above the D_z , and two bright states, split by only a few μeV and polarized in-plane, at an energy of around $30\text{-}40\ \mu\text{eV}$ above D_z . These results are in excellent quantitative agreement with the experimental data, demonstrating that the QDs presented here can be used as model systems to study and possibly make use of LH states.

According to the calculation in Fig. 5.4(b), the energy separation ΔE between B_z and the in-plane polarized doublet monotonically increases with increasing tensile strain. To test this prediction, we have transferred pre-stressed membranes onto a piezoelectric substrate (PMN-PT) via gold-thermo-compression bonding (see Ref.³⁵ and inset of Fig. 5.5), allowing us to increase (decrease) the tensile strain by simply decreasing (increasing) the electric field applied across the piezo. (For this experiment, another sample with asymmetric QDs²³ was used. For such QDs, the B_z -line becomes

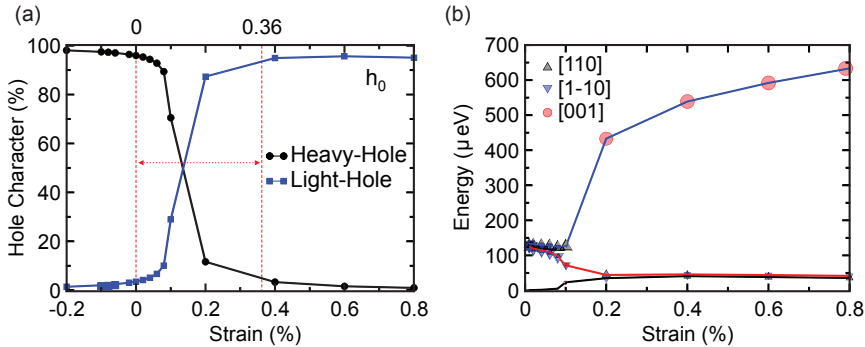


Figure 5.4 | Calculation results using the experimental QD structure. (a) Analysis of the hole character of the ground state h_0 as a function of in-plane biaxial strain. The used GaAs QD has a shape constructed from representative AFM topographs. The dashed lines and horizontal arrow indicate the value of strain before and after membrane undercut. (b) Excitonic fine structure, setting the energy of the lowest exciton state to zero. The black and blue triangles represent the transitions polarized in the growth plane (001) while the red circles represent the transitions polarized along the growth direction [001]. The size of the symbols is proportional to the oscillator strengths. The lowest exciton transition energies are between 1.56 and 1.45 eV for the range of used strains.

easily visible also when observed along the z -direction indicating a radiating dipole which is tilted away from the ideal z -direction. This facilitates the strain-dependent measurements by allowing PL collection along the z direction). As shown in Fig. 5.5, when the electric field changes from 23.3 to -10 kV/cm the exciton energy decreases by about 9 meV and ΔE increases by about 44 μeV (474 to 518 μeV). The calculations predict an increase in ΔE , when going from 0.2% to 0.4% strain, of 105 μeV (388 to 493 μeV) accompanied by a reduction in exciton energy of 31 meV (1.550 to 1.519 eV). Therefore the change in ΔE relative to the change in emission energy is 3.4 $\mu\text{eV}/\text{meV}$ in good agreement with the experimental result of 4.9 $\mu\text{eV}/\text{meV}$.

5.5 Conclusion

In conclusion, we have shown that the excitonic ground-state of self-assembled GaAs QDs can be switched from the common dominant HH to the LH type by releasing prestressed membranes with initially unstrained QDs. The excitonic fine structure was investigated both experimentally and theoretically. The high optical quality of the presented dots (FWHM 23 μeV for as-grown QDs²³, FWHM 37.5 μeV for LH QDs in released membranes), the compatibility of membrane processing with electrical control³⁵, and the fact that the ground hole state can have more than

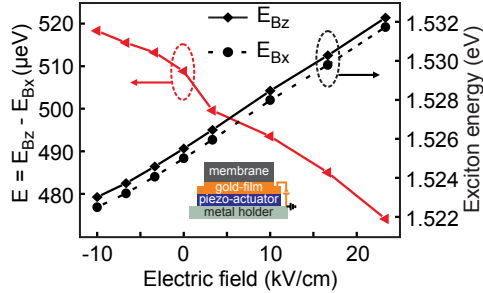


Figure 5.5 |Dynamic strain tuning of a light-hole exciton. Strain-tuning of exciton energy and energy splitting (ΔE) between the B_z line and the low-energy component of the in-plane polarized doublet (here indicated as B_x) measured using an asymmetric QD in a membrane which was released from the GaAs substrate and placed onto a piezoelectric actuator. The inset is a sketch of the experimental configuration.

95% LH character for tensile strains of 0.4%, demonstrate that three-dimensionally confined LH may soon be explored as new semiconductor-based quantum systems for quantum communication technologies.

5.6 Methods

5.6.1 Sample growth, processing and structural characterization

Two samples are discussed in the manuscript (see PL spectra in Fig. 5.2 and Ref³⁶). Sample #1 contains highly symmetric QDs (see AFM image in Fig. 5.1b and Fig. 5.6) and sample #2 asymmetric QDs (see AFM images in Fig. 5.7). Both of the samples were grown by molecular beam epitaxy on semi-insulating GaAs(001) substrates. Eight-nanometre-deep nanoholes were obtained by depositing 0.5 monolayers of excess Al on an $\text{Al}_{0.4}\text{Ga}_{0.6}\text{As}$ (001) surface at a substrate temperature of 600 °C followed by 5 min annealing under As_2 flux. The nanoholes were then overgrown with 2nm GaAs (quantum-dot material), followed by 2 min annealing favouring hole filling, 37nm $\text{Al}_{0.4}\text{Ga}_{0.6}\text{As}$, and 7nm graded $\text{Al}_x\text{Ga}_{1-x}\text{As}$ (with x varying from 0.4 to 0.44). The morphology of the quantum dots was obtained by measuring with AFM the surface of two additional samples, where the growth was interrupted after nanohole etching and after GaAs overgrowth. We can obtain the shape of the resulting QDs by subtracting AFM images of representative nanostructures before and after GaAs filling. Such AFM images are shown in Fig. 5.6 together with corresponding linescans. And they were used to calculate the optical properties of our QDs without adjustable parameters.

The quantum-dot layer was placed into symmetrically pre-stressed membranes, which

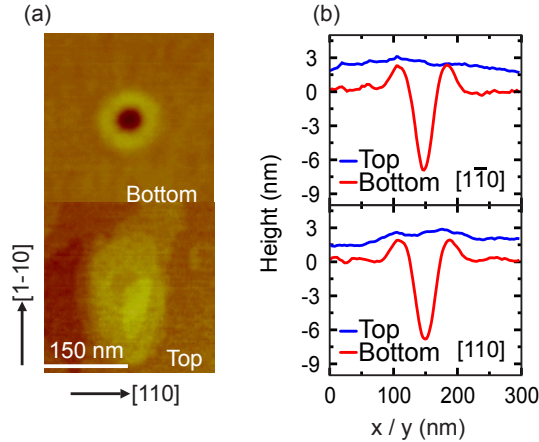


Figure 5.6 [(color online)]. (a) Representative AFM images of the symmetric nanoholes in AlGaAs matrix (Top) and of the surface after 2 nm GaAs-filling (Bottom). (b) Linescans of the AFM images along $[1-10]$ and $[110]$ crystal directions vertically offset by an amount corresponding to the GaAs layers used to form the QDs.

include one $\text{In}_{0.2}\text{Al}_{0.4}\text{Ga}_{0.4}\text{As}$ stressor layer below and another above the active structure. By etching a sacrificial AlAs layer placed below the membrane structure, the strain, which was originally confined in the InAlGaAs layers, is shared with the initially unstrained heterostructure (see horizontal arrows in Fig. 5.1(a,c), with lengths proportional to the strain magnitudes). After etching, the membranes bond-back to the underlying substrate. A tensile strain of 0.36% was induced in the quantum-dot layer according to X-ray diffraction measurements.

5.6.2 Optical characterization

We performed μ -photoluminescence measurements using a 532nm continuous-wave frequency-doubled Nd:YVO4 laser focused onto the sample surface using a microscope objective with a numerical aperture of 0.42. The same objective was used to collect light along the z $[001]$ direction. A second objective was mounted at 90deg to collect light emitted along the x $[110]$ direction. The membranes with underlying substrate were cleaved and mounted on the cold-finger of a cryostat equipped with multiple optical windows. For polarization analysis, we rotated an achromatic $\lambda/2$ waveplate by 360° at 2° steps in front of a linear polarizer. For the magnetic-field-dependent photoluminescence measurements, the samples were mounted on the top and side

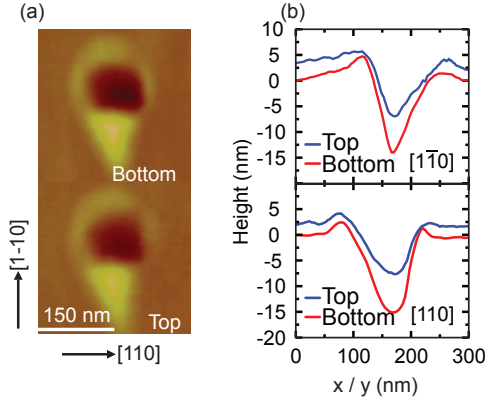


Figure 5.7 (a) Representative AFM images of the nanoholes in GaAs matrix (Top) and of the surface after 2 nm GaAs-filling (Bottom). (b) Linescans of the AFM images along $[1-10]$ and $[110]$ crystal directions.

facets of a cubic sample holder. A vector magnet was employed to measure each sample in the Faraday geometry with magnetic fields up to $B_{max} = 8T$ ($B_{max} = 4T$) along the growth direction for samples on the top (side) facet.

5.7 Supplementary

5.7.1 Fine structure of as-grown QDs and of side view PL spectra

The fine-structure of bright excitons confined in as-grown QDs similar to those in samples used in this experiment have been studied and reported in Refs.²³ and³⁷, respectively. In both cases the fine structure consists of two lines linearly polarized in the growth plane, indicating a dominant HH character. The QDs in #1 are characterized by an average fine structure splitting (FSS) of ~ 4 μeV and a rather random orientation of the two mutually perpendicular, linearly polarized bright exciton lines. In contrast, QDs in Sample #2 are anisotropic, their average FSS is 49 μeV and the polarization direction of the low energy component is mostly aligned along the $[110]$ crystal direction.

When the emission is observed along the x direction (cleaved edge), we expect a *radiating dipole oriented along the y direction* to produce no signal polarized along the z (growth) direction. Similarly, for a dipole oriented along the z direction we expect no light polarized along the y direction. For a *dipole oriented along the x direction*

the situation is slightly more complex. In fact, since the QDs are close to the sample surface, we expect to collect also light which has undergone total internal reflection and light which is emitted from the top surface and is refracted towards the objective. When both in-plane dipoles form a finite angle with respect to the cleaved edge (as it is generally the case for our symmetric dots) they will both contribute to z-polarized light. These arguments, backed by finite-difference-time-domain simulations with the LUMERICAL software, see Fig. S5.8, explain why the side-view polarization-resolved PL spectra (Fig. 2b, 2d, 3b) show some weak z-polarized signal in correspondence to the in-plane polarized dipoles.

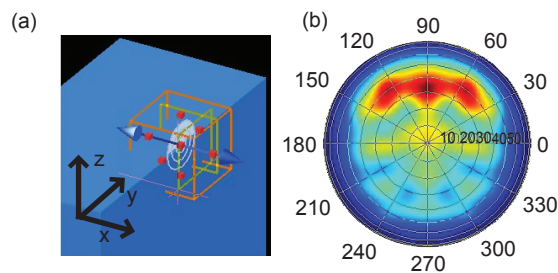


Figure 5.8 |Lumerical simulation of a dipole oriented in the x direction. (a) Schematic of the simulated structure: $20\mu\text{m} \times 10\mu\text{m}$ AlGaAs (refractive index, $n = 3.36$) membrane of 150 nm thickness on GaAs ($n=3.68$). The dipole source is embedded in the membrane 200 nm from the sample edge. (b) Far field projection of z-polarized light component onto a hemisphere in the x direction. Our objective ($\text{NA} = 0.4$) collects light from a cone of a solid angle 23° centered at $(0,0)$. The x-dipole radiates to the top of the sample (in a cone in the z-direction). Therefore light emitted at an angle to the top of the sample will exhibit a z-polarized component (intense red spot on a hemisphere). However, part of the light emitted to the top undergoes a total internal reflection and emerges at the membrane edge (weak horizontal spot). This light is collected with our objective and seen as z-polarized.

5.7.2 Magnetic-field-dependent PL data for as-grown QDs (HH exciton)

The magnetic-field dependent spectra of two representative as-grown QDs in sample #1 are shown in Fig. 5.9. The polarization of the two bright excitons in Fig. 5.9(a) is a typical fingerprint of a HH exciton in the Faraday configuration: two bright states of circular polarization σ^+ and σ^- . The side view (Fig. 5.9(b)) reveals mostly in-plane polarized emission and only weak emission polarized along the z direction, whose origin is discussed in Sec. 3.a. Dark states remain invisible consistent with the highly

symmetric shape of the QDs and no extra line polarized in the z-direction is observed. For QDs from sample #2, the latter observation remains valid, while dark states appear also in Faraday configuration, consistent with the irregular shape of the QDs (not shown here).

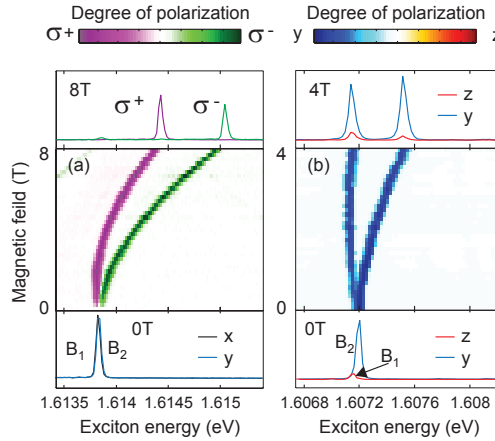


Figure 5.9 |Color-coded magneto-PL spectra of a single heavy-hole exciton in the as-grown sample #1 as a function of magnetic field applied along the growth direction (Faraday configuration). In (a), light is collected along the z-direction and in (b) along the x-direction. The polarization-resolved spectra are shown for zero and maximum magnetic field.

5.7.3 Magnetic-field dependent PL spectroscopy of tensile strained QDs

For 3 QDs we have recorded side view spectra in the magnetic field (in Faraday configuration up to $B = 4$ T). As apparent from Fig. 5.10 all of them exhibit the same, reproducible features: two transitions polarized in-plane and one polarized in the z-direction. The red arrow at $B=4$ T points at a very weak emission from the initially dark state D_z . The QDs differ only by the relative intensity of the in-plane and z-polarized lines. We extrapolated the position of the dark exciton D_z with respect to the B_z line using the set of equations for the energy these exciton states in the

magnetic field B:

$$E(B_z) = \frac{1}{2}\delta_0 + \frac{1}{2}\sqrt{\delta_1^2 + \mu_B^2 g_{X,z}^2 B^2} + \gamma B^2, \quad (5.2)$$

$$E(D_z) = \frac{1}{2}\delta_0 - \frac{1}{2}\sqrt{\delta_1^2 + \mu_B^2 g_{X,z}^2 B^2} + \gamma B^2, \quad (5.3)$$

$$(5.4)$$

where δ_0 is an exchange splitting between in-plane and z -polarized transitions, δ_1 is a splitting between B_z and D_z line, $g_{X,z}$ is an exciton g -factor for z -polarized states, and γ a diamagnetic coefficient. Subtracting these two equations gives a much simpler formula dependent only on the g -factor $g_{X,z}$ and δ_1 :

$$E(B_z - D_z) = \sqrt{\delta_1^2 + \mu_B^2 g_{X,z}^2 B^2}. \quad (5.5)$$

The position of B_z and D_z line was found by fitting a Lorentzian function to the PL data. Next, we took the difference in $B_z - D_z$ energy and fitted the formula in eq. 5.5. We found the splittings δ_1 between B_z and D_z to be 482 μeV , 448 μeV and 466 μeV for dots A, B and C. For each dot the dark exciton is below B_x and B_y line.

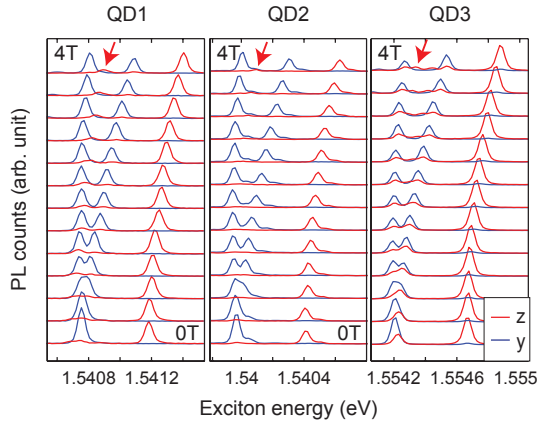


Figure 5.10 |Polarization-resolved spectra of 3 representative QDs in the undercut membrane. The magnetic field is applied along the sample growth direction (Faraday configuration) and the spectra are collected from the side edge of the sample.

5.7.4 Evaluation of amplitude of HH-LH mixing

Figure 5.11 describes the estimation of HH-LH mixing amplitude β (LH ratio) (see Eq. (1) of Ref.³⁴ for the definition) using the existing model by Tonin *et al.* We first fit polarization-angle-dependent intensity (collected by top configuration) of B₁ and B₂ lines by a cosine function and then we add the fitted intensities of both lines to obtain the polarization ellipse of the total in-plane emission intensity. Inset 1 of Fig. 5.11 shows the polar plot of the measured (B₁ - closed circles and B₂ - open circles) and fitted (solid lines) intensities as a function of polarization angle for the as-grown QD in Fig. 2a. Inset 2 is that of strained QD in Fig. 2c. Inset 3 is the analysis of a strained QD 5 μm away from the cleave edge where the strain situation is more ideally biaxial than near the edge. The triangular symbols (solid lines) in all polar plots are for measured (calculated) total in-plane emission intensities. The maximum (I_{max}) and minimum (I_{min}) of the polarization ellipses of total intensity (dotted lines in both polar plots) were used to calculate the linear polarization degree C ($= (I_{\text{max}} - I_{\text{min}}) / (I_{\text{max}} + I_{\text{min}})$). The values of β were estimated from the C versus β plot, as shown in Fig. 5.11 and is calculated using Eq. (7) of Ref.³⁴. The value of C that we obtained from the polarization ellipse of as-grown (inset 1) is 0.12 which corresponds to a value of 0.10 for β . For the strained QD near edge (inset 2), the values of C and β are 0.13 and 0.99 respectively. Surprisingly when the strained QD is away from the edge, where tensile strain is more ideally biaxial, the polarization degree decreases to 0.01 which corresponds to 100% LH in the ground state. The cross marks in Fig. 5.11 show C versus β co-ordinates for all QDs.

5.7.5 Numerical Results

While the model delivers clear results for the polarization of the eigenstates, it does not reveal the energetic splittings between the exciton states. We therefore calculate numerically, using the atomistic empirical pseudopotential method and configuration interaction³², the energetic splittings. The results for InGaAs QDs embedded in GaAs where the hole states have dominant heavy-hole character are well known. In order to obtain excitons with light-hole character we use the same approach as followed experimentally. We calculate the excitonic states, including the electron-hole exchange interaction³¹ for different GaAs QDs, embedded in $\text{Al}_x\text{Ga}_{1-x}\text{As}$. The structures are nearly strain-free and due to the rather large height/base ratio, the splitting between the dominant heavy- and dominant light-hole states is significantly reduced, compared to the InAs/GaAs case. Fig. 5.12 shows the heavy- and light-hole character of the first six hole states in an unstressed GaAs QD. The first hole state h_0 has over 90% heavy-hole character, but the deeper holes, which are only a few meV from h_0 have already a significant light-hole character. The composition dependence is non-monotonic, since the amount of light-hole mixing depends on the orbital symmetry of the states. To create a ground state hole (h_0) with dominant light-hole character, we apply tensile strain to the simulation cell which favors a light-hole ground state. The strain is

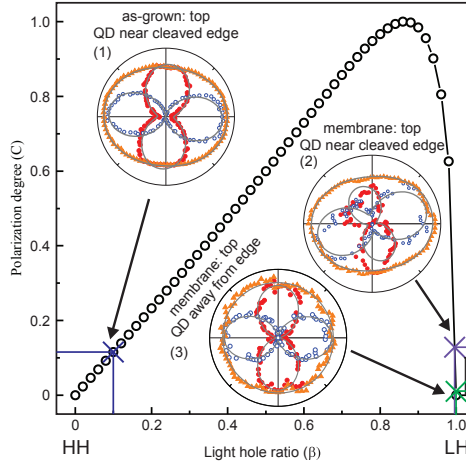


Figure 5.11 | Linear polarization degree C versus the mixing parameter β . The two polar plots are for the as-grown QD (top) and strained QD (bottom) demonstrated in the main text respectively.

defined as $\frac{a_s - a_0}{a_0}$ where a_s is the lattice constant of the stressed simulation cell and a_0 is the lattice constant of the unstressed structure. Under the stressed conditions, all the atomic positions are relaxed to minimize the strain energy, using the valence force field method³². In Fig. 5.4(a) we plot the heavy- and light-hole character of the first hole state h_0 as a function of the applied strain. We see that, already for rather moderate strain values, the character shifts from dominantly heavy-hole to dominantly light-hole.

In Fig. 5.4(b) we plot the excitonic fine structure as a function of the tensile strain. The size of the symbols is proportional to the oscillator strength of the transition. The energies are given relative to the lowest exciton states that is, in all cases, a dark state. The color of the symbols give the polarization property of the transitions, blue and black for in-plane polarization and red for out-of-plane (along [001]) polarization. The situation at zero strain corresponds to the well known situation where the two bright states are polarized in-plane and are split by the FSS. The dark states are nearly unsplit and at zero-energy in the Fig. 5.4(b).

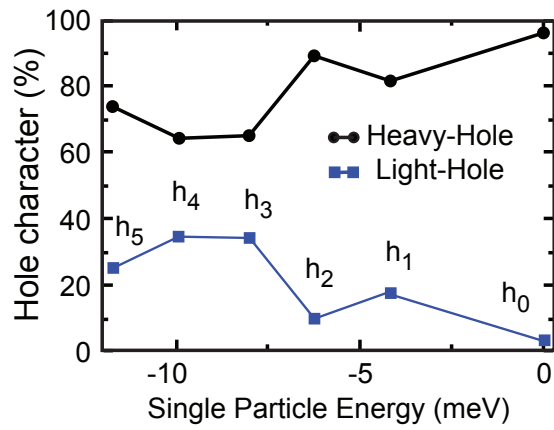


Figure 5.12 | Analysis of the hole character of the first six hole states in an unstrained GaAs QD with a shape constructed from representative AFM topographies. The energy is given with respect to the energy of the ground hole state h_0 .

5.8 Bibliography

- [1] A. Zrenner *et al.* Coherent properties of a two-level system based on a quantum-dot photodiode. *Nature* **418**, 612 (2002).
- [2] A. Ramsay. A review of the coherent optical control of the exciton and spin states of semiconductor quantum dots. *Semiconductor Science and Technology* **25**, 103001 (2010).
- [3] A. Greilich *et al.* Mode locking of electron spin coherences in singly charged quantum dots. *Science* **313**, 341 (2006).
- [4] D. Press, T. D. Ladd, B. Zhang and Y. Yamamoto. Complete quantum control of a single quantum dot spin using ultrafast optical pulses. *Nature* **456**, 218 (2008).
- [5] K. Nowack, F. Koppens, Y. V. Nazarov and L. Vandersypen. Coherent control of a single electron spin with electric fields. *Science* **318**, 1430 (2007).
- [6] S. Laurent *et al.* Electrical control of hole spin relaxation in charge tunable InAs/GaAs quantum dots. *Physical review letters* **94**, 147401 (2005).
- [7] B. D. Gerardot *et al.* Optical pumping of a single hole spin in a quantum dot. *Nature* **451**, 441 (2008).
- [8] K. De Greve *et al.* Ultrafast coherent control and suppressed nuclear feedback of a single quantum dot hole qubit. *Nature Physics* **7**, 872 (2011).
- [9] P. Michler *et al.* A quantum dot single-photon turnstile device. *Science* **290**, 2282 (2000).
- [10] N. Akopian *et al.* Entangled photon pairs from semiconductor quantum dots. *Physical review letters* **96**, 130501 (2006).
- [11] C. Salter *et al.* An entangled-light-emitting diode. *Nature* **465**, 594 (2010).
- [12] R. Vrijen and E. Yablonovitch. A spin-coherent semiconductor photo-detector for quantum communication. *Physica E: Low-dimensional Systems and Nanostructures* **10**, 569 (2001).
- [13] D. Sleiter and W. Brinkman. Using holes in GaAs as qubits: An estimate of the Rabi frequency in the presence of an external rf field. *Physical Review B* **74**, 153312 (2006).
- [14] H. Kosaka *et al.* Spin state tomography of optically injected electrons in a semiconductor. *Nature* **457**, 702 (2009).

-
- [15] D. Reiter, T. Kuhn and V. Axt. Coherent control of a single mn spin in a quantum dot via optical manipulation of the light hole exciton. *Physical Review B* **83**, 155322 (2011).
- [16] K. Schmidt, G. Medeiros-Ribeiro, M. Oestreich, P. Petroff and G. Döhler. Carrier relaxation and electronic structure in inas self-assembled quantum dots. *Physical Review B* **54**, 11346 (1996).
- [17] K. Karlsson *et al.* Fine structure of exciton complexes in high-symmetry quantum dots: Effects of symmetry breaking and symmetry elevation. *Physical Review B* **81**, 161307 (2010).
- [18] L. Besombes, K. Kheng and D. Martrou. Exciton and biexciton fine structure in single elongated islands grown on a vicinal surface. *Physical review letters* **85**, 425 (2000).
- [19] T. Belhadj *et al.* Impact of heavy hole-light hole coupling on optical selection rules in gaas quantum dots. *Applied Physics Letters* **97**, 051111 (2010).
- [20] L. Li *et al.* Control of polarization and dipole moment in low-dimensional semiconductor nanostructures. *Applied Physics Letters* **95**, 221116 (2009).
- [21] P. Ridha *et al.* Polarization properties of columnar quantum dots: effects of aspect ratio and compositional contrast. *Quantum Electronics, IEEE Journal of* **46**, 197 (2010).
- [22] V. Troncale, K. Karlsson, E. Pelucchi, A. Rudra and E. Kapon. Control of valence band states in pyramidal quantum dot-in-dot semiconductor heterostructures. *Applied Physics Letters* **91**, 241909 (2007).
- [23] Y. Huo, A. Rastelli and O. Schmidt. Ultra-small excitonic fine structure splitting in highly symmetric quantum dots on gaas (001) substrate. *Applied Physics Letters* **102**, 152105 (2013).
- [24] D. Owen, D. Lackner, O. Pitts, S. Watkins and P. Mooney. In-place bonding of gaas/ingaas/gaas heterostructures to gaas (0 0 1). *Semiconductor Science and Technology* **24**, 035011 (2009).
- [25] T. Zander *et al.* Epitaxial quantum dots in stretchable optical microcavities. *Optics express* **17**, 22452 (2009).
- [26] F. Ding *et al.* Tuning the exciton binding energies in single self-assembled ingaas/gaas quantum dots by piezoelectric-induced biaxial stress. *Physical review letters* **104**, 067405 (2010).
- [27] G. L. Bir, G. E. Pikus, P. Shelnitz and D. Louvish. *Symmetry and strain-induced effects in semiconductors*, volume 624. Wiley New York (1974).

- [28] F. Meier and B. P. Zakharchenya. *Optical orientation*. Access Online via Elsevier (1984).
- [29] M. Bayer *et al.* Fine structure of neutral and charged excitons in self-assembled in (ga) as/(al) gaas quantum dots. *Physical Review B* **65**, 195315 (2002).
- [30] B. Witek *et al.* Measurement of the g-factor tensor in a quantum dot and disentanglement of exciton spins. *Physical Review B* **84**, 195305 (2011).
- [31] G. Bester, S. Nair and A. Zunger. Pseudopotential calculation of the excitonic fine structure of million-atom self-assembled in $\{1-x\}$ ga $\{x\}$ as/gaas quantum dots. *Physical Review B* **67**, 161306 (2003).
- [32] G. Bester. Electronic excitations in nanostructures: an empirical pseudopotential based approach. *Journal of Physics: Condensed Matter* **21**, 023202 (2009).
- [33] A. Rastelli *et al.* Hierarchical self-assembly of gaas/algaas quantum dots. *Physical review letters* **92**, 166104 (2004).
- [34] C. Tonin *et al.* Polarization properties of excitonic qubits in single self-assembled quantum dots. *Physical Review B* **85**, 155303 (2012).
- [35] R. Trotta *et al.* Nanomembrane quantum-light-emitting diodes integrated onto piezoelectric actuators. *Advanced Materials* **24**, 2668 (2012).
- [36] Y. Huo *et al.* Semiconductor quantum dots with light-hole exciton ground state: fabrication and fine structure. *arXiv preprint arXiv:1208.6554* (2012).
- [37] J. Plumhof *et al.* Tuning of the valence band mixing of excitons confined in gaas/algaas quantum dots via piezoelectric-induced anisotropic strain. *Physical Review B* **87**, 075311 (2013).

IMPACT OF STRAIN AND SHAPE SYMMETRY ON SPIN STATES

The shape symmetry of semiconductor quantum dots and strain distribution have a tremendous influence on the exciton spin states and emitted photons polarization. The fine structure splitting of the heavy hole (HH) exciton states, which is sensitive to the dot shape elongation, is a main obstacle in entangled photon pairs generation. The shape elongation results not only in the mixing of the HH exciton states, but leads also to the HH and light hole (LH) exciton states mixing. Importantly, all of the impressive steps towards quantum computing with spins trapped in quantum dots, such as the spin initialization, optical spin manipulation and the spin state readout, rely on the purity of the exciton polarization selection rules, hence the hole state purity. In this chapter we demonstrate and explain the HH-LH exciton mixing in epitaxial quantum dots. In particular, we show the experimental evidence of hole spin state mixing caused by two leading mechanisms: Luttinger-Kohn terms and hole-electron exchange.

6.1 Observation of a strong heavy-light hole spin mixing

Before we managed to demonstrate a LH exciton with negligible mixing in quantum dots (see chapter 5), we went through a series of attempts with quantum dots of distorted shapes. A novel method developed to induce tensile strain in nanomembranes containing quantum dots¹⁻⁴ proved to be sufficient to reorder energetically the LH and HH band. However, the shape asymmetry of the quantum dot prevented us from observing clean polarization selection rules for the LH exciton. Here we describe the HH-LH mixing mechanism leading to the distortion of LH exciton polarization.

6.1.1 Quantum dot sample description

The quantum dots studied here were obtained by local droplet etching of nanoholes into a GaAs surface⁵⁻⁷ followed by heterostructure overgrowth^{8,9}. The advantage of this method over strain-induced self-assembly is that the height of the quantum dots, which directly influences the LH-HH splitting, can be controlled in a wide range even when the depth of the holes is fixed.¹⁰ In addition, these QDs can display single-dot emission linewidths narrower than $25 \mu\text{eV}$ ⁸, allowing detailed investigations of the excitonic fine structure to be performed. To gather information on the dot morphology, we measured by atomic force microscopy (AFM) the surface morphology of two additional samples where the growth was interrupted after the deposition of the bottom barrier and after GaAs overgrowth, respectively. AFM images of two similarly shaped nanoholes found on the two samples are shown on the left side of fig. 6.1(a). The approximate shape of the GaAs quantum dots can be obtained by subtracting the two images, as shown in fig. 6.1(a). Linescans of the quantum dot interfaces as well as of the resulting quantum dot shape along two orthogonal directions are shown on the right part of fig. 6.1(a). We see the GaAs-filled nanohole has an irregular shape, elongated in the [110] direction. Similar conclusions can be drawn by inspection of other nanoholes. To generate tensile strain into the GaAs quantum dots, we follow an approach similar to Refs.¹⁻³. The quantum dots were placed into symmetrically pre-stressed membranes which include one $\text{In}_{0.2}\text{Al}_{0.3}\text{Ga}_{0.5}\text{As}$ stressor layer below and another above the active structure (see fig. 6.1(b) left). After defining patterns by optical lithography and wet chemical etching, we selectively remove a sacrificial $\text{Al}_{0.75}\text{Ga}_{0.25}\text{As}$ layer placed below the membrane structure. In this way the membranes are undercut and bond-back to the underlying substrate, as shown in the sketch on the right of fig. 6.1 (b). After release, the strain, which was originally confined into the InAlGaAs layers, is shared also with the initially unstrained heterostructure (see horizontal arrows in fig. 6.1(b), with lengths proportional to the strain magnitudes). Strain was quantified by X-ray diffraction measurements of a similar sample containing a GaAs layer instead of the (Al, Ga)As heterostructure between the $\text{In}_{0.2}\text{Al}_{0.3}\text{Ga}_{0.5}\text{As}$ layers. From the position of the peak associated to strained GaAs we obtain a strain value of 0.36% (see ref.⁴ for more details).

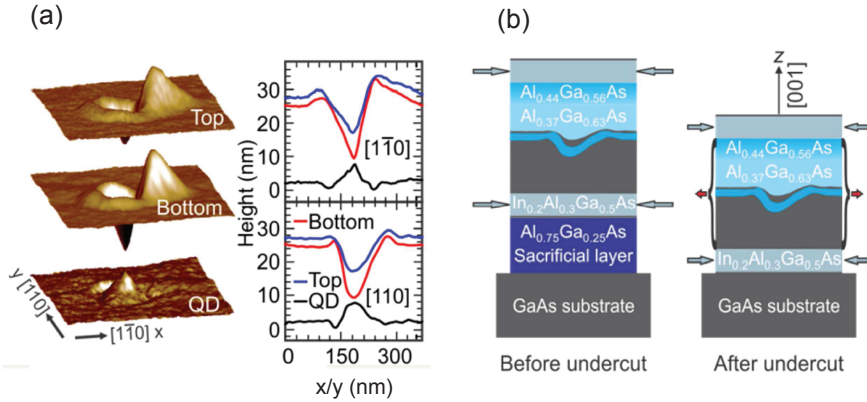


Figure 6.1 | (a) Representative AFM images of the surface of GaAs-filled AlGaAs nanoholes (Top) and of the AlGaAs nanoholes (Bottom). The difference between the two images provides the approximate morphology of the resulting GaAs quantum dot. Linescans of the AFM images along $[1\bar{1}0]$ and $[110]$ crystal directions are shown on the right side. (b) Side-view sketches of as grown sample structure before (left) and after removal of the sacrificial layer (right). The length of the horizontal arrows is proportional to the magnitude of in-plane strain in the layers.

6.1.2 Experimental results

Polarization resolved micro-photoluminescence in magnetic field was studied for several dots in the as grown sample and in the undercut membrane. All of the dots present very reproducible spectral features, which are shown in fig. 6.2 for two representative dots (one in the as grown sample and one in the undercut membrane). A quantum dot in the as grown sample exhibits a slightly distorted behavior of a HH exciton. In fig. 6.2(a), next to two bright states, a very weak emission from the dark states, which lies $140.8 \mu\text{eV}$ below the bright doublet, is observed. Spectra in fig 6.2(b) show that the emission of the dark states (pointed with arrows) is not exceeding 7% of bright states intensity. The appearance of dark states can be linked to the non symmetric shape of the dot that leads to the HH-LH mixing term S (see eq. 2.42). Besides this, the HH exciton bright state reveal expected polarization: linear at zero magnetic field, and a high degree of circular polarization at $B = 8 \text{ T}$. We observe a dramatic change of the spectral features for a quantum dot in the undercut membrane in fig. 6.2(c). First of all, the emission energy of quantum dots is shifted to the red, which is consistent with our expectations of tensile strain (fig. 2.5). Secondly, four exciton lines are visible, as predicted for a LH state (see chapter 3). However, in a standard top-view micro-photoluminescence geometry, two LH exciton states polarized in z direction should not be visible. Here, as we look at the spectra in fig. 6.2(d), all the

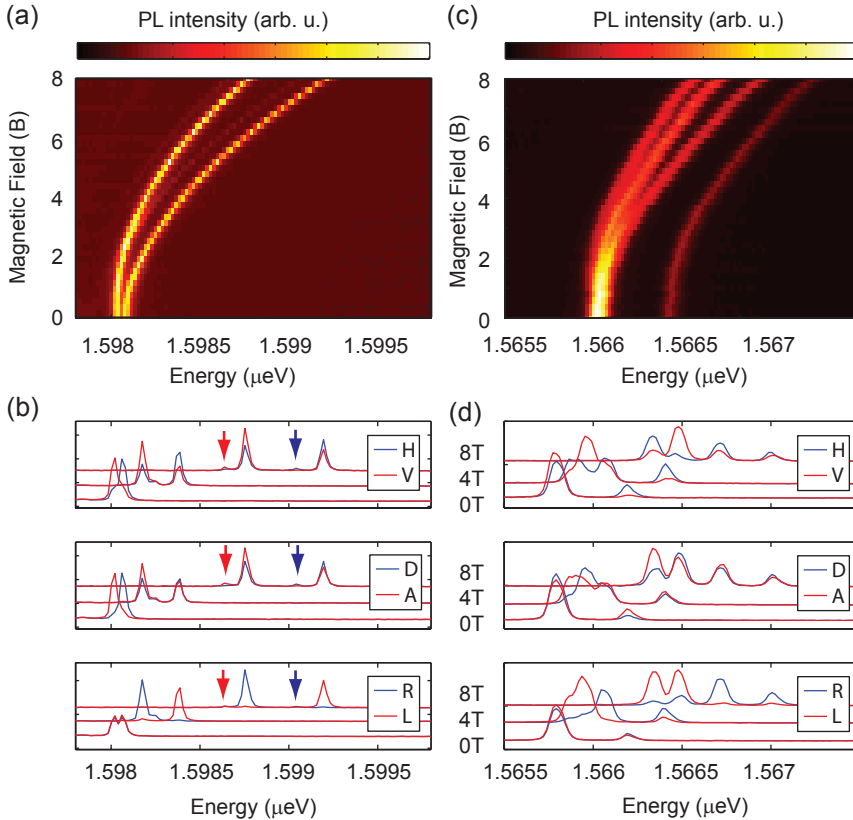


Figure 6.2 | Spectral fingerprints in the magnetic field along the growth direction z (Faraday configuration) of representative quantum dots in (a, b) the as grown sample and (c, d) the undercut membrane. (c,d) Polarization-resolved $\mu\text{-PL}$ spectra of those quantum dots at 0, 4 and 8T. Horizontal (H) and vertical (V) polarization is not aligned with any specific crystallographic axis of the sample. The arrows in (b) point at a weak emission attributed to the HH exciton dark state. In the undercut membrane, the energies of the exciton states in (c) resemble the LH exciton features, however, not the polarization and intensity of the lines in (d).

lines have a rather pronounced intensity. In order to compare the nature of these lines with the case of high purity LH exciton, we subtract the diamagnetic shift ($\gamma = 11.4$) and focus on the Zeeman energy in fig. 6.3(b). The energy of the lines can be fitted with the Zeeman Hamiltonian for a LH exciton. We therefore can identify which lines should exhibit purely z -polarization. As labeled in fig. 6.3(b), the line of the highest energy resembles the B_z exciton, and $398 \mu\text{eV}$ below we find a state resembling a dark state D_z of the LH exciton. In addition, we show that the behavior of the quantum dot in the as-grown sample can be very well reproduced by the Zeeman Hamiltonian for the HH exciton (fig. 6.3(a)).

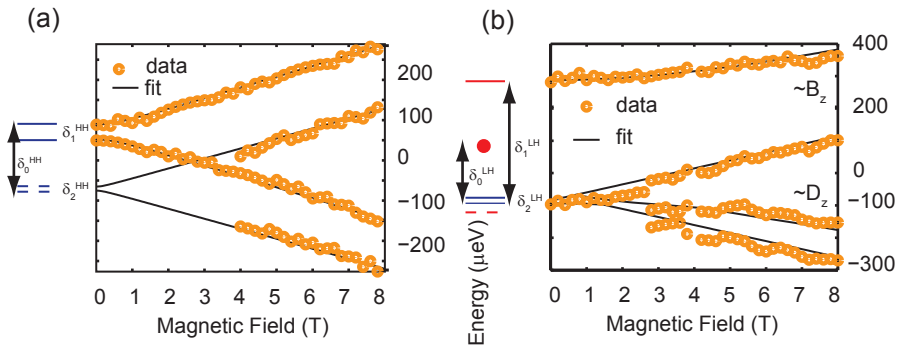


Figure 6.3 | The Zeeman energy of the exciton states in (a) the as grown sample and (b) the undercut membrane extracted from the experiment by diamagnetic shift subtraction (points). Solid lines represent the fit to the Zeeman Hamiltonian for (a) the HH exciton and (b) the LH exciton.

6.1.3 Discussion and conclusion

As apparent from fig. 6.3, the energies of four exciton transitions in the undercut membrane follow the expectations for the LH exciton in Faraday geometry. Similarly, the energies of exciton states observed in the as grown sample can be described by the Zeeman Hamiltonian for the HH exciton. Only the polarization and the oscillator strength does not match with a pure HH or a pure LH exciton case. Apparently, the hole spin state, hence the exciton polarization, is a very sensitive measure of the quantum dot symmetry. Distortion from the polarization of the pure HH and LH exciton case can be explained by mixing of the HH spin up $|\frac{3}{2}, \frac{3}{2}\rangle$ with the LH spin up $|\frac{3}{2}, \frac{1}{2}\rangle$ (and the HH spin down with the LH spin down). The effect of such mixing on polarization of lines is explained in fig. 6.4. HH exciton dark states acquire circular polarization due to the admixture of the LH states, as seen in our experiment (fig. 6.2). On the other hand, z -polarized states of the LH exciton gain a component

of circular polarization related to the admixture of the HH state. This effect is very strong for the quantum dot in the undercut membrane. Surprisingly, the state resembling D_z , which should not be visible in our micro-photoluminescence geometry, has the highest intensity of all lines. Let us look again at the spectra for the undercut membrane in fig.6.2(d). A line resembling D_z reveals a high degree of left handed circular polarization ($L \equiv \sigma^-$), whereas a state similar to B_z is mostly right handed circularly polarized ($R \equiv \sigma^+$). Each of these LH-like states couples to one of the circular HH exciton states. We shall now recall a possible origin of such hole mixing.

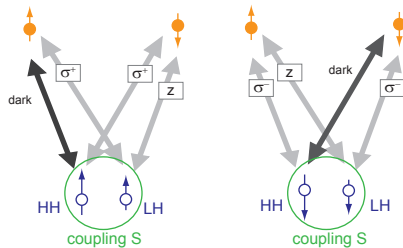


Figure 6.4 | Polarization components of the photons emitted from a HH-LH mixed state. The term S from the Luttinger-Kohn Hamiltonian couple parallel HH and LH spins. Transitions forbidden for a purely HH state gain circular polarization. Mixture of z polarized states with circularly polarized states (σ^+ and σ^-) is expected.

First of all, it can be due to the shape asymmetry, which makes the S term in the Luttinger-Kohn Hamiltonian non-negligible:

$$S = \left(\frac{\hbar^2}{2m_0}\right)2\sqrt{3}\gamma_3((k_x - ik_y)k_z). \quad (6.1)$$

This should be the case for strain free quantum dots in the as grown sample. We probe the polarization of the GaAs at the location of the quantum dot studied here (fig. 6.5(a)). We discover that even the emission from the ≈ 100 nm thick GaAs layer below the quantum dot, is slightly polarized, and there are two split exciton peaks. This could indicate some non uniform strain distribution already present in the as grown structure. In the undercut membrane, where tensile strain is induced, the effect of the mixing is more dramatic, as confirmed by a nonuniform polarization in fig 6.5(b). It is likely that the asymmetric shape of the dot results in uneven distribution of strain. If shear strain is built up in a quantum dot, then the mixing between HH and LH spins is enhanced by a term:

$$S_\epsilon = -d(\epsilon_{zx} - i\epsilon_{yz}). \quad (6.2)$$

The polarization of GaAs at the location of the quantum dot in the undercut membrane shows even stronger polarization than in the as grown sample. It is a signature of further reduction of the structure symmetry.

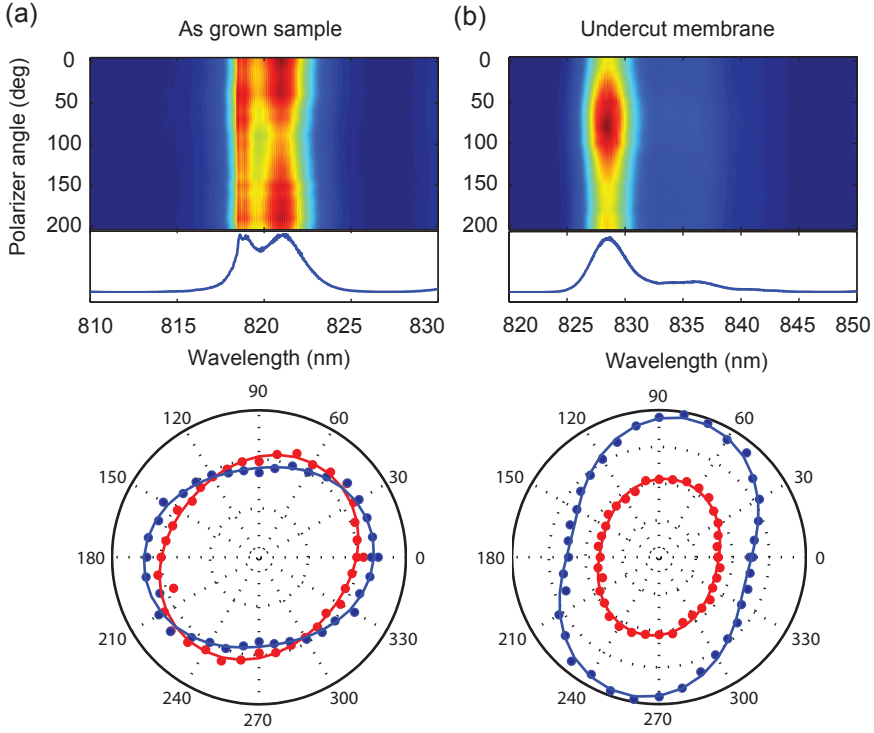


Figure 6.5 | Polarization ellipse recorded for the GaAs emission (originating from the ≈ 100 nm thick layer below the quantum dot). (a) The as grown sample at the position of the studied quantum dot and (b) the undercut membrane at the location of the quantum dot.

In conclusion, we have identified a dominant term responsible for the HH-LH mixing in our asymmetric epitaxial quantum dots. This work emphasizes the importance of the quantum dot symmetry and strain uniformity for the purity of hole spin states.

6.2 Observation of the exchange interaction induced mixing

The Luttinger-Kohn Hamiltonian helps us predict the order and the character of the valence sub-bands in a semiconductor nanostructure based on the shape of the confining potential and strain. Once the valence ground state is defined in this method, there is yet another mechanism which can modify spin states, however, not just the hole spins, but the overall exciton spins. The exchange Hamiltonian, as we learnt in

chapter 3 couples the electron and hole spin:

$$H_{exch} = - \sum_{i=x,y,z} (a_i \sigma_i \otimes J_i + b_i \sigma_i \otimes J_i^3). \quad (6.3)$$

In chapter 3 we gave the matrix form of this interaction for either a pure HH or a pure LH exciton 4x4 subspace. Interestingly, if the exchange Hamiltonian is calculated in a complete 8 dimensional exciton states basis (4 HH excitons + 4 LH excitons), we discover the off diagonal terms that couple both the HH and LH exciton subspaces (see appendix A). The 8x8 exchange Hamiltonian takes a form (for the exciton $|J_{z,h}, S_{z,e}\rangle$ basis states $|+\frac{3}{2}, +\frac{1}{2}\rangle, |+\frac{3}{2}, -\frac{1}{2}\rangle, |-\frac{3}{2}, +\frac{1}{2}\rangle, |-\frac{3}{2}, -\frac{1}{2}\rangle, |+\frac{1}{2}, +\frac{1}{2}\rangle, |+\frac{1}{2}, -\frac{1}{2}\rangle, |-\frac{1}{2}, +\frac{1}{2}\rangle, |-\frac{1}{2}, -\frac{1}{2}\rangle$):

$$H_{exch} = \begin{pmatrix} H_{exch}^{HH} & H_{exch}^{HH-LH} \\ H_{exch}^{HH-LH\dagger} & H_{exch}^{LH} \end{pmatrix} \quad (6.4)$$

Where H_{exch}^{HH-LH} is a HH-LH exciton mixing term:

$$H_{exch}^{HH-LH} = \frac{1}{2} \begin{pmatrix} 0 & \Delta_2 & 0 & 0 \\ \Delta_1 & 0 & 0 & 0 \\ 0 & 0 & 0 & \Delta_1 \\ 0 & 0 & \Delta_0 & 0 \end{pmatrix} \quad (6.5)$$

Apparently, the exchange interaction is not only responsible for mixing of the HH bright exciton states, which is a main obstacle towards entangled photon pairs generation from a biexciton cascade. It is also responsible for mixing of the HH and the LH excitons. Coupling between the HH and LH excitons of $J_X = \pm 1$ momentum:

$$\left| +\frac{3}{2}, -\frac{1}{2} \right\rangle_{LH} \leftrightarrow \left| +\frac{1}{2}, +\frac{1}{2} \right\rangle_{LH}, \quad (6.6)$$

$$\left| -\frac{3}{2}, +\frac{1}{2} \right\rangle_{LH} \leftrightarrow \left| -\frac{1}{2}, -\frac{1}{2} \right\rangle_{LH}, \quad (6.7)$$

is given by the Δ_1 term:

$$\Delta_1 = -\frac{\sqrt{3}}{2}(a_x + a_y) - \frac{7\sqrt{3}}{8}(b_x + b_y). \quad (6.8)$$

Here a_i and b_i ($i = x, y, z$) are spin-spin coupling constants that determine also the exchange energies δ_j^h ($j = 0, 1, 2$) of the $h = LH$ and $h = HH$ exciton. The HH

exciton states of $J_X = \pm 2$ momentum couple to the LH exciton states of $J_X = 0$:

$$\left| +\frac{3}{2}, +\frac{1}{2} \right\rangle_{LH} \leftrightarrow \left| +\frac{1}{2}, -\frac{1}{2} \right\rangle_{LH}, \quad (6.9)$$

$$\left| -\frac{3}{2}, -\frac{1}{2} \right\rangle_{LH} \leftrightarrow \left| -\frac{1}{2}, +\frac{1}{2} \right\rangle_{LH}. \quad (6.10)$$

The strength of this coupling is determined by Δ_2 :

$$\Delta_2 = -\frac{\sqrt{3}}{2}(a_x - a_y) - \frac{7\sqrt{3}}{8}(b_x - b_y). \quad (6.11)$$

It can be easily shown that the strength of Δ_1 and Δ_2 coupling relates to the fine structure of the HH and LH exciton: $\Delta_2 = \sqrt{3}/2(\delta_2^{LH} - \delta_1^{HH})$ and $\Delta_1 = \sqrt{3}/2(\delta_1^{LH} - \delta_2^{HH})$.

In most of the experiments, mixing induced by the exchange interaction can be regarded as negligible, unless the bright states of the HH and LH exciton are almost degenerate. In the following paragraphs we investigate such a case.

6.2.1 Quantum dot sample description

The GaAs quantum dots were grown with the same method as described in section 6.1.1. In fig. 6.6 the AFM image of the nanoholes is shown. In the growth process, these nanoholes are filled with GaAs to form a quantum dot. Therefore the geometry of the nanohole reflects the one of the quantum dot. First of all, the nanoholes are elongated along the $[-110]$ direction. Secondly, most the nanoholes have a relatively deep insertion. Such deep hole leads to the formation of a quantum dot with strong confinement in $x-y$ plane, in contrast to the usual case where the strongest confinement is along the growth direction z . As we discussed in section 2.3.2, such geometry can lift the LH band above the HH band.

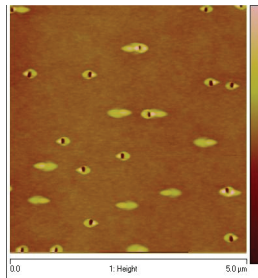


Figure 6.6 | AFM image of elongated and deep nanoholes in AlGaAs. These nanoholes are filled with GaAs to form quantum dots.

6.2.2 Experimental results

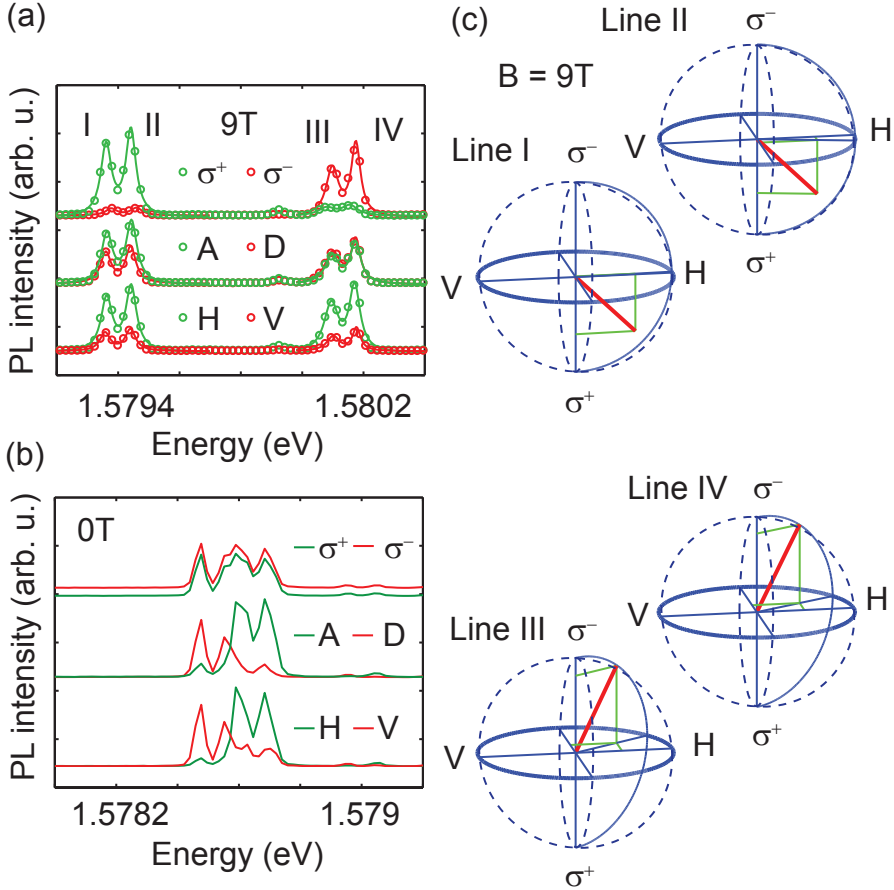


Figure 6.7 | Polarization resolved ground state emission from a quantum dot at (a) $B=0$ T and (b) $B=9$ T. Polarization state of four emission lines at $B=9$ T represented on Poincare spheres.

All of the quantum dots in this sample exhibit a very peculiar spectrum. A representative ground state emission from a quantum dot at zero magnetic field is shown in fig. 6.7(a). A polarization selective measurement helps us recognize four lines. These lines are clearly linearly polarized, since the spectra in circular polarization basis σ^+ and σ^- are equivalent. A pair of lines on the lower energy side of the spectrum is polarized in between the vertical V and diagonal D , whereas the pair of lines of higher energy is polarized in between the horizontal H and antidiagonal A polarization. Since

it is difficult to resolve the individual line polarization, it is not possible to say whether the pairs of lines are perfectly orthogonal to each other. At $B = 9$ T, however, the pairs are better separated (fig. 6.7(b)). Still, the separation within the pair does not increase in the magnetic field. It is possible to calculate the Stokes parameters for each line and represent the polarization state on the Poincare sphere, as shown in fig. 6.7(c). Lines in the second pair (line *III* and *IV*) are close to σ^- state. Lines in the first pair, on the other hand, are between the σ^+ state and the equator (H polarization). These features are reproducible for all quantum dots. The separation between the lines in the pair vary slightly from dot to dot, sometimes it is hard to resolve the individual line in a pair. Nonetheless, the separation between the lines in each pair does not seem to be visibly affected by the magnetic field, only the splitting between the pairs. This conclusion is supported by fig. 6.9(a), which shows the energy of the four lines in fine steps for another quantum dot in magnetic field.

6.2.3 Discussion and conclusion

As we have learnt in section 6.1, that a dominantly LH exciton can exhibit four exciton lines in the top-view micro-photoluminescence geometry, when coupled to the HH exciton by a term S in Luttinger Kohn Hamiltonian. However, such case should be excluded here, since the splitting between the lines is never as large as expected for a LH exciton ($\approx 400 \mu eV$). It is also not likely that these lines represent other than a neutral X^0 excitonic complex. All four lines follow the same power dependence (not shown) and appear to be a ground state excitonic emission. In order to interpret the unusual spectrum of the neutral exciton shown in fig. 6.7, we focus on the off-diagonal terms in the exchange Hamiltonian which are responsible for the HH and LH exciton coupling, Δ_1 and Δ_2 (see eq. 6.11 and 6.11). For simplicity, we neglect for a moment other terms in the exchange Hamiltonian and assume that the basis HH and LH exciton states are the eigenstates in a quantum dot ($|+\frac{3}{2}, -\frac{1}{2}\rangle, |-\frac{3}{2}, +\frac{1}{2}\rangle, |+\frac{1}{2}, +\frac{1}{2}\rangle, |-\frac{1}{2}, -\frac{1}{2}\rangle$). This situation can be approximated in the magnetic field in Faraday geometry¹¹. Fig. 6.8 shows schematically the HH and LH exciton states split by the Zeeman term $\mu_B(g_{z,e} \pm g_{z,h})B_z$ in the external magnetic field B_z . Bright states of the HH exciton are circularly polarized in Faraday configuration, σ^+ for a $|+1\rangle_{HH} = |+\frac{3}{2}, -\frac{1}{2}\rangle$ state and σ^- for the $| -1\rangle_{HH} = |+\frac{3}{2}, -\frac{1}{2}\rangle$ state. Similarly, the in-plane polarized states of a LH exciton are circular: σ^+ for the $|+1\rangle_{LH} = |+\frac{1}{2}, +\frac{1}{2}\rangle$ and σ^- for the $| -1\rangle_{LH} = |-\frac{1}{2}, -\frac{1}{2}\rangle$. Now, if these states are sufficiently close, almost degenerate, then we can consider coupling among them induced by Δ_1 . The result of such coupling, as shown in fig. 6.8, gives a pair of σ^+ polarized states, and a pair of σ^- polarized states.

The splitting between the lines within a pair is mostly linked to Δ_1 and the initial HH-LH exciton splitting Q , as well as to the splitting between the HH states δ_1^{HH} and LH states δ_2^{LH} . However, it should not be affected by the magnetic field (it is not true only for small values of the magnetic field, when we cannot yet approximate

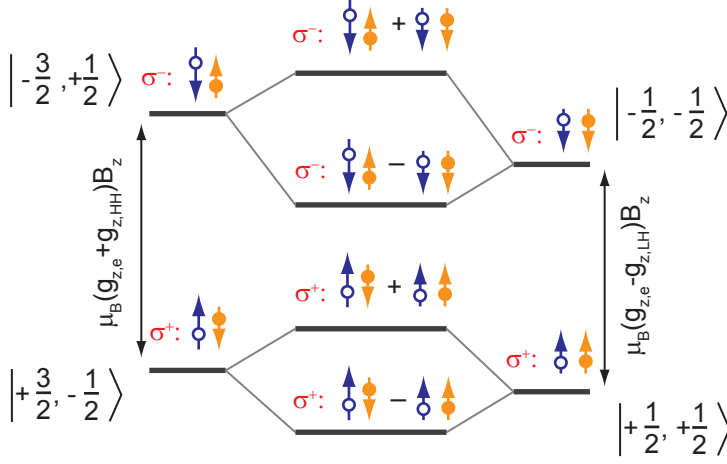


Figure 6.8 | A schematic explanation of the exciton states and their polarization resulting from the HH-LH mixing caused by the coupling term Δ_1 . For clarity, we consider a situation in the external magnetic field along the z direction (Faraday geometry), which allows us to neglect other exchange terms in the exchange Hamiltonian.

the exciton states with $|\pm 1\rangle_{HH/LH}$. The lines within a pair, being composed of the same combination of electron and hole spins, have the same g -factors. Only the two pairs split apart in the magnetic field. This reasoning already gives quite satisfying qualitative understanding. Nonetheless, it is still needed to find a Hamiltonian which could quantitatively reproduce our experimental data. To start with, we will narrow down the 8 dimensional space of the HH and LH exciton to the excitons measurable in our micro-photoluminescence geometry. Therefore we can neglect two z polarized states of the LH exciton and two dark states of the HH exciton. We are left with the following basis:

$$\begin{aligned}
 | +1 \rangle_{HH} &= \left| +\frac{3}{2}, -\frac{1}{2} \right\rangle, & | -1 \rangle_{HH} &= \left| -\frac{3}{2}, +\frac{1}{2} \right\rangle, \\
 | +1 \rangle_{LH} &= \left| +\frac{1}{2}, +\frac{1}{2} \right\rangle, & | -1 \rangle_{LH} &= \left| -\frac{1}{2}, -\frac{1}{2} \right\rangle.
 \end{aligned} \tag{6.12}$$

It is allowed to make this simplification, since there is no matrix element in the 8×8 exchange Hamiltonian that couples the subspace in eq. 6.12 with the remaining four exciton states. Note that Δ_2 couples only the z polarized LH states with HH dark

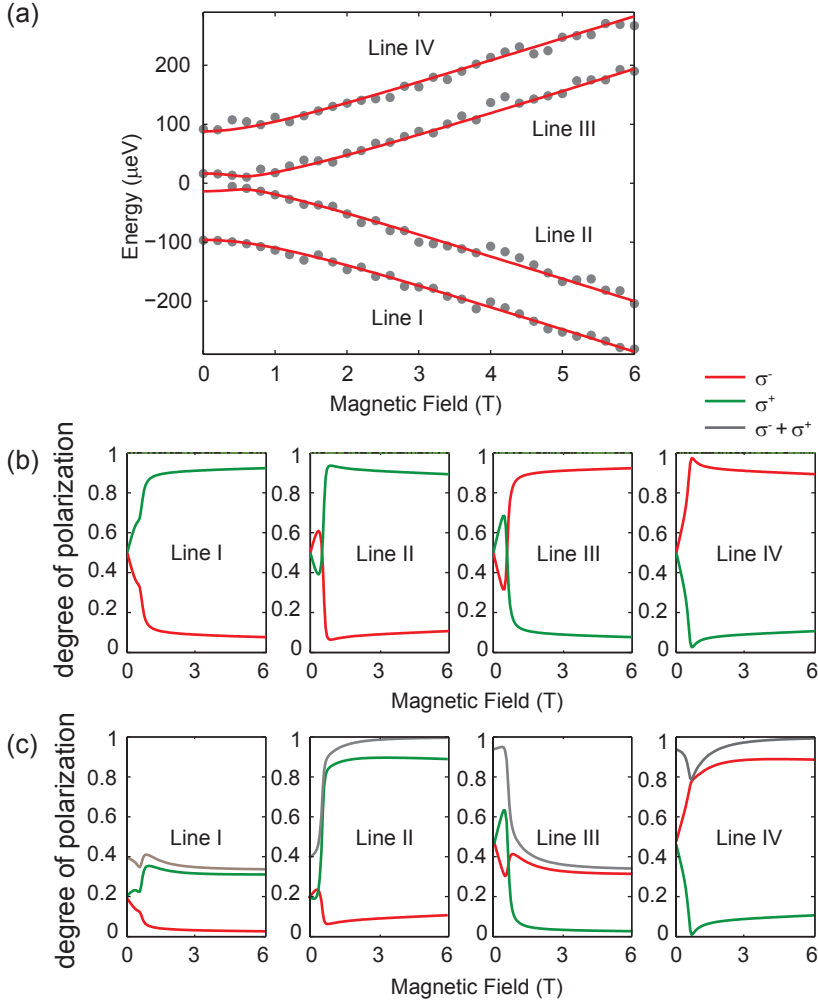


Figure 6.9 | (a) Experimental data points representing the Zeeman energy of four exciton transitions fit with a model based of the exchange interaction induced spin mixing. (b) Within the model, predicted polarization of the line *I*, *II*, *III* and *IV*. Equal oscillator strength for the HH and LH exciton is assumed. (c) Expected polarization of lines and intensity when HH to LH oscillator strength ratio has a typical value 3.

states. Now, the Hamiltonian for the basis states in eq. 6.12 can be written:

$$H^{HH-LH} = \frac{1}{2} \begin{pmatrix} \delta_0^{HH} + Q & \delta_1^{HH} & \Delta_1 & 0 \\ \delta_1^{HH} & \delta_0^{HH} + Q & 0 & \Delta_1 \\ \Delta_1 & 0 & -\delta_0^{LH} - Q & \delta_2^{LH} \\ 0 & \Delta_1 & \delta_2^{LH} & -\delta_0^{LH} - Q \end{pmatrix} \quad (6.13)$$

It is basically an exchange Hamiltonian with an additional diagonal term Q from the Luttinger Kohn Hamiltonian which sets the HH-LH splitting. As apparent from fig. 6.9(a), such Hamiltonian reproduces the experimental data for a set of parameters:

$$\delta_0^{HH} + Q = 72.5\mu eV \quad (6.14)$$

$$-\delta_0^{LH} - Q = -87.5\mu eV \quad (6.15)$$

$$\Delta_1 = 55.9\mu eV \quad (6.16)$$

$$\delta_1^{HH} = 73\mu eV \quad (6.17)$$

$$\delta_2^{LH} = 98\mu eV \quad (6.18)$$

Are these numbers reasonable? The fine structure splitting of the HH bright exciton and δ_1^{HH} as well as the LH exciton δ_2^{LH} is very large. It implies $a_x \neq a_y$ and $b_x \neq b_y$, which is a signature of a strongly elongated quantum dot. From the coupling term Δ_1 we deduce $\delta_1^{LH} - \delta_2^{HH} = 64.5 \mu eV$. In symmetric dots δ_1^{LH} can be as high as $500 \mu eV$, whereas δ_2^{HH} is usually close to zero (see chapter 5). However, we have observed in section 6.1, that for the asymmetric quantum dot δ_1^{LH} is below $400 \mu eV$, while δ_2^{HH} is expected to increase with shape asymmetry. Therefore the values might be reasonable, however, more experimental data is needed to draw a strong conclusion. It is not possible to extract an independent value of the HH-LH splitting Q in the quantum dot. If δ_0^{LH} and δ_0^{HH} have similar values and are smaller than $80 \mu eV$, then Q is positive and the HH band is above the LH band. However, it is more common in experiments to observe δ_0^{LH} and δ_0^{HH} higher than $80 \mu eV$. In this case the LH band has to be on top of the valence band. Again, it is hard to say something concrete for this particular dot shape. Nonetheless for tall dots we would rather expect the LH band to be a ground state.

We have also checked, if the H^{HH-LH} Hamiltonian gives expected polarization of exciton states. In fig. 6.9(b) we plot the resulting polarization of four lines projected on σ^+ and σ^- polarization. The agreement with our experiment is very good: lines *I* and *II* are indeed mainly σ^+ polarized and lines *III* and *IV* are σ^- polarized. In this plot, we assumed that the LH exciton oscillator strength is the same as the HH one. Based on chapter 2, we know that circularly polarized LH exciton transitions are expected to be 3 times weaker than the HH exciton transitions. We took this ratio into account in fig. 6.9(c). It does not change the polarization of lines, however, it affects the relative intensity of the lines. Spectra of the quantum dot in fig. 6.7, show just a tiny intensity imbalance between the lines. One might be concerned that this inconsistency is enough to question our model. We could also argue that the ratio between the HH and LH exciton oscillator strength does not have to be exactly 3. We get this ratio by making an assumption that the dipole moments for the p_x , p_y and p_z orbitals are the same. In my opinion this might be a misleading simplification, since the quantum dot confinement is not the same in x , y and z direction.

In conclusion, we have discussed the possibility of HH-LH exciton mixing due to exchange interaction. We have presented experimental data for an asymmetric quantum dot which can be very well explained by exchange induced mixing. However, I would be reluctant to claim that this is the only possible explanation for the observed effects. In a quantum dot of a very irregular shape there might be plenty of spin mixing mechanisms taking place. Nonetheless, since growing quantum dots in a strain-free method of droplet epitaxy becomes more and more popular, it is crucial to understand what happens if the HH and the LH exciton states are almost degenerate.

6.3 Conclusion

In summary, shape and/or strain anisotropy results in the HH and LH spin states mixing, which is reflected in polarization of neutral exciton photons. Identifying the type of distortion from the pure HH and LH exciton polarization gives us insight into the dominant spin mixing mechanism. We have described a mixing term S in the Luttinger-Kohn Hamiltonian and shown how it is manifested in the polarization resolved exciton spectrum. In addition, we have considered yet another sensitive measure of the dot asymmetry, which is the exchange interaction. Exchange interaction can lead to another unique spectral fingerprint of the exciton mixing. This work emphasizes the importance of a controllable and reproducible growth technique of highly symmetric quantum dots. On the other hand it develops understanding of the effects that can result from strain tuning of quantum dots^{8,12,13}.

6.4 Bibliography

- [1] G. Cohen, P. Mooney, V. Paruchuri and H. Hovel. Dislocation-free strained silicon-on-silicon by in-place bonding. *Applied Physics Letters* **86**, 251902 (2005).
- [2] D. Owen, D. Lackner, O. Pitts, S. Watkins and P. Mooney. Bonding of elastically strain-relaxed gaas/ingaas/gaas heterostructures to gaas (001). *ECS Transactions* **16**, 271 (2008).
- [3] D. Owen, D. Lackner, O. Pitts, S. Watkins and P. Mooney. In-place bonding of gaas/ingaas/gaas heterostructures to gaas (0 0 1). *Semiconductor Science and Technology* **24**, 035011 (2009).
- [4] Y. Huo *et al.* Semiconductor quantum dots with light-hole exciton ground state: fabrication and fine structure. *arXiv preprint arXiv:1208.6554* (2012).
- [5] J. Lee, Z. M. Wang, N. Strom, Y. I. Mazur and G. Salamo. Ingaas quantum dot molecules around self-assembled gaas nanomound templates. *Applied physics letters* **89**, 202101 (2006).
- [6] C. Heyn, A. Stemmann and W. Hansen. Nanohole formation on algaas surfaces by local droplet etching with gallium. *Journal of Crystal Growth* **311**, 1839 (2009).
- [7] E. Zallo, P. Atkinson, A. Rastelli and O. G. Schmidt. Controlling the formation of quantum dot pairs using nanohole templates. *Journal of Crystal Growth* **338**, 232 (2012).
- [8] S. Kumar *et al.* Strain-induced tuning of the emission wavelength of high quality gaas/algaas quantum dots in the spectral range of the ^{87}rb d_2 lines. *Applied Physics Letters* **99**, 161118 (2011).
- [9] P. Atkinson, E. Zallo and O. Schmidt. Independent wavelength and density control of uniform gaas/algaas quantum dots grown by infilling self-assembled nanoholes. *Journal of Applied Physics* **112**, 054303 (2012).
- [10] L. Wang *et al.* Self-assembled quantum dots with tunable thickness of the wetting layer: role of vertical confinement on interlevel spacing. *Physical Review B* **80**, 085309 (2009).
- [11] B. J. Witek *et al.* Measurement of the g-factor tensor in a quantum dot and disentanglement of exciton spins. *Phys. Rev. B* **84**, 195305 (2011).
- [12] M. Bouwes Bavinck *et al.* Controlling a nanowire quantum dot band gap using a straining dielectric envelope. *Nano letters* **12**, 6206 (2012).

- [13] R. Trotta *et al.* Universal recovery of the energy-level degeneracy of bright excitons in ingaas quantum dots without a structure symmetry. *Phys. Rev. Lett.* **109**, 147401 (2012).

NON-LOCALITY OF A SINGLE PHOTON

B.J. Witek, R.W. Heeres

In this chapter we use photons to experimentally test non-locality, one of the fundamental properties of quantum mechanics. Non-locality has been already shown for pairs of entangled particles, however here we aim at proving non-locality of a single particle, a concept introduced in chapter 2.4.3. An InGaAs quantum dot is chosen as a source of single photons. The non-locality of single photon is tested in a homodyne detection measurement with a reference local oscillator field (the laser). We show Einstein-Podolsky-Rosen (EPR) type of correlations for a single photon field in two spatial modes. After correction for the detectors response time we obtain $74 \pm 4\%$ visibility. This value is limited by the multiphoton emission events from the quantum dot and discarding them improves the visibility to $98 \pm 4\%$.

7.1 Experimental details

Successful verification of single photon non-locality relies on high visibility of single photon and local oscillator interference. First of all, in order to ensure high spatial overlap of two modes we carry on a homodyne detection in a fiber network. Further, our goal is to achieve the highest possible indistinguishability of the two dissimilar photon sources. In the following paragraphs we describe our experimental set-up, characterize the photon sources and show the procedure of tuning the local oscillator energy to match the single photons.

7.1.1 Fiber network

The polarization maintaining fiber network and its components were designed for 915 nm wavelength (roughly the wavelength of the quantum dot emission). A schematic of the fiber network is shown in fig. 7.1. There are two independent inputs, one for single photons and one for the local oscillator field. A tunable Ti:Sapphire (Matisse) laser (labeled as "Laser 1") serves as a local oscillator (continuous wave). A linear polarizer in front of the fiber coupler ensures that only one polarization (vertical) is coupled into the fiber. The local oscillator is split into two arms with a 50:50 beam splitter. In each arm the fiber is wrapped around a piezoactuator, which is used for the local oscillator phase control and for changing the measurement basis in a Bell test. Each fiber arm with phase control is 8 meters long before the signal is split by another beam splitter, this time of 30:70 ratio. Its task is to direct 30% of the local oscillator signal to the homodyne detectors and 70% of the signal is picked for the interferometric local oscillator phase measurement. The phase can be readout by looking at relative currents of two silicon photodetectors D1 and D2 (Thorlabs Si Amplified detectors). In section 7.1.4 we describe how we implement the phase control using the feedback based on the signal of D1 and D2.

"Laser 2" is a tunable Ti:Sapphire (Mira) laser used for the non-resonant, pulsed (≈ 5 picosecond) excitation of a quantum dot. First, its beam is coupled to a home-made fiber network, which doubles the repetition rate from 76 MHz to 152 MHz. The working principle is very simple; we split the laser into two arms with a relative delay corresponding to half of a repetition period (6.3 ns) and merge them again.

The quantum dot is in a home-made helium bath cryostat. Before the quantum dot emission is coupled to a polarization maintaining fiber network, it passes through a linear polarizer (vertical orientation). The first 50:50 beam splitter splits the single photon field to create a nonlocal single photon field entanglement. Next, after 0.8 meters of the fiber, the single photon field is mixed with the local oscillator at the beam splitters. The beam splitters belonging to the two homodyne detectors are marked with exclamation marks in fig. 7.1. There is only one APD in each homodyne detector. Since the spectrum of the quantum dot consists of several lines (see section 7.1.2 we first use a spectrometer to spectrally select only one transition of interest.

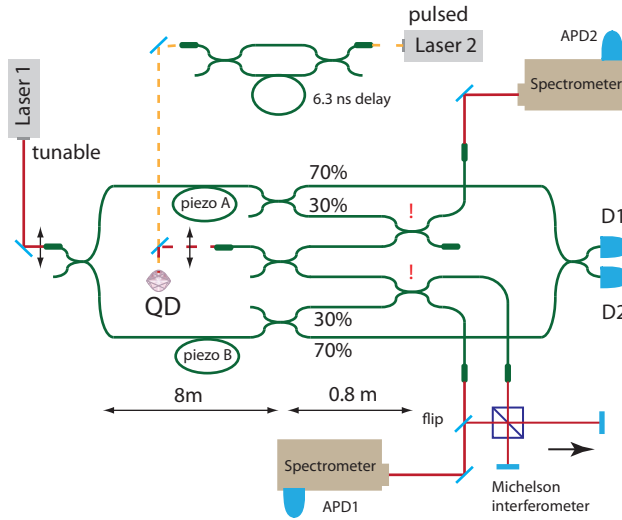


Figure 7.1 | Schematic of the fiber network used for testing quantum mechanical single photon non-locality. The polarization maintaining fiber and the fiber components (like beam splitters) were designed for 915 nm wavelength. The local oscillator ('Laser 1') and single quantum dot photons (excited by "Laser 2") are coupled to different inputs of the fiber network. Each input splits in two arms. Red exclamation marks mark the beamsplitters, where the single photon field mixes with the local oscillator. The result of the homodyne detection is received by the APD1 and APD2 mounted behind the spectrometers. Silicon detectors D1 and D2 are used for read out of the relative phase of a local oscillator, whereas the phase can be set and controlled by piezoA and piezoB. One of the fiber network outputs is directed to the Michelson interferometer, where the energy difference between the local oscillator photons and the quantum dot photons can be detected.

One of the free outputs of the homodyne detector (which is not equipped with the spectrometer and the APD) is sent to a Michelson interferometer. The signal carried in this fiber consists both of the quantum dot single photons and the local oscillator photons. In the following paragraphs (section 7.1.3) we explain how the Michelson interferometer is used to overlap the energy of the local oscillator and the single photons.

7.1.2 Single photon source

We have considered three main criteria when selecting a quantum dot single photon source: (i) brightness (ii) coherence (iii) wavelength (matching the tuning range of the Matisse laser).

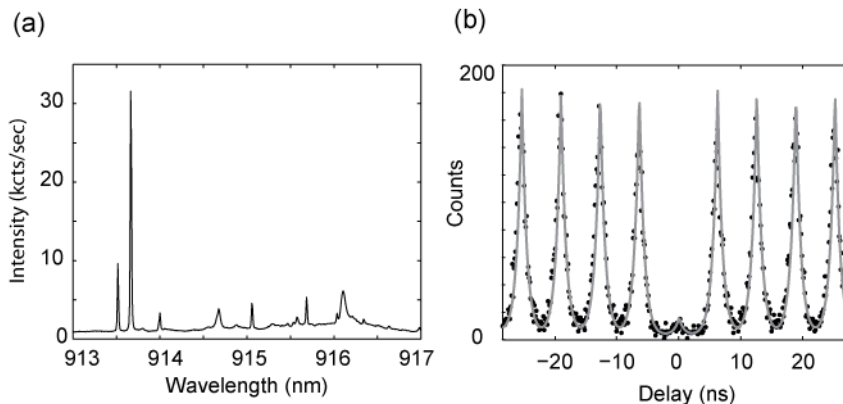


Figure 7.2 | (a) Spectrum of the InGaAs quantum dot, a bright transition around 913.7 nm is used as a single photon source. (b) Second order correlation function measurement verifying the purity of a single photon source. The quantum dot is excited with a doubled rate of Mira (every 6.3 ns). The measurement was performed in the fiber network having the 'Laser 1' blocked. Two APDs on spectrometers recorded start-stop counts for the correlations.

Two quantum dot systems were investigated: self-assembled quantum dots and nanowire quantum dots. In both cases several quantum dots were measured to select an optimal candidate. The nanowire system, consisting of InAsP quantum dots in defect-free wurtzite nanowires is introduced in ref.¹. The other sample consists of self-assembled InGaAs quantum dots in GaAs grown inside an optical cavity defined by two Bragg mirrors. The cavity has a large volume, therefore it does not change the lifetime of optical transitions. However, it is of great use in the experiment as light emitted in resonance with the cavity is directed mostly orthogonally to the sample surface, towards the collection optics. After a series of measurements we decided to select the InGaAs self-assembled quantum dot as the source of single photons. The dot emits photons around 914 nm, which lies still within the Matisse tuning range, in contrast to most of the dots in the nanowire sample (wavelength 930 nm). We have picked the brightest line in the spectra presented in fig. 7.2(a). It is possible to obtain as many as 44 000 counts on an APD after passing through the polarization maintaining single mode fiber network (which divides the signal in four outputs) and the spectrometer. Second order correlation function measurement presented in fig.

7.2(b), verifies the purity of a single photon emission ($g^2(0) = 0.07$). The probability of detecting two or more photons from a quantum dot $P(n \geq 2) = \frac{1}{2}\hat{n}g^{(2)}(0)$ is 14 times smaller than for a Poissonian source, for which $P(n \geq 2) = \frac{1}{2}\hat{n}$.

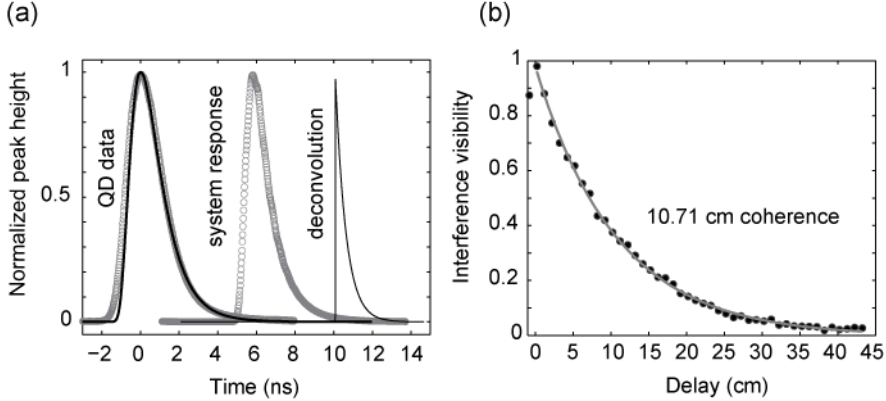


Figure 7.3 | Coherence properties of the single photon source. (a) Lifetime measurement in time-resolved photoluminescence; the APD response measured with the picosecond laser pulse is used to deconvolute the quantum dot signal and get $T_1 = 544ps$. (b) Coherence measurement in the Michelson interferometer ($T_2 = 357ps$).

In fig. 7.3 we show the radiative lifetime T_1 and the phase coherence of the single photons T_2 . We determined the lifetime $T_1 = 544$ ps in time resolve photoluminescence using an avalanche photodiode (fig. 7.3(a)). In order to obtain T_1 we fit an exponential decay convolved with the system response to a picosecond laser pulse. Coherence length of 10.71 cm measured in the Michelson interferometer translates to coherence time of $T_2 = 357$ ps. Although our quantum dot is still far from the Fourier limit ($T_2/2T_1 = 0.32$), it is less affected by the inhomogeneous broadening than a nanowire quantum dot with $T_2 = 340$ ps and $T_1 = 1.63$ ns ($T_2/2T_1 = 0.10$).

7.1.3 Local oscillator and single photon indistinguishability

In principle, photons coming from different origins can interfere with perfect visibility, provided they are made indistinguishable in all degrees of freedom. In our experiment we can ensure that the quantum dot photons and the local oscillator photons have the same polarization and identical energy. However, photons from these two sources differ by orders of magnitude in coherence and bandwidth. Successful interference of quantum dot photons and laser photons has been demonstrated by A. J. Bennett et. al², which encouraged us to proceed with our implementation of the non-locality test.

When coupling light to a polarization maintaining fiber, a polarimeter (Thorlabs Pax series) was used to measure the extinction ratio. Extinction of 30-40 dB could be

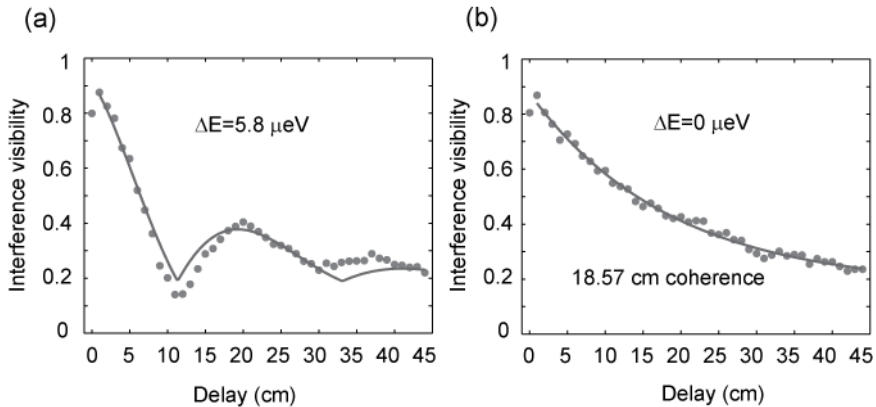


Figure 7.4 | Single photons and laser photons (local oscillator) in the Michelson interferometer. (a) Beating in the interference signal resulting from the energy mismatch $\Delta E = 5.68 \mu\text{eV}$ between the two photon sources. (b) Laser photons tuned to the energy of quantum dot photons; no beating observed, a combined beam of photons exhibits enhanced coherence (18.57 cm) compared to single quantum dot photons (10.71 cm).

maximally achieved.

The next step is to ensure that the two photon sources have the same energy. We use a scheme based on interference in a Michelson interferometer. We attenuate the local oscillator so that it gives a comparable count rate to the quantum dot emission and send both through the Michelson interferometer. If there are two different energy components present, then we observe ‘beating’ in the interference visibility, as presented in fig. 7.4 (a). The period of the beats is inversely proportional to the energy difference between the states. The fit gives us an estimation of the energy difference $\Delta E = 5.68 \mu\text{eV}$. The local oscillator wavelength is measured with a high resolution wavelength meter (HighFinesse, resolution 100 MHz = $0.4 \mu\text{eV}$) so we can monitor how the energy shifts when we tune the laser. After shifting the laser energy by $\Delta E = 5.80 \mu\text{eV}$ we observe a perfect spectral overlap with single photons in fig. 7.4(b). The coherence of the quantum dot photons combined with the laser photons is over 18 cm.

7.1.4 Local oscillator relative phase control

By changing the relative phase between the two arms of the local oscillator we can observe a formation of the interference pattern with detectors $D1$ and $D2$, as shown in fig. 7.5. The change in relative phase is achieved by stretching one of the fiber arms with the piezoactuator. A voltage in a range of 0-0.6V can typically induce a phase change up to 2π . We run such voltage scan as a calibration procedure before taking

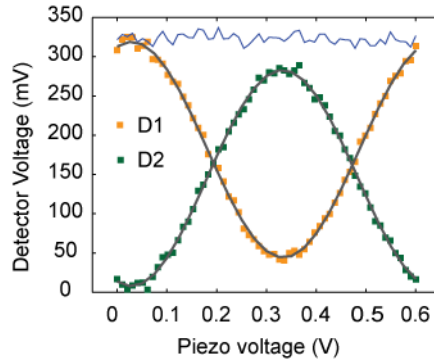


Figure 7.5 | Calibration procedure of the phase stabilization feedback loop. The output voltage of the silicon detectors D1 and D2 is monitored while the piezoA voltage is being ramped up from 0 to 0.6V and piezoB kept at a constant voltage. Interference pattern recorded by D1 and D2 detectors is fitted by a sinusoidal function. The blue line is the sum of the D1 and D2 detector outputs, which is a test of local oscillator intensity stability.

each data point in the final measurement. For every angle θ from 0 to 2π , there is a unique correspondence to a given intensity ratio $D1/D2$ and its slope $\frac{\partial D1/D2}{\partial \theta}$.

Next, we run a procedure to set a desired relative phase θ and keep it constant against any drift in the fiber network. An example is shown in fig. 7.6. A set point $\theta = 75^\circ$ corresponds to highly unbalanced output of the D1 and D2 detectors as shown in fig. 7.6 (a), whereas for $\theta = 0^\circ$ the detectors outputs should be more balanced, as in fig. 7.6 (b). The desired ratio in each case is set very quickly at the beginning and then kept constant throughout the 15 min measurement time. In fig. 7.6 (c) and (d) we see the action of the feedback control loop, that compensates for any drift with the piezo voltage. As a result, the relative phase oscillates around the set point with certain accuracy. Close to the maxima of the sinusoidal function, where the first derivative changes sign, the feedback becomes more problematic. Therefore, the relative phase $\theta = 75$ deg is set with lower accuracy (fig. 7.6 (c)) than $\theta = 10$ deg (fig. 7.6 (d)).

7.2 Data acquisition and analysis

The local oscillator operates in a continuous wave mode, whereas the quantum dot is excited with laser pulses every 6.3 ns. We use Time-Tagged Time-Resolved (TTTR) mode of a HydraHarp picosecond event timer to record individual count events and their arrival time for the APD1 (channel CH1) and the APD2 (channel CH2). Time-tagging is synchronized with a dedicated SYNC channel input, being the same pulsed laser as we use for the dot excitation. The knowledge of arrival time of the photons

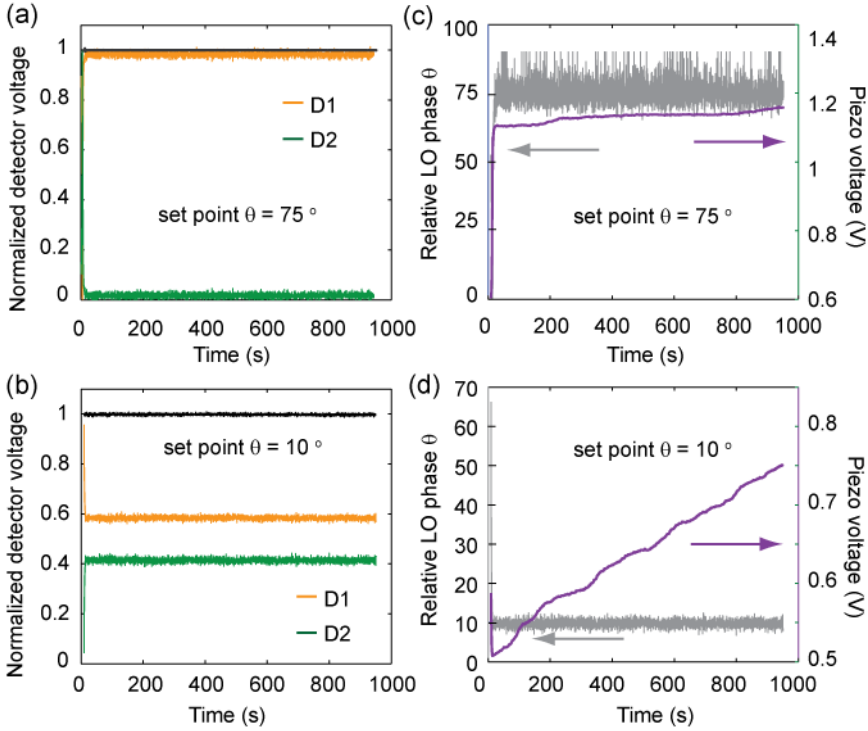


Figure 7.6 | Example demonstration of the phase stabilization procedure for (a,c) $\theta = 75^\circ$ and (b,d) $\theta = 10^\circ$. executed for more than 15 min. (a) and (b) show directly the output voltage of detectors D1 and D2 which is used as a feedback in the stabilization loop. In (c) and (d) the piezo voltage compensates for the local oscillator phase drift so that the phase is kept constant. The procedure is more accurate for θ close to 0° (d), than for interference maxima close to $\theta = \pm 90^\circ$ (c).

enables us to correlate the detection events between the two channels. Each data point is integrated for 15 min and we ensure that the local oscillator relative phase θ and its amplitude α do not change. We record arrival events with 32 ps resolution.

7.2.1 Single channel histograms

Time tagging allows us to construct histograms of events in each of the channels, where a 'START' signal is given by the SYNC laser and a "STOP" signal by a detection event. Fig.7.7 shows a typical single channel histogram calculated from a dataset obtained in the TTTR mode. The outputs of CH1 and CH2 with respect to the SYNC signal in the absence of the local oscillator (fig. 7.7 (a) and (b)) are equivalent

to the lifetime measurement in a histogram mode (fig. 7.3 (a)). The presence of the local oscillator in fig. 7.7 adds a constant contribution of the CW laser to the histogram, however, the quantum dot photons arriving every 6.3 ns can still be clearly distinguished. The local oscillator flat contribution is extracted from the fit (black lines).

We use the single channel histograms to determine the local oscillator intensity with respect to single photons intensity. Fig. 7.8 explains the procedure we implement

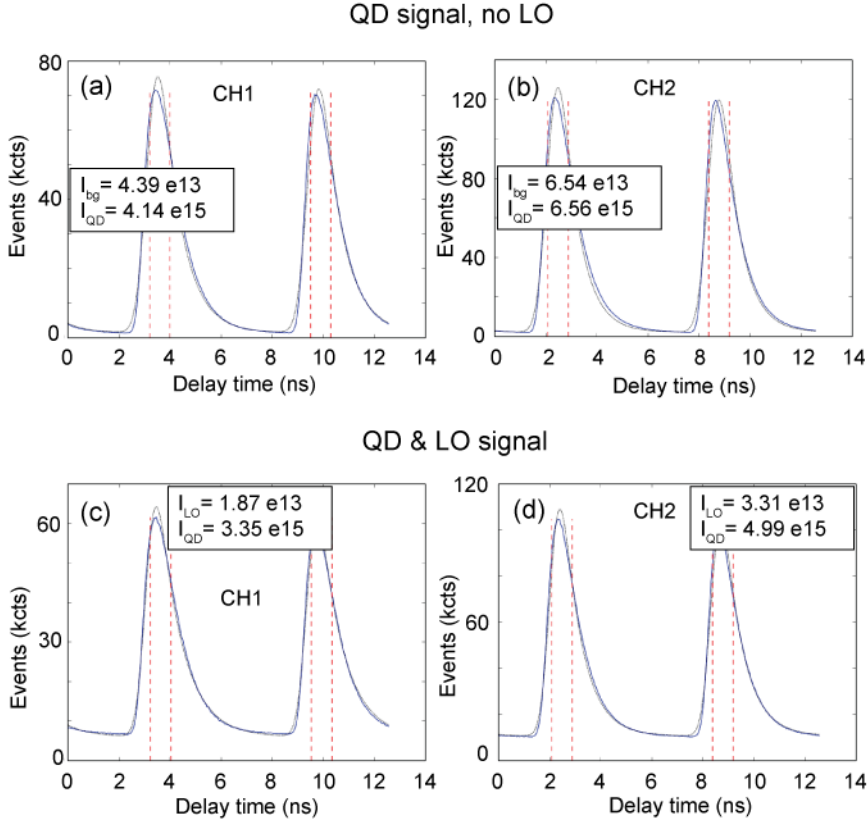


Figure 7.7 | Single channel histograms built from a data file acquired in a Time-Tagged Time-Resolved mode. (a, b) Only a quantum dot (QD) signal measured and (c, d) combined signal with a local oscillator (LO). From the fit (dotted lines) we extract a constant contribution of the local oscillator and calculate the local oscillator intensity (I_{LO}) and the quantum dot intensity (I_{QD}). In the absence of the local oscillator (I_{bg}) stands for a constant background.

to extract the local oscillator amplitude α from a single channel histogram. In our

experiment, single photons originate from an exciton transition of radiative lifetime T_1 , hence the arrival time of a single photon at the detector is characterized by a single exponential decay (black curve) with time constant T_1 . However, due to the finite time resolution of our detectors, the detection time is smeared out by the APD jitter. In fig. 7.8 (a) a typical histogram trace obtained with our APDs is shown. It consists of the local oscillator flat contribution (grey shaded area) and the quantum dot single photon events (purple curve). The APD jitter only gives uncertainty to the photon detection time, however, the overall count rate is still a good measure of the single photon source intensity. Therefore we take the area below the APD single photon curve (purple line) and define it as the quantum dot intensity I_{QD} . For the

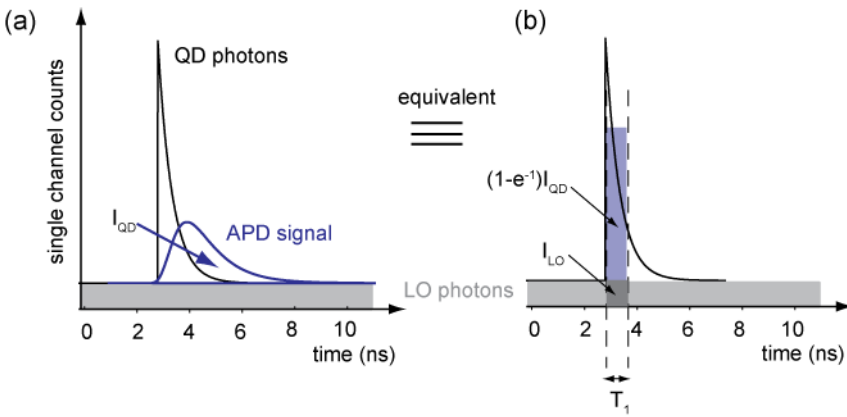


Figure 7.8 | Single channel histogram of detection events recorder with (a) finite time resolution and (b) infinite time resolution.

quantum interference experiment the field amplitude ratio between the local oscillator and the quantum dot is important. We extract the local oscillator intensity I_{LO} in a straight-forward way. We are interested in the local oscillator intensity I_{LO} that is seen by a single photon, hence we look in a time window T_1 . The effective quantum dot intensity is more complicated as the quantum dot emission intensity changes in time. We know that there is 63% probability $(1 - e^{-1})$ that a single photon is emitted within T_1 time. Hence we define the effective quantum dot intensity in time T_1 to be

$I_{QD}(1 - e^{-1})$ as shown in fig. 7.8 (b). Intensities I_{QD} and I_{LO} in a single channel histogram relate to the fields amplitude in the following way:

$$I_{QD} = \frac{1}{4}, \quad (7.1)$$

$$I_{LO} = \frac{1}{2}\alpha^2. \quad (7.2)$$

This relation is clear from a schematic in fig. 3.1 in chapter ???. It follows that the local oscillator amplitude α is:

$$\alpha = \sqrt{\frac{I_{LO}}{2(1 - e^{-1})I_{QD}}} \quad (7.3)$$

7.2.2 Two channel coincidence histogram

To obtain a two channel coincidence histogram we correlate the detection events from CH0 and CH1. First, we look at the case when only quantum dot photons are present in the fiber network. Figure 7.9(a) presents the antibunching measurement histogram constructed from a dataset acquired in a TTTR mode. The number of coincidence events in the zero-delay peak is clearly suppressed in comparison to the non-zero delay peaks, therefore, as expected, the quantum dot photons are antibunched. However, the antibunching peak has a peculiar volcano shape. In order to understand it better we subtract the contribution from the other peaks. The red curve represents the fit of a function:

$$y = y_0 + \sum_n (Ae^{-\frac{|t-nT|}{t_1}} * e^{-\frac{(t-nT)^2}{2w^2}}) \quad (7.4)$$

where n is the number of peaks (> 15), A reflects their amplitude, t_1 represents the exponential decay constant of the quantum dot photons and w is the system response function width, $T = 6.3$ ns is the quantum dot excitation period. Important timescales obtained from the fit are $w = 401$ ps and $t_1 = 974$ ps (t_1 is indeed in the order of the quantum dot photons lifetime T_1). We assume that observed correlations come only from the quantum dot photons and there are no ‘dark’ correlations, therefore we keep $y_0 = 0$ for this fit. This assumption is justified since the dark count rate is less than 1% (0.8% for CH0 and 0.2% for CH1) of the quantum dot signal. The green curve in figure 7.9(a) represents the data after the subtraction of the contribution from the peaks outside the zero delay (red curve). Therefore it shows only zero delay peak coincidences and we zoom into them in fig. 7.9(b). We can fit the volcano shape with the following function:

$$y = (A_0e^{-\frac{|t|}{t_1}} - A_{dip}e^{-\frac{|t|}{t_{1,dip}}}) * e^{-\frac{t^2}{2w^2}} \quad (7.5)$$

The only fit parameters here are A_0 , A_{dip} and $t_{1,dip}$, the system response w and exponential decay constant t_1 are fixed to be the same as for other (non-zero delay)

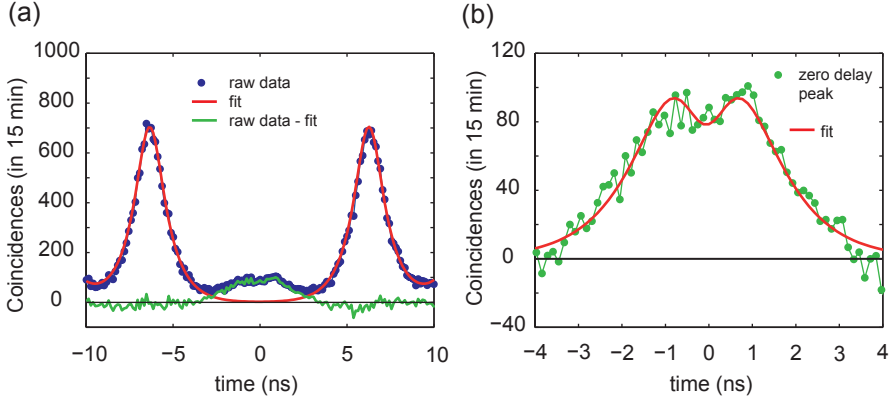


Figure 7.9 | (a) Two channel coincidences showing quantum dot antibunching measurement in a TTTR more. Red line represents a fit to the non-zero delay peaks, green line shows the data after a subtraction of the non-zero delay coincidences contribution. (b) Zoom into the zero delay peak (green data points) and the fit (red line).

peaks. The shape of the zero-delay suggests that there is some re-feeding of the quantum dot on the timescale of $t_{1,dip} = 430$ ps, however, we are not yet able to explain it.

The two channel coincidence histogram for the case when the local oscillator of amplitude $\alpha = 0.18 \pm 0.01$ is present in the experiment is shown in fig. 7.10. We fit to this data the same function as in eq. 7.6, however, we fix w , t_1 and A to be the same as in the antibunching measurement in fig. 7.9(a). The only fit parameter is y_0 , which in this case accounts for the coincidence events from the LO-LO and LO-QD. Once again, we subtract the contribution from the peaks outside the zero delay (red curve) to focus our attention on the zero delay peak (green curve). We see that the appearance of the zero delay peak depends on the phase of the local oscillator! For the phase of $\theta = 0^\circ$ we observe a clear dip (fig. 7.10(a)) whereas for the phase of $\theta = 220^\circ$ a peak appears. This is a signature of phase dependent quantum interference between the dot photons and the local oscillator photons. In fig. 7.10 (c) and (d) we zoom only on the interference peak/dip (green curve) which is plot on top of the shape of the antibunching peak (black curve) from fig. 7.9(b). The effect of the quantum dot and local oscillator photons interference is manifested by the green curve only in the part that deviates from the standard antibunching data (black curve). Gray points show the data corrected for imperfect antibunching and the fit of the interference peak/dip:

$$y = A_{inter} e^{-\frac{|t|}{t_{inter}}} * e^{-\frac{t^2}{2w^2}} \quad (7.6)$$

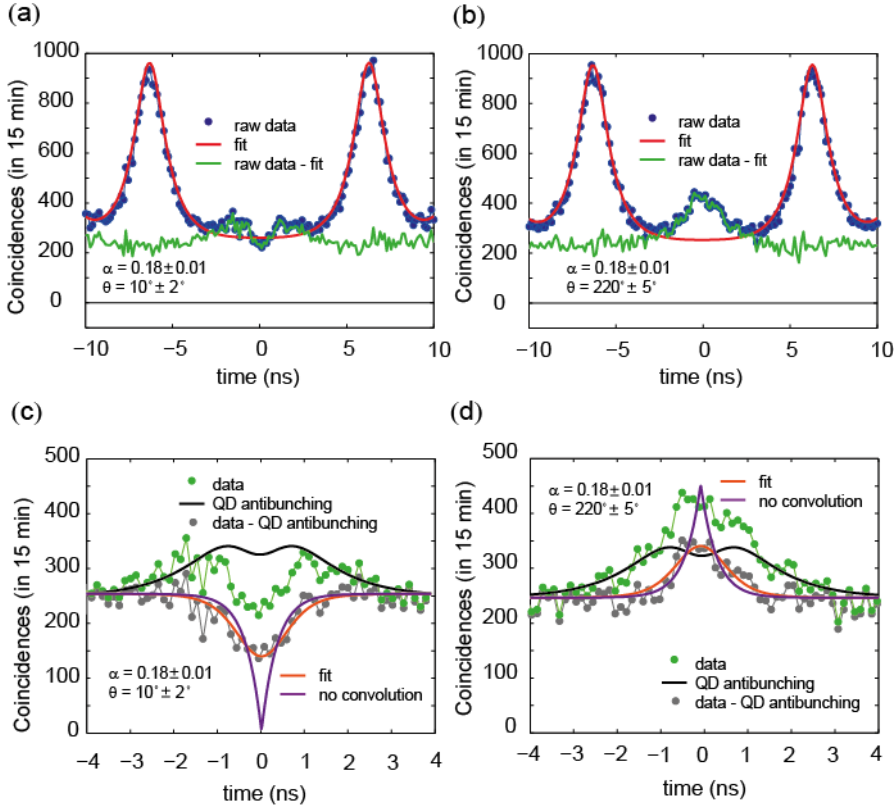


Figure 7.10 | (a) Two channel coincidences for quantum dot and local oscillator photons. The local oscillator amplitude $\alpha = 0.18 \pm 0.01$ is fixed, whereas the relative phase between the arms is $\theta = 10^\circ$ (a,c) and $\theta = 220^\circ$ (b,d). In (a) and (b) raw data is shown (blue datapoints), (c) and (d) show only coincidences in the zero delay peak (green datapoints). Black line represents the shape of the imperfect quantum dot antibunching peak, which is subtracted to obtain gray datapoints. Orange line is the fit of the interference effect that accounts for the finite system response time, whereas the purple line is a deconvolution.

Interestingly, we find that $t_{inter} = 360\text{ps}$ fits best all the interference peaks and dips for 9 datasets with different local oscillator phases. This value is the same (within the errorbar) as the quantum dot coherence time $T_2 = 357\text{ps}$ and as argued in ref. ³, a pair of photons is coincident to within photons coherence length. Once again, in the fit we have accounted for the finite system response time of the width $w = 401\text{ps}$. Knowing the response time allows us to reconstruct the interference effect as it would look with perfect time resolution of our APDs and we show it with a purple line. For the phase of $\theta = 10^\circ$ the interference dip goes almost to zero, which is a sign of high

interference visibility.

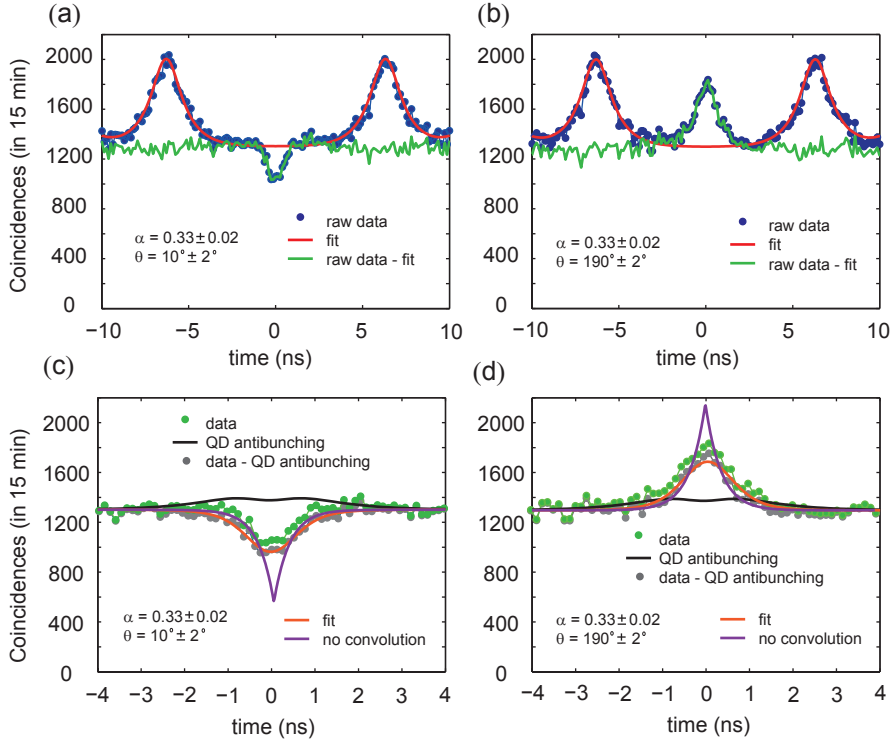


Figure 7.11 | (a) Two channel coincidences for quantum dot and local oscillator photons. The local oscillator amplitude $\alpha = 0.33 \pm 0.02$ is fixed, whereas the relative phase between the arms is $\theta = 10^\circ$ (a,c) and $\theta = 190^\circ$ (b,d). In (a) and (b) raw data is shown (blue datapoints), (c) and (d) show only coincidences in the zero delay peak (green datapoints). Black line represents the shape of the imperfect quantum dot antibunching peak, which is subtracted to obtain gray datapoints. Orange line is the fit of the interference effect that accounts for the finite system response time, whereas the purple line is a deconvolution.

We have performed the same measurement also for the local oscillator amplitude $\alpha = 0.33 \pm 0.02$. The effect of the quantum dot and local oscillator photons interference is more pronounced thanks to a higher relative local oscillator intensity as shown in fig. 7.11 (a) and (b). However, the overall interference visibility is much lower because of the constant contribution of the LO-LO correlation events. As apparent from fig. 7.11(c) the interference dip does not reach zero even if we correct for the time response of the system.

We summarize our results for different phases and two local oscillator amplitudes ($\alpha = 0.18$ and 0.33) in figure 7.12(a) and (b). The EPR-type correlation for the interference is revealed as a function of the local oscillator phase θ .

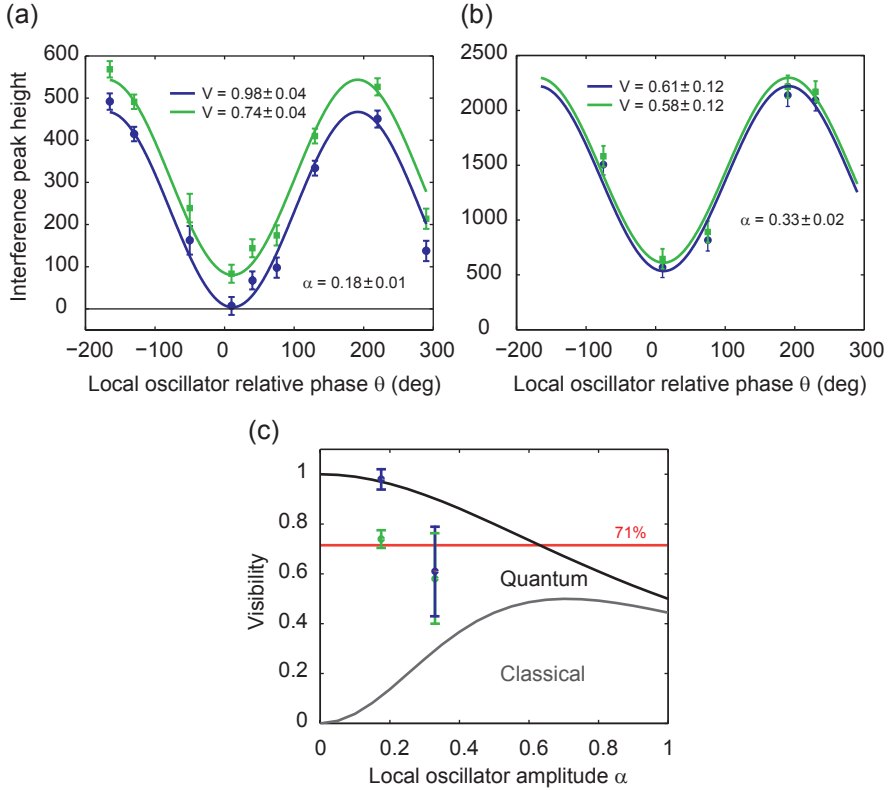


Figure 7.12 | EPR-type correlation for (a) $\alpha = 0.18 \pm 0.01$ and (b) $\alpha = 0.33 \pm 0.02$ as a function of relative local oscillator phase θ . Blue points represent the case when the dataset is corrected for imperfect antibunching, whereas green points do not correct for it. All values are corrected for the finite system response time. (c) Visibility as a function of local oscillator amplitude α . All measurement results lie outside the classical regime. It is possible to violate Bell's inequalities with $\alpha = 0.18 \pm 0.01$.

The data for $\alpha = 0.18 \pm 0.01$ in fig. 7.12(a) corrected both for the system response and the imperfect antibunching show very high interference visibility of $V = 98 \pm 4\%$ (blue curve). If we do not correct for antibunching (green curve), the visibility drops to $V = 74 \pm 4\%$, which is still above the threshold of 71% allowing for Bell's inequalities violation. The interference visibility for higher α (0.33 ± 0.4) in fig. 7.12(a) is around

60%. We note that a large uncertainty on the visibility value is a result of very poor statistics in this measurement (only 5 different phases θ). However, the fit is still trustworthy, since the minimum and the maximum of the interference occur at the same phases θ as in fig. 7.12(a). In fig. 7.12(c) all interference results are summarized and compared to the quantum and classical regimes. It is worth to note that not only the absolute numbers of the visibility bring us to the quantum regime, but also the trend. Visibility in our experiment increases with decreasing local oscillator amplitude α , and it should not be the case if the effect was classical.

7.3 Conclusion

In conclusion, we have demonstrated that it is possible to violate Bell's inequalities with a single photon from a quantum dot (for the local oscillator phase of $\alpha = 0.18 \pm 0.01$). There are two aspects that can be further improved in our experiment. First of all, detectors with better time resolution (below the quantum dot photons coherence time T_2) would result in more pronounced interference data without correcting for the finite time-response. A much more severe issue of the imperfect quantum dot antibunching should be understood and solved. This effect requires further investigations to draw some hypothesis. The volcano shape of the antibunching peak was observed for every antibunching measurement in the TTTR mode.

It will be also very useful to measure quantum dot photons lifetime T_1 with better resolution detectors, since T_1 is an important parameter in our fits and is also used in the definition of α .

Acknowledgments I thank Klaus Jöns for his help and involvement in fixing the laser.

7.4 Bibliography

- [1] D. Dalacu *et al.* Ultraclean emission from inasp quantum dots in defect-free wurtzite inp nanowires. *Nano letters* **12**, 5919 (2012).
- [2] A. Bennett, R. Patel, C. Nicoll, D. Ritchie and A. Shields. Interference of dissimilar photon sources. *Nature Physics* **5**, 715 (2009).
- [3] J. Rarity. Interference of single photons from separate sources. *Annals of the New York Academy of Sciences* **755**, 624 (1995).

OUTLOOK

8.1 Spins: heavy or light?

After the efforts of growers, theoreticians and experimentalists were combined in order to realize the highest purity (>95%) light hole ground state in semiconductor quantum dots, a natural question arises: in which applications is the light hole advantageous? In a broader picture, which one of the three spin species in quantum dots - electrons, heavy holes and light holes - is the most attractive? The answer is not straightforward and a couple of criteria should be considered which I discuss below.

All-optical manipulation. For all-optical manipulation schemes the heavy hole is the only good choice thanks to its clear optical selection rules. For an optical transition involving a heavy hole, there is one to one correspondence between its spin state and the photon polarization, hence the spin state initialization and the spin state readout can be done optically. On the contrary, a given light hole spin can result in two different photon polarizations, depending on which electron spin it couples to. Both the electron and the heavy hole spin can be subject to optical manipulation. In the first case a negatively charged exciton optical transition is used^{1,2} whereas in the latter case a positively charge exciton transition is addressed³.

All-electrical manipulation. If we consider on-chip spin manipulation, the electron spin can be addressed either directly with oscillating magnetic field⁴ or indirectly with oscillating electric field via the spin-orbit interaction⁵. Heavy holes in semiconductor quantum dots present a serious limitation in the first approach, since they do not couple to the ac magnetic field $B_x e^{i\omega t}$ (term $B_x e^{i\omega t} J_x$ is zero for heavy holes)⁶. Using light holes is the solution to this problem, which became feasible only now when we have learnt to engineer a light hole ground state⁷.

Thanks to a strong spin orbit interaction there are ongoing efforts to use holes as a spin-orbit qubit⁸. Nonetheless, to the best of my knowledge, this approach is limited only to gate-controlled quantum dots.

Best candidate for a robust, coherent qubit. A great advantage of p-type heavy holes is that they interact 10 times weaker with the nuclear bath than s-type electrons^{9,10} and therefore should preserve their coherence for longer. However, spin echo technique reveals no drastic difference between the electron¹¹ and the heavy hole³ T_2 time (in both cases 1-3 μ s). It has been demonstrated that on the one hand the hole spin is less sensitive to dephasing due to nuclei, but on the other hand it is more sensitive to dephasing due to electric field³. However, heavy holes' high sensitivity to spectral diffusion is mostly a problem in charge tunable and highly doped structures. The growth of high purity, defect free nanowires and cooling down to 300 mK should substantially reduce this obstacle¹².

In a previous section I argued that a light hole spin enables electrical on-chip manipulation with the oscillating magnetic field, whereas the heavy hole does not. This is an example of a usual trade-off that we have to accept for qubits: an interaction that allows us to control the the spin state makes it at the same time susceptible to decoherence due to the environment. Heavy holes cannot be manipulated with the ac magnetic field $B_x e^{i\omega t}$, however, the advantage is that they are decoupled from the x and y component of the Overhauser field. The admixture of a light hole state to the heavy hole reduces its coherence time.

Due to spin-orbit interaction holes show 5-10 times shorter spin storage time¹³ than electrons¹⁴ ($T_1 = 20$ ms). However, the strength of the spin-orbit interaction for holes can be engineered by the quantum dot confinement shape. It is predicted that for strongly 2D quantum dots the spin-orbit is reduced and we might achieve even longer T_1 time than for the electrons¹⁵. Additionally, in such flat quantum dots the heavy-light hole mixing is reduced, which leads to longer T_2 coherence time.

Spin-photon interfaces. Optical selections rules for light holes are an obvious obstacle if we want to initialize/readout the spin state, but at the same time they come as a great resource if we want to coherently map a photon polarization superposition onto the spin superposition¹⁶ (the details of this concept can be found in section 2.2.2). Despite the favorable polarization selection rules, as already argued, the feasibility of this implementation is seriously reduced by the enormous exchange interaction of the light hole exciton reported in this thesis.

One to one coherent photon to spin mapping (and vice versa) is a very appealing tool for quantum networks. Recently, however, spin photon entanglement which can serve a similar purpose has been demonstrated with quantum dots^{17,18}. Once the spin and the photon are entangled, we can use this state for teleportation of another photon onto the spin state¹⁹ and effectively realize the photon to spin transfer. These experiments rely on selection rules for heavy holes which are usually given as a natural

ground state in quantum dots. Another alternative for one to one coherent photon to spin transfers based on a heavy hole exciton is to use a photon in a time-bin superposition instead of a polarization superposition, as shown by Kosaka et al.²⁰. The same idea can be realized when the electron and heavy hole spins are disentangled by the careful choice of the magnetic field orientation and magnitude, as proposed in this thesis (chapter 4).

8.2 Current status and future directions

I see even greater potential for quantum dots in their photons than in their spins. In my opinion, quantum dots develop into the best on-demand, bright and coherent single photon sources for quantum optics. Here I mention some of the quantum dots' advantages which support my claim:

- **fast = bright.** The radiative lifetime of a quantum dot usually does not exceed 1 ns, whereas for NV centers in diamond the lifetime is typically 12 ns^{21,22} and similarly for atoms it is tens of ns.²³ Short lifetime enables the generation of single photons at high repetition rate.
- **coherent photons.** In recent years quantum dot photons are approaching the Fourier limit of their coherence thanks to resonant excitation techniques^{24,25} and the use of microcavities that accelerate the spontaneous emission rate²⁶. Photon coherence is a basic requirement if we want to look into quantum effects (e.g. see chapter 7).
- **wide range and tunability of emission energy.** III-V semiconductor quantum dot material system can be chosen to emit photons in energies ranging from infrared in optical communication band (InAs/GaAs quantum dots) to ultraviolet (GaN/AlGaN quantum dots used in white LEDs). Additionally, we are provided with a set of tuning knobs (strain, the magnetic and electric field) for each individual quantum dot if we want to bring it in resonance with another system e.g. a natural atom^{27,28}.
- **electrical and optical excitation.** Next to optical excitation, carriers can be injected into the quantum dot with electric field²⁹. Such electrically driven single photon emission makes realization of practical and compact single photon sources possible. Moreover, an entangled light emitting diode has been demonstrated³⁰.
- **polarization entangled photons from every dot!** It became possible to reduce to zero the fine structure splitting in almost any dot by simultaneous application of large strain and electric fields³¹. In this way high fidelity polarization entanglement generation from quantum dots is turning into a routine³².

Next, we consider the areas that should boost further the development and suitability of quantum dots for quantum optics:

- **Growth.** Since the coherence of electron and hole spins in quantum dots directly affects the coherence of emitted photons, it is recommended to grow quantum dots with high purity heavy hole ground state. Therefore the efforts should be focused on growing flat dots with compressive strain. Quantum dots grown in droplet epitaxy proved to show high shape symmetry³³ which is crucial for spin state purity. It will be interesting to develop a recipe for embedding these quantum dots in compressive strained nanomembranes. Nowadays tensile strain nanomembranes are achieved by adding a thin layer of InAlGaAs, where indium has a higher lattice constant than other materials in the membrane and therefore 'stretches' the structure. In order to achieve compressive strain we should try a material with smaller lattice constant, like AlGaAsP. Additionally, the growth of quantum dots in nanomembranes allows for integration with piezoactuators for dynamic strain tuning.
- **Strain engineering.** Strain is a superb knob for tuning the properties of quantum dots for optics. Biaxial and hydrostatic strain does not affect the symmetry of the dot, therefore does not mix the spin states. On the other hand, axial strain can be used to restore the symmetry of the quantum dot³¹. In contrast to electric field, strain does not quench the optical oscillator strength. Strain can be used to both red shift and blue shift the emission by as much as 200 meV³⁴. In the future efforts should be focused on efficient integration of quantum dots in nanomembranes on piezoactuators.

8.3 Quantum optics: any entanglement is just mode entanglement!

The single photon mode entanglement presented in this thesis seems to be the least complicated and least troublesome entangled state to generate (all that we need is a single photon source and a 50:50 beam splitter). We can map this simple form of the entangled state on a more complex physical system, like e.g., two ensembles of rare-earth ions doped into separate crystals³⁵ and achieve entanglement between two remote quantum memories. Single photon mode entangled state is considered as a resource for quantum computation in linear optics³⁶. A similar approach was proposed for generation of entangled electron-hole (hole = missing electron) pairs in a degenerate electron gas³⁷. In physics of cold atoms and Bose-Einstein condensation it is proposed to use mode entanglement of a single massive particle for dense coding and quantum teleportation³⁸. These are the examples of practical implementations of single particle mode entanglement, however, in my opinion, there are even greater fundamental implications following single particle non-locality.

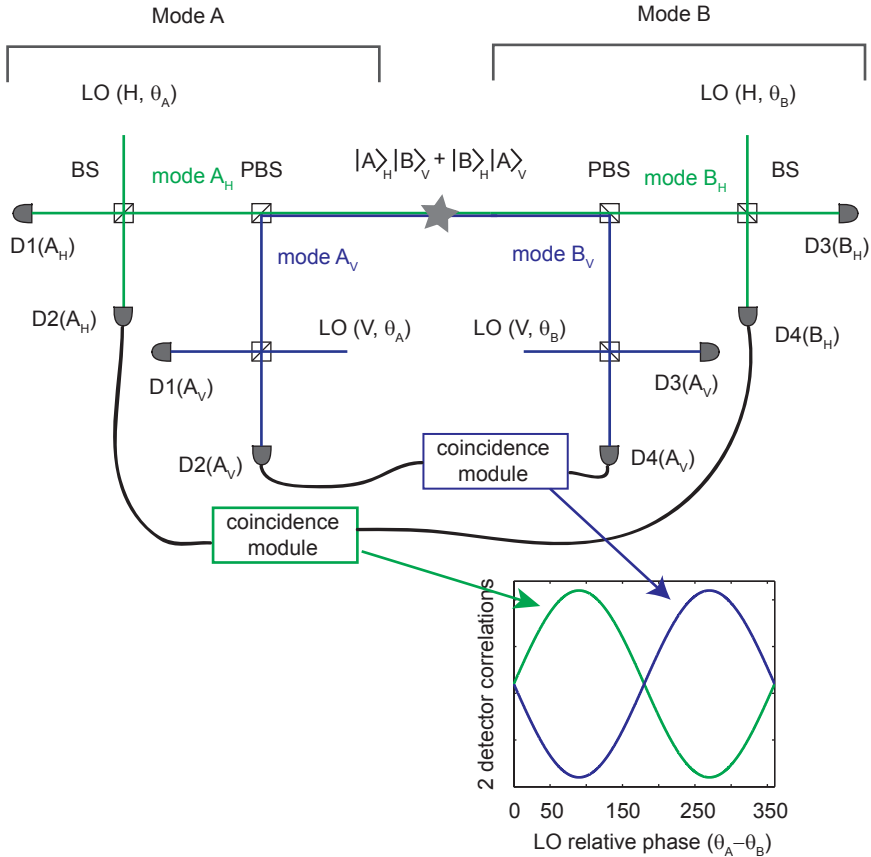


Figure 8.1 | Schematic of the proposed experiment to verify mode entanglement for a polarization entangled photon pair.

The experiment with single photon mode entanglement has tremendously affected the way I look at the two photon entanglement. Let's take a polarization entangled photon pair, where H and V denotes the polarization state and A and B labels the spatial mode. I claim the equivalence of the polarization entangled state of two photons and mode entanglement of two photons:

$$\frac{1}{\sqrt{2}}(|H\rangle_A |V\rangle_B + |V\rangle_A |H\rangle_B) = \frac{1}{\sqrt{2}}(|A\rangle_H |B\rangle_V + |B\rangle_H |A\rangle_V). \quad (8.1)$$

This equation is much more than a simple change of labels, it has profound consequences on how I understand non-locality in quantum mechanics. The left hand side of eq. 8.1

tells us that we have one photon in mode A and one photon in mode B . Even though the polarization state of the individual photon is undefined, the two photons show strong correlations in their polarization. The right hand side of eq. 8.1 gives a little twist to this well accepted picture. Here we have one photon that is V – polarized and one photon H – polarized and both of them are delocalized in mode A and B . Even though the spatial mode of the individual photon is undefined, the pair shows correlations: if the H photon is found in A mode, then the V photon is in mode B and vice versa.

In order to show that correlations have a quantum nature, we should measure them in different bases. The rotation of the polarization basis is straightforward to implement, but the rotation of basis spanned by 0 and 1 Fock state is not trivial to define. Therefore it is more intuitive to look at the state in eq. 8.1 as polarization entanglement. Nonetheless, in this thesis we have successfully implemented a measurement of mode entanglement equivalent to Fock state basis rotation. I propose an analog test for a state in eq. 8.1 to prove the equivalence of polarization entanglement and mode entanglement. The schematic of the setup is presented in fig. 8.1. The source of polarization entangled photons emits into two spatial modes A and B . In each mode a polarizing beam splitter (PBS) is used to spatially separate H and V polarized photons into submodes A_H, A_V, B_H, B_V . In each submode, the field of a single photon is mixed with a weak local oscillator (amplitude $\alpha \ll 1$). The details of this measurement are described in chapter 7 of this thesis. We can probe mode correlations for the H polarized photon by measuring correlations of the $D2(A_H)$ and $D4(A_H)$ detection events as a function of the local oscillator relative phase $\theta = \theta_A - \theta_B$. Similar correlations can be measured for the V polarized photon, as shown in fig. 8.1. The point is to compare the correlations for the H photon and V photon. This proposal is still in a premature stage and I recognize the need for a rigorous mathematical formulation of the expected correlation curves. However, I believe that it is the right approach to verify the equivalence of mode entanglement and entanglement in any other arbitrary degree of freedom (polarization, time bin, energy, etc). If my claim proves to be correct, then suddenly entanglement will not seem a spooky action at a distance. Entanglement should be rather seen as between modes, not just particles.

8.4 Bibliography

- [1] J. Berezovsky, M. Mikkelsen, N. Stoltz, L. Coldren and D. Awschalom. Picosecond coherent optical manipulation of a single electron spin in a quantum dot. *Science* **320**, 349 (2008).
- [2] D. Press, T. D. Ladd, B. Zhang and Y. Yamamoto. Complete quantum control of a single quantum dot spin using ultrafast optical pulses. *Nature* **456**, 218 (2008).
- [3] K. De Greve *et al.* Ultrafast coherent control and suppressed nuclear feedback of a single quantum dot hole qubit. *Nature Physics* **7**, 872 (2011).
- [4] F. Koppens *et al.* Driven coherent oscillations of a single electron spin in a quantum dot. *Nature* **442**, 766 (2006).
- [5] K. Nowack, F. Koppens, Y. V. Nazarov and L. Vandersypen. Coherent control of a single electron spin with electric fields. *Science* **318**, 1430 (2007).
- [6] D. Sleiter and W. F. Brinkman. Using holes in gaas as qubits: An estimate of the rabi frequency in the presence of an external rf field. *Phys. Rev. B* **74**, 153312 (2006).
- [7] Y. Huo *et al.* A light-hole exciton in a quantum dot. *Nature Physics* (2013).
- [8] V. Pribiag *et al.* Electrical control of single hole spins in nanowire quantum dots. *Nature nanotechnology* **8**, 170 (2013).
- [9] P. Fallahi, S. T. Yilmaz and A. Imamoglu. Measurement of a heavy-hole hyperfine interaction in ingaas quantum dots using resonance fluorescence. *Phys. Rev. Lett.* **105**, 257402 (2010).
- [10] E. A. Chekhovich, A. B. Krysa, M. S. Skolnick and A. I. Tartakovskii. Direct measurement of the hole-nuclear spin interaction in single InP/GaInP quantum dots using photoluminescence spectroscopy. *Phys. Rev. Lett.* **106**, 027402 (2011).
- [11] D. Press *et al.* Ultrafast optical spin echo in a single quantum dot. *Nature Photonics* **4**, 367 (2010).
- [12] M. Reimer *et al.* Overcoming power broadening of the quantum dot emission in a pure wurtzite nanowire. *in preparation* .
- [13] D. Heiss *et al.* Observation of extremely slow hole spin relaxation in self-assembled quantum dots. *Phys. Rev. B* **76**, 241306 (2007).
- [14] M. Kroutvar *et al.* Optically programmable electron spin memory using semiconductor quantum dots. *Nature* **432**, 81 (2004).

- [15] D. V. Bulaev and D. Loss. Spin relaxation and decoherence of holes in quantum dots. *Phys. Rev. Lett.* **95**, 076805 (2005).
- [16] R. Vrijen and E. Yablonovitch. A spin-coherent semiconductor photo-detector for quantum communication. *Physica E: Low-dimensional Systems and Nanostructures* **10**, 569 (2001).
- [17] K. De Greve *et al.* Quantum-dot spin-photon entanglement via frequency down-conversion to telecom wavelength. *Nature* **491**, 421 (2012).
- [18] W. Gao, P. Fallahi, E. Togan, J. Miguel-Sanchez and A. Imamoglu. Observation of entanglement between a quantum dot spin and a single photon. *Nature* **491**, 426 (2012).
- [19] W. Gao *et al.* Quantum teleportation from a propagating photon to a solid-state spin qubit. *Nature communications* **4** (2013).
- [20] H. Kosaka *et al.* Coherent transfer of time-bin photons to electron spins in a semiconductor. *Phys. Rev. A* **85**, 042304 (2012).
- [21] A. Collins, M. Thomaz and M. I. B. Jorge. Luminescence decay time of the 1.945 eV centre in type Ib diamond. *Journal of Physics C: Solid State Physics* **16**, 2177 (1983).
- [22] A. Batalov *et al.* Temporal coherence of photons emitted by single nitrogen-vacancy defect centers in diamond using optical Rabi-oscillations. *Phys. Rev. Lett.* **100**, 077401 (2008).
- [23] U. Volz and H. Schmoranzer. Precision lifetime measurements on alkali atoms and on helium by beam-gas-laser spectroscopy. *Physica Scripta* **1996**, 48 (1996).
- [24] S. Ates *et al.* Post-selected indistinguishable photons from the resonance fluorescence of a single quantum dot in a microcavity. *Phys. Rev. Lett.* **103**, 167402 (2009).
- [25] Y.-M. He *et al.* On-demand semiconductor single-photon source with near-unity indistinguishability. *Nature nanotechnology* (2013).
- [26] O. Gazzano *et al.* Bright solid-state sources of indistinguishable single photons. *Nature communications* **4**, 1425 (2013).
- [27] N. Akopian *et al.* Tuning single GaAs quantum dots in resonance with a rubidium vapor. *Applied Physics Letters* **97**, 082103 (2010).
- [28] N. Akopian *et al.* An artificial atom locked to natural atoms. *arXiv preprint arXiv:1302.2005* (2013).
- [29] Z. Yuan *et al.* Electrically driven single-photon source. *Science* **295**, 102 (2002).

- [30] C. Salter *et al.* An entangled-light-emitting diode. *Nature* **465**, 594 (2010).
- [31] R. Trotta *et al.* Universal recovery of the energy-level degeneracy of bright excitons in ingaas quantum dots without a structure symmetry. *Physical review letters* **109**, 147401 (2012).
- [32] R. Trotta, J. S. Wildmann, E. Zallo, O. G. Schmidt and A. Rastelli. Highly entangled photons from hybrid piezoelectric-semiconductor quantum dot devices. *arXiv preprint arXiv:1403.0225* (2014).
- [33] Y. Huo, A. Rastelli and O. Schmidt. Ultra-small excitonic fine structure splitting in highly symmetric quantum dots on gaas (001) substrate. *Applied Physics Letters* **102**, 152105 (2013).
- [34] M. Bouwes Bavinck *et al.* Controlling a nanowire quantum dot band gap using a straining dielectric envelope. *Nano letters* **12**, 6206 (2012).
- [35] I. Usmani *et al.* Heralded quantum entanglement between two crystals. *Nature Photonics* **6**, 234 (2012).
- [36] E. Knill, R. Laflamme and G. J. Milburn. A scheme for efficient quantum computation with linear optics. *nature* **409**, 46 (2001).
- [37] C. Beenakker, C. Emary, M. Kindermann and J. Van Velsen. Proposal for production and detection of entangled electron-hole pairs in a degenerate electron gas. *Physical review letters* **91**, 147901 (2003).
- [38] L. Heaney and V. Vedral. Natural mode entanglement as a resource for quantum communication. *Physical review letters* **103**, 200502 (2009).

APPENDIX A

RELEVANT MATRICES

B.J. Witek, G. Bester

A.1 Spin matrices

Electron spin $S = \frac{1}{2}$ matrices:

$$\sigma_x = \begin{pmatrix} 0 & \frac{1}{2} \\ \frac{1}{2} & 0 \end{pmatrix}$$

$$\sigma_y = \begin{pmatrix} 0 & -\frac{i}{2} \\ \frac{i}{2} & 0 \end{pmatrix}$$

$$\sigma_z = \begin{pmatrix} \frac{1}{2} & 0 \\ 0 & -\frac{1}{2} \end{pmatrix}$$

Hole spin $J = L + S = \frac{3}{2}$ matrices:

$$J_x = \begin{pmatrix} 0 & \frac{\sqrt{3}}{2} & 0 & 0 \\ \frac{\sqrt{3}}{2} & 0 & 1 & 0 \\ 0 & 1 & 0 & \frac{\sqrt{3}}{2} \\ 0 & 0 & \frac{\sqrt{3}}{2} & 0 \end{pmatrix}$$

$$J_y = \begin{pmatrix} 0 & -\frac{i\sqrt{3}}{2} & 0 & 0 \\ \frac{i\sqrt{3}}{2} & 0 & -i & 0 \\ 0 & i & 0 & -\frac{i\sqrt{3}}{2} \\ 0 & 0 & \frac{i\sqrt{3}}{2} & 0 \end{pmatrix}$$

$$J_z = \begin{pmatrix} \frac{3}{2} & 0 & 0 & 0 \\ 0 & \frac{1}{2} & 0 & 0 \\ 0 & 0 & -\frac{1}{2} & 0 \\ 0 & 0 & 0 & -\frac{3}{2} \end{pmatrix}$$

$$J_x^3 = \begin{pmatrix} 0 & \frac{7\sqrt{3}}{8} & 0 & \frac{3}{4} \\ \frac{7\sqrt{3}}{8} & 0 & \frac{5}{2} & 0 \\ 0 & \frac{5}{2} & 0 & \frac{7\sqrt{3}}{8} \\ \frac{3}{4} & 0 & \frac{7\sqrt{3}}{8} & 0 \end{pmatrix}$$

$$J_y^3 = \begin{pmatrix} 0 & -\frac{7i\sqrt{3}}{8} & 0 & \frac{3i}{4} \\ \frac{7i\sqrt{3}}{8} & 0 & -\frac{5i}{2} & 0 \\ 0 & \frac{5i}{2} & 0 & -\frac{7i\sqrt{3}}{8} \\ -\frac{3i}{4} & 0 & \frac{7i\sqrt{3}}{8} & 0 \end{pmatrix}$$

$$J_z^3 = \begin{pmatrix} \frac{27}{8} & 0 & 0 & 0 \\ 0 & \frac{1}{8} & 0 & 0 \\ 0 & 0 & -\frac{1}{8} & 0 \\ 0 & 0 & 0 & -\frac{27}{8} \end{pmatrix}$$

Heavy hole subspace matrices:

$$J_{hh,x} = \begin{pmatrix} 0 & 0 \\ 0 & 0 \end{pmatrix}$$

$$J_{hh,y} = \begin{pmatrix} 0 & 0 \\ 0 & 0 \end{pmatrix}$$

$$J_{hh,z} = \begin{pmatrix} \frac{3}{2} & 0 \\ 0 & -\frac{3}{2} \end{pmatrix}$$

$$J_{hh,x}^3 = \begin{pmatrix} 0 & \frac{3}{4} \\ \frac{3}{4} & 0 \end{pmatrix}$$

$$J_{hh,y}^3 = \begin{pmatrix} 0 & \frac{3i}{4} \\ -\frac{3i}{4} & 0 \end{pmatrix}$$

$$J_{hh,z}^3 = \begin{pmatrix} \frac{27}{8} & 0 \\ 0 & -\frac{27}{8} \end{pmatrix}$$

Light hole subspace matrices:

$$J_{lh,x} = \begin{pmatrix} 0 & 1 \\ 1 & 0 \end{pmatrix}$$

$$J_{lh,y} = \begin{pmatrix} 0 & -i \\ i & 0 \end{pmatrix}$$

$$J_{lh,z} = \begin{pmatrix} \frac{1}{2} & 0 \\ 0 & -\frac{1}{2} \end{pmatrix}$$

$$J_{lh,x}^3 = \begin{pmatrix} 0 & \frac{5}{2} \\ \frac{5}{2} & 0 \end{pmatrix}$$

$$J_{lh,y}^3 = \begin{pmatrix} 0 & -\frac{5i}{2} \\ \frac{5i}{2} & 0 \end{pmatrix}$$

$$J_{lh,z}^3 = \begin{pmatrix} \frac{1}{8} & 0 \\ 0 & -\frac{1}{8} \end{pmatrix}$$

A.2 8 dimensional Exchange Hamiltonian

$$\mathbf{H}_{exch} = \frac{1}{2} \begin{pmatrix} -\delta_0^{HH} & 0 & 0 & 0 & 0 & 0 & 0 & 0 \\ 0 & +\delta_0^{HH} & +\Delta_1 & 0 & 0 & 0 & +\delta_1^{HH} & 0 \\ 0 & +\Delta_1 & 0 & 0 & 0 & 0 & 0 & 0 \\ \Delta_2 & 0 & 0 & 0 & 0 & 0 & 0 & +\delta_1^{HH} \\ 0 & 0 & 0 & 0 & 0 & 0 & 0 & 0 \\ 0 & 0 & 0 & 0 & 0 & 0 & 0 & 0 \\ 0 & +\delta_1^{HH} & +\Delta_1 & 0 & 0 & 0 & +\delta_0^{HH} & 0 \\ 0 & +\delta_1^{HH} & +\Delta_1 & 0 & 0 & 0 & +\delta_0^{HH} & 0 \\ 0 & 0 & +\delta_0^{LH} & +\delta_1^{LH} & 0 & 0 & 0 & \Delta_2 \\ 0 & 0 & +\delta_2^{LH} & 0 & 0 & -\delta_0^{LH} & \Delta_1 & 0 \\ 0 & 0 & 0 & 0 & 0 & 0 & +\delta_0^{HH} & 0 \\ 0 & +\delta_1^{HH} & 0 & 0 & 0 & 0 & +\delta_0^{HH} & 0 \\ +\delta_2^{HH} & 0 & 0 & 0 & 0 & 0 & 0 & -\delta_0^{HH} \end{pmatrix}$$

where:

$$\begin{aligned}
 \delta_0^{HH} &= \frac{1}{2}(3a_z + \frac{27}{4}b_z) & \delta_0^{LH} &= \frac{1}{8}(4a_z + b_z) \\
 \delta_1^{HH} &= -\frac{3}{4}(b_x - b_y) & \delta_1^{LH} &= -(a_x + a_y) - \frac{5}{2}(b_x + b_y) \\
 \delta_2^{HH} &= -\frac{3}{4}(b_x + b_y) & \delta_2^{LH} &= -(a_x - a_y) - \frac{5}{2}(b_x - b_y) \\
 \Delta_1 &= -\frac{\sqrt{3}}{2}(a_x + a_y) - \frac{7\sqrt{3}}{8}(b_x + b_y) \\
 \Delta_2 &= -\frac{\sqrt{3}}{2}(a_x - a_y) - \frac{7\sqrt{3}}{8}(b_x - b_y)
 \end{aligned}$$

Summary

Quantum dots bridge and interface two worlds: the one of quantum particles of matter and quantum particles of light. In a similar fashion, this thesis treats both the topics of single spins and single photons. Our major achievement in the topic of single spins is engineering quantum dots with a high purity light hole state, whereas up to now only a high purity heavy hole state or a mixed hole state was accessible in III-V semiconductor quantum dots. We have developed and optimized the growth technique that offers strain as a tuning knob to switch from heavy to light hole character in GaAs/AlGaAs quantum dots. We have provided an experimental evidence of the light hole exciton based on the analysis of the exciton emission polarization, exchange interaction and the magnetic response. The atomistic pseudopotential method calculations have been performed and they have shown an excellent agreement with our experimental observations. With a demonstration of a light hole exciton we have opened up a new set of optical polarization selection rules for interfacing spins and photons. One of the signatures of a light hole exciton is the presence of two exciton states of z-polarization, however, one of them is dark at zero magnetic field. We have found an extremely large ($\approx 500 \mu\text{eV}$) exchange splitting between these two states. This splitting puts in doubt the feasibility of a single photon to spin coherent transfer scheme based on light holes. Even though our initial motivation for the search of light hole ground state is not valid anymore, we expect to witness new applications of the light hole spin in the following years. A light hole is a novel quantum state in semiconductor quantum dots and it needs further investigation of its potential e.g. for electrical manipulation. It will be also very useful to verify the predictions for the light hole spin interactions with the nuclei and measure its coherence time. The hole spin state quantum number ($3/2$ for heavy or $1/2$ for light) is not the only spin property that can be engineered in quantum dots. The characterization of the electron and hole g-factor tensor shown in this work is the first step towards g-factor engineering by the choice of the quantum dot composition and shape. We have chosen nanowire quantum dots as a promising system for g-factor engineering because of the possibility to controllably grow quantum dots of different sizes and aspect ratios. Our studies have demonstrated that the coupling strength between exciton states can be tuned by a careful choice of the magnetic field angle and magnitude. In particular, we have found the conditions for the electron and heavy hole spin disentanglement. Finally, we summarize the second part of this thesis, where the nonlocality of a single photon was tested using single photons from a quantum dot. Visibility as high as 98% has been measured, whereas the visibility of 71% is enough to violate Bell's inequalities. Therefore it is clear that the concept of quantum nonlocality applies to the state of a single particle just like it does for the entangled particle pair.

Samenvatting

Kwantum dots vormen een brug en interface tussen twee werelden: enerzijds kwantum deeltjes van materie anderzijds kwantum deeltjes van licht. Dit komt terug in deze scriptie, waarin zowel enkele spins als enkele fotonen behandeld worden. Ons belangrijkste resultaat op het gebied van enkele spins is de ontwikkeling van kwantum dots met een grote zuiverheid aan toestanden voor lichte gaten, terwijl tot nu toe alleen een grote zuiverheid aan toestanden voor zware gaten of een gemixte toestand voor gaten mogelijk waren in III-V halfgeleider kwantum dots. We hebben een groeitechniek ontwikkeld en geoptimaliseerd waarbij spanning als afstelling dient om het karakter van de gaten in GaAs/AlGaAs kwantum dots van zwaar naar licht te veranderen. We laten een experimenteel bewijs zien voor een licht gat exciton, gebaseerd op de analyse van de polarisatie van de emissie van dit exciton, de uitwisselingsinteractie en de magnetische respons. De berekeningen aan de hand van de atomistische pseudo-potentiaal methode komen zeer goed overeen met onze experimentele observaties. Met een demonstratie van een licht gat exciton ontstaat er een nieuwe set van optische polarisatie selectieregels voor de interface tussen spins en fotonen. Een van de kenmerken van een licht gat exciton is de aanwezigheid van twee excitons met z-polarisatie, hoewel één van deze twee bij een magneetveld van nul donker is. We hebben een extreem grote (≈ 500 μeV) uitwisselingsenergiesplitsing tussen deze twee toestanden gevonden. Door deze splitsing kan worden betwijfeld of een protocol voor de coherente overdracht van foton naar spin gebaseerd op lichte gaten mogelijk zal zijn. Hoewel de originele reden voor het onderzoek naar lichte gaten hierdoor wegvalt, verwachten we de komende jaren nieuwe toepassingen voor de spin van een licht gat. Een licht gat is een recent uitgevonden kwantum toestand in halfgeleider kwantum dots en er is verder onderzoek nodig om de mogelijkheden te ontdekken, bijvoorbeeld voor elektronische manipulatie. Het zal ook goed zijn om de voorspellingen voor de interactie tussen de spin van lichte gaten en kernspins na te gaan, en de coherentietijd te meten. Het kwantumgetal van de spin van een gat ($3/2$ voor een zwaar gat, $1/2$ voor een licht gat) is niet de enige eigenschap die kan worden bewerkt in kwantum dots. De karakterisatie van de elektron en gat g-factor tensor die wij laten zien is de eerste stap naar g-factor bewerking door keuze van compositie en vorm van de kwantum dot. We hebben kwantum dots in nanodraden gekozen als veelbelovend systeem voor g-factor bewerking, omdat deze kwantum dots gecontroleerd gegroeid kunnen worden met verschillende afmetingen en aspect ratio's. Ons onderzoek laat zien dat de koppeling tussen exciton toestanden kunnen worden afgestemd door de grootte en hoek van het magneetveld zorgvuldig te kiezen. Meerbepaald hebben we de condities gevonden waarbij de verstrengeling tussen spins van een elektron en een licht gat ongedaan gemaakt kan worden. Afsluitend vatten we het tweede deel van deze scriptie samen, waar enkele fotonen uit een kwantum dot gebruikt zijn om de non-lokaliteit van een enkel foton te testen. We hebben een visibiliteit van 98% is gemeten, waar een visibiliteit van 71% genoeg is om Bell's ongelijkheid aan te tonen.

Dit toont aan dat het concept van kwantum non-lokaliteit op een enkel deeltje kan worden toegepast op dezelfde manier als op een paar van verstrengelde deeltjes.

Acknowledgements

Does God play dice? Einstein couldn't accept that the world described by quantum mechanics is ruled by randomness, however, I am very grateful that it is! One lucky random coincidence - meeting Val Zwiller on the bus from the Jaszowiec Conference in 2009 - brought me to Delft despite my deterministic plans to do a PhD in Paris. Val, I want to express my gratitude for the years we worked together. I especially thank you for giving me the freedom and trust that I enjoyed so much in my research and at the same time providing me with the necessary support and resources. Leo, it was very inspiring to have you as my promotor and learn from you how to do research. Hans, Lieven, Ronald, Leo DC and Ad, you bring a great motivating working culture in QT.

I have been extremely fortunate to have Reinier as my mentor in the optics lab. Reinier, I am grateful for your patience and involvement at the early stage of my PhD. Thanks to you my PhD research could get going (in the lab, in the cleanroom, programming). By the end of my PhD, the single photon non-locality experiment carried out with you, turned my research into a thrilling quantum adventure. I wish and hope to stay in contact with professor Reinier Heeres in the future!

My special acknowledgments go to the team in Dresden/Linz and Stuttgart that made the first observation of the light hole exciton in quantum dots possible. Armando Rastelli and Rinaldo Trotta it has been a great experience to work with you. Thank you for your dedicated and thorough way of working. Yongheng Huo, it is impressive how you mastered the growth of such beautiful symmetric dots. Finally, Gabriel Bester, I am very grateful for unveiling the world of Hamiltonians for me. I wish I had even more opportunities for inspiring discussions about physics beyond the light hole subject.

Without the technical help of Jelle, Raymond, Bram and Remco my PhD research in Delft would have been much harder. Thank you for your smart technical solutions and your willingness to help! Yuki, Marja and Angele, you make all the formalities and the paper work run as smooth as possible, this help is priceless for a chaotic physicist like me.

Within my optics team in Delft I owe a distinctive 'thank you' to Nika for his support in the search for light holes and for guiding me onto a high-impact research track. Maaïke, it has been a true pleasure to work with you, it is a pity that only for so short. Gabriele, I am grateful to you for being the team-building spirit in our lab. Working with you was fun and rewarding. Michael, thank you for being the best hokey player! Marijn, I wish you all the best with your Post-Doc in Vienna! Umberto, I appreciate I could learn from you in the beginning of my PhD. Maria, good luck with your PhD, I am impressed how much you have achieved. Iman, all the best with your SSPDs. Finally Klaus, I am very happy that you have joined our team as a Post-Doc and you bring a great value to our group.

Acknowledgements

The friendly Team Diamond, in particular Hannes, Wolfgang and Tim, thank you for the exchange of ideas and the equipment!

QT is filled up with inspiring physics and equally inspiring personalities. Reinier's beer feeding skills, Julia's tea time, Hannes' laughter, Nika's dancing, Floris' super-star look, Stijn's anecdotes, Wolfgang's sweet and sour Germannes, Pasquale's and Gabriele's fine Italian style and the American dream with Vincent and Toeno - this all (and much more!) made me enjoy the years in QT a lot!

I would not be able to carry on in Delft without interacting with its most graceful and beautiful part. Dear ladies, Yun, Marieke, Guen, Ania, Maria F. and Maria B., thank you for many dinners, sports, dancing and other events that I shared with you. Marta, meeting you in Delft made the Netherlands feel less foreign for me. Thank you for all the great moments! Natashka, sharing a house with you really felt like home thanks to your big warm heart and the sparkle of a Slavic soul. Wioletta & co, I hope it is only the beginning of a closer Bruxelles-Rotterdam connection. Julia, from my bachelor student you turned into my powerful support in QT. I feel very happy (and, if I may say, proud) to see all the mind-blowing experiments that you do in the diamond team. Alina, your friendship is always a resource of strength, inspiration and many influential thoughts for me.

I would like to thank those who are the closest to me. Dear parents, I am grateful to you for the wise way in which you taught and explained the world to me. Despite one thousand kilometers between us I always felt your wonderful support and motivation to pursue my dreams. My big brother Maciej, you have been my invaluable guide in many important life decisions. Finally, my thanks go to my husband Paweł, who is a superb ambassador of science outside the academic environment. You always knew how to boost my motivation, either by emphasizing the meaning and uniqueness of my work, by putting on the 'winter' gloves and filling helium with me, or simply by turning my little lab frustrations into a sincere laughter. This thesis would have been much harder to accomplish without you. I am looking into our common future with great confidence and happiness.

Basia

March 2014

List of Publications

1. B. J. Witek, G. Bester, N. Akopian, R. Trotta, Y. H. Huo, A. Rastelli, and V. Zwiller. *Light holes in magnetic field: a complete experimental determination of all spin-spin coupling constants.* in preparation.
2. M.E. Reimer, G. Bulgarini, B.J. Witek, R.W. Heeres, M.A.M. Veerstegh, D. Dalacu, P.J. Poole, V. Zwiller. *Overcoming power broadening of the quantum dot emission in a pure wurtzite nanowire.* submitted.
3. Y. H. Huo, B. J. Witek, S. Kumar, J. R. Cardenas, J. X. Zhang, N. Akopian, R. Singh, E. Zallo, R. Grifone, D. Kriegner, R. Trotta, F. Ding, J. Stangl, V. Zwiller, G. Bester, A. Rastelli, and O. G. Schmidt. *A light-hole exciton in a quantum dot.* Nature Phys. **10**, 46-51 (2014).
4. M. Bouwes Bavinck, M. Zieliński, B. J. Witek, T. Zehender, E. P. A. M. Bakkers, and V. Zwiller. *Controlling a Nanowire Quantum Dot Band Gap Using a Straining Dielectric Envelope.* Nano Lett. **12**, 6206 (2012).
5. B. J. Witek, R. W. Heeres, U. Perinetti, E. P. A. M. Bakkers, L. P. Kouwenhoven, and V. Zwiller. *Measurement of the g-factor tensor in a quantum dot and disentanglement of exciton spins.* Phys. Rev. B **84**, 195305 (2011).

Curriculum Vitae

- March 8, 1985 Born in Szczecin, Poland
- 2000–2004 Secondary school, *V Liceum Ogólnokształcące*, Szczecin, Poland
- 2004–2009 Magister, *Uniwersytet Warszawski* Poland
Thesis research under supervision of Dr. hab. A. Wymolek.
- 2008–2009 Erasmus program, *Joseph Fourier University*, Grenoble, France
Student research in the High Magnetic Field Laboratory.
- 2009–2014 PhD in Applied Physics, *Delft University of Technology*, Netherlands
Thesis research under supervision of Dr. V. Zwiller
and Prof. dr. ir. L. P. Kouwenhoven.

